Electrostriction and Pyroelectricity of PZT/PU Composites

SUBMITTED BY

LAM KAI SIU

A THESIS SUBMITTED IN PARTIAL FULFILMENT OF THE

REQUIREMENTS FOR THE DEGREE OF

MASTER OF PHILOSOPHY IN PHYSICS

AT

THE DEPARTMENT OF APPLIED PHYSICS

THE HONG KONG POLYTECHNIC UNIVERSITY

August, 2003

CERTIFICATE OF ORIGINALITY

I hereby declare that this thesis is my own work and that, to the best of my knowledge and belief, it reproduces no material previously published or written nor material which has been accepted for the award of any other degree or diploma, except where due acknowledgement has been made in the text.

_____(Signed)

LAM KAI SIU (Name of student)

Abstract

A composite system, comprising an electrostrictive thermoplastic elastomer Polyurethane (PU) and a ferroelectric ceramic Lead Zirconate Titanate (PZT) has been investigated in this project. This material system exhibits various features that have attracted both scientific interest and attention for engineering applications. The present work aims at the study of the electrostrictive and the pyroelectric properties of these PZT/PU composites of various ceramic contents. The full understanding of their properties can help us design prototype devices based on these composites for sensor and actuator applications.

0-3 composites of PZT/PU with various ceramic volume fractions were prepared by extrusion. The samples for characterization were produced by hot pressing. The microstructures of the samples were studied by different techniques including scanning electron microscopy, X-ray diffraction and Fourier transform infrared spectroscopy. Other physical properties such as dielectric permittivities, resistivities and thermal conductivities of the samples which affect electromechanical and pyroelectric performance have been determined. It is interesting to point out that the measured pyroelectric coefficients of the composites increase almost linearly with the volume fraction of the PZT inclusions, which in general is not the case. A model is proposed to provide an explanation of such a relationship.

Based on the measured physical properties of the composites, samples of 26% and 30% PZT were chosen as pyroelectric sensor elements. This responsivity and detectivity were measured with a chopped light source and a lock-in amplifier.

The electrostriction of the composites was measured by a modified Michelson interferometer. Quasi-static fields were applied across the samples when strains and displacement currents were measured simultaneously. It was found that the electrostriction of the composites was dependent on the ceramic volume fraction. Switching in the electrostrictive strain of the samples was also observed. It occurs at a critical field which decreases with the PZT content. Electrode clamping can affect the electrostriction performance. By using compliant electrodes (a mixture of carbon black and silicone) instead of metallic electrodes, an enhancement in the electrostriction of PU was obtained. Electrostrictive bending is another interesting feature that was observed in pure PU and PZT/PU composites. Several types of bending actuators with a combination of PU and PZT/PU composite were fabricated and their bending performances were studied. Hysteretic bending response was observed. The bending mechanisms of these actuators are also discussed in this thesis.

Acknowledgements

I would like to deeply thank my chief supervisor Dr. Y. W. Wong for his excellent guidance, constant encouragement and invaluable advice throughout the whole study period. I am also grateful for his suggestions regarding the content, organization and proof reading of this thesis.

I would particularly like to thank my co-supervisor Prof. F. G. Shin for fruitful discussion and invaluable suggestions on both experimental and theoretical aspects in my research work.

My special thanks are also extended to Dr. Y. M. Poon, Dr. Bernd Ploss and Mr. L. S. Tai for their support and helpful suggestions.

It is my pleasure to thank Dr. F. T. Cheng and Dr. K. H. Wong for their encouragement during my whole study period. Thanks also go to Mr. S. H. Choy and Mr. Y. T. Or for their helpful assistance, discussion and support in my work.

I gratefully acknowledge all my classmates, research personnel and technicians in the Department of Applied Physics and the Materials Research Centre (MRC) of The Hong Kong Polytechnic University who have so often offered me assistance in all

aspects of my study.

I truly appreciate the continual encouragement, support and understanding from my family and from my best friends Miss M.K. Cheung and Mr. K.F. Fung.

Finally, I would like to acknowledge the financial support from the Research Grants Council (RGC), under the research grant of A/C No. 5143/01E, and miscellaneous support from the Centre for Smart Materials of The Hong Kong Polytechnic University.

Table of Contents

List of Figures

List of Tables

Chapter 1

Introduction

1.1 Background

Composites of polymer matrix of negligible electrostriction blended with piezoelectric ceramics have been well studied and widely applied in various areas [Skinner et al., 1978; Newnham et al., 1980; Kim et al., 1994; Dias et al., 1996; Clegg et al., 1997]. Despite the complicated behavior of such composites in the high electric field regime, their properties in the low electric field regime can be correctly predicted to a certain extent. On the other hand, composite made by blending polymers of large electrostriction with piezoelectric ceramics is a new class of materials which has yet to be investigated extensively. They may provide novel applications that have not been achieved by traditional ferroelectric ceramic-polymer composites.

Recently, a composite material which consists of a ferroelectric ceramic, Lead Zirconate Titanate (PZT), and a thermoplastic elastomer of large electrostriction, Polyurethane (PU) [Wong et al., 2001(a); Wong et al., 2001(b); Wong et al., 2002; Sakamoto et al., 2000], has been studied. One of the unusual features of this composite observed by Wong et al. is the switching electromechanical response at an applied

electric field above a critical value, which provides new possibilities in electromechanical applications. In addition, the large electromechanical strain found in the PU thermoplastic elastomer [Zhenyi et al., 1994; Zhang et al., 1997] has not been fully evaluated. Thus much work can be done toward clarifying the electromechanical mechanisms as well as to further exploit the advantages provided by the elastomer and its composites in sensing and actuation applications.

Since PZT is well known for its large pyroelectric response, some studies [Yamazaki et al., 1981; Yamada et al., 1982] have shown that composites of PZT ceramics and polymer also reveal pyroelectric properties after poling. Compared with pure ceramic, the advantages of polymer composite systems are flexibility and light weight. As a result, they have received considerable attention especially in pyroelectric sensor applications. The PZT/PU system indeed exhibits pyroelectric effect as expected. The elastomeric matrix also provides suppression of vibration noise that has been a nuisance in most piezoelectric ceramic pyroelectric sensor materials.

1.2 Literature Review on PZT, PU and PZT/PU Composites

1.2.1 Lead Zirconate Titanate (PZT)

PZT is a well studied ferroelectric ceramic material. Due to the higher electromechanical coupling coefficient and the higher Curie temperature of PZT, it has been used for transducer applications [Mason, 1964]. Besides, it is easily poled and possesses a large range in dielectric constant depending on the dopants [Haertling, 1999].

In the research of Furukawa [Furukawa et al., 1990], the electric field induced strain in the thickness direction and the corresponding *D-E* loops were measured at the same time. Ferroelectric switching occurred when the applied sinusoidal electric field was high enough and the induced strain drew a hysteresis loop of butterfly shape. In the butterfly strain-field loop, switching was observed at about 1 MV/m at a strain of -0.2%. The strain then increased to 0.1% when the electric field was at 1.5 MV/m and dropped steadily back to zero when the field decreased to zero. On the other hand, the conventional D-E hysteresis loop was obtained in the electric displacement measurement. The coercive field and the remanent polarization were found as 1.5 MV/m and 35 $\mu C/cm^2$ respectively.

In the work of Kholkin [Kholkin et al., 1996], the electric field dependence of

piezoelectric response of PZT film was measured by using double-beam interferometry They showed that the piezoelectric response was almost constant at 50 pm/V in the frequency range from 10^2 Hz to 10^5 Hz as expected from the low-signal piezoelectric coefficient of PZT [Zhang et al., 1988; Zhang et al., 1989]. On the other hand, for low applied field, the strain was a linear function of electric field. The typical butterfly-type strain hysteresis loop was also obtained when the applied field was high enough.

1.2.2 Thermoplastic Polyurethane (PU)

In recent years, a lot of research effort was devoted to electrostrictive thermoplastic polyurethane (PU) elastomers. PU was reported to exhibit large electric field induced strain and this (non-ferroelectric) material exhibited a quadratic relation between applied electric field and strain [Zhenyi et al., 1994]. In Zhenyi's work, three separate measurement techniques (accelerometer, double beam leaser interferometer and capacitance measurement) were used to test the thickness response on Dow polyurethane (PT6100S). A maximum strain of 3% was found at a field of 20 MV/m by using a capacitance measurement system. However, for films with gold electrodes, only about 1% and 0.6% strain were obtained by using the capacitance measurement system and laser interferometer system respectively. The corresponding electrostriction coefficient M was found in the range from $-1.63\times10^{-17}\ m^2/V^2$ to $-3.3\times10^{-17}\ m^2/V^2$. It was suggested that the large electrostrictive response was in fact greatly reduced due to the surface constraints imposed by the stiffness of electrodes.

Based on the electrode clamping effect, Su et al. [Su et al., 1998] developed an all-polymer electrostrictive soft film by depositing conductive polypyrrole (PPy) directly on both sides of the solution-cast electrostrictive polyurethane elastomer film. Such films were flexible with strong adhesion between the PU and PPy electrodes. The sheet resistivity of the PPy electrode was about 1000 Ω/m. Compared with films coated with metallic electrodes, the compatibility at the interface between PPy and PU significantly improved the acoustic and optical transparency of these all-polymer films. Moreover, they also exhibited dielectric properties and electrostrictive characteristics comparable to those of films with gold electrodes under identical measurement conditions.

The electromechanical response of the polyurethane elastomers (Dow 2101-80AE) was studied by Zhang et al. [Zhang et al., 1997], at room temperature and in the temperature range near its glass transition. The Maxwell stress raised significant contribution to the strain response at temperatures higher than the glass transition temperature especially for high elastic compliance materials (from 10^{-7} to 10^{-8} m^2/N). They also reported that the strain response M (electrostriction coefficient) was -2.2×10^{-18} m^2/V^2 at room temperature and 10 Hz, but the Maxwell stress contributed about 50% to M. Furthermore, PU exhibited a very large electrostrictive coefficient Q_{33} (-150 to -450 m^4/C^4); it was about two orders of magnitude greater than that of polyvinylidenefluoride (PVDF). It was also found that the chain segment motions in this polymeric material could be divided into two parts, one related to the polarization and the other to mechanical response, and the overlap between the two motions yielded the

electromechanical response of the material. The activation energies for the two types of chain segment motion could be different, resulting in different relaxation times in the dielectric, elastic compliance and electrostrictive responses observed in the PU elastomers.

Su et al. [Su et al., 1997(b)] studied the dependence on temperature and frequency of the electromechanical properties of PU (Dow 2103-80AAE). They discussed the strain contributions from the Maxwell stress effect and electrostrictive effect. They found a decrease in the Maxwell stress contribution at higher frequencies. Moreover, the Maxwell stress contribution increased markedly at the glass transition (~-20°C), along with sharp increases in the elastic compliance and dielectric constant. The electrostrictive effect exhibited an increase at another transition temperature, at 75°C. From thermal and chemical structural analyses such as differential scanning calorimetry (DSC), thermal expansion (TE) and Fourier transform infrared (FTIR) investigations, they indicated that the phenomena observed at these transition temperatures were the reflections of the molecular motions of the soft segment and the extension in hard segment. Therefore, they suggested that the chain-segment motions could be grouped into those related to polarization, those related to the elastic process and those related to both. These conclusions may be helpful to explain the observed electrostriction of PU.

1.2.3 Electrostrictive Bending Effect of Polyurethane (PU)

In recent years, some research groups showed that polyurethane film exhibited not

only electrostriction in the thickness direction but also bending deformation when an electric field was applied across the thickness of the film.

There were many works about the bending of PU investigated by the group of Watanabe et al. One of their works [Watanabe et al., 1997] showed that the horizontal bending displacement of a monolayer PU film (0.5 mm in thickness and cut into 5×30 mm) suspended vertically was proportional to the square of the applied electric field. The maximum displacement was about 0.15 mm under a field of 2 MV/m. In addition, they also showed that by applying two repeated electric field pulses, the bending displacement increased gradually during the first application but rapidly during the second application. They claimed that the rapid second deformation was caused by the electrostriction which was asymmetric to the polarity.

In addition, PU films were shown to bend toward the cathode side and exhibited memory effect in the bending displacement when an electric field was applied across the film [Watanabe et al., 1999(a)]. They also examined that a force of about 40 mgf was generated by the PU film under an applied field of about 12 MV/m. The bending memory effect was investigated by measurement of the current density and thermally stimulated discharge current [Watanabe et al., 2001(a)]. It was found that the bending direction of the film was not changed when the polarity of the electric field was reversed. Besides, hysteresis in the bending electrostriction was detected and was ascribed to ionic polarization of the ionic impurities contained in the film. The ionic polarization formed by a prior electric field influenced the next bending electrostriction.

The prior application of an electric field significantly improved the response speed and controlled the bending direction. In another paper [Watanabe et al., 1999(b)], they found that the expansion of the anode surface was much larger than that of the cathode surface so the film bent to the cathode side. The expansion of the anode surface was concluded to be related to the electric conduction of the PU film. Besides, they also found that the bending displacement was reduced when the ionic impurities were removed from the film [Watanabe et al., 1999(c)]. On the other hand, the bending direction of the PU film could be changed by adding a small amount of lithium bromide in the film. They also investigated the mechanism of the bending electrostriction in PU by using in situ ultraviolet to visible (UV-vis) spectroscopy that enabled them to obtain the UV-vis spectra of the PU film under the application of electric field [Watanabe et al., 2000]. The obtained spectra which showed reversible absorption that appeared during the application of the electric field and disappeared with its removal. They suggested that the absorption was related to charge injection which was the cause of the bending electrostriction.

The bending displacement and direction of the PU film could be enhanced and controlled by doping with salt [Watanabe et al., 2001(b); Watanabe et al., 2001(c)]. The cations of the salt influenced the field-induced expansion of the cathode surface. However, anions of the salt influence the expansion of the anode surface. It was believed that both cations and anions affect charge injection; doping with salt increased the conductivity of the film and promoted charge injection.

The bending displacement could also be enhanced by using wrinkled polypyrrole electrodes [Watanabe et al., 2002]. The bending displacement of a doped PU film with wrinkled PPy electrodes was about five times that of an undoped PU film with gold electrodes under the action of a 2 MV/m electric field for 300 s. However, the response time of the film with PPy electrodes was much slower (reach 0.5 mm in 100 s) than that with gold electrodes (reach 0.5 mm in a few seconds).

The variation of bending displacement of doped PU films with different metallic electrodes was also investigated in some other papers [Ueda et al., 1997; Kyokane et al., 1999].

1.2.4 Electrostriction of PZT/PU Composites

The literature on investigations of the electrostriction of PZT/PU composites is limited.

In the recent work of Wong et al. [Wong et al., 2001(a); Wong et al, 2001(b)], electrostriction and related properties of PU and its composites with PZT of various volume fractions were investigated. The PZT/PU composites were prepared by rolling. From the X-ray diffraction (XRD) profiles, polarization peaks of PZT ceramic could be observed even for the composition only with 2% volume fraction of PZT. The elastic moduli and the dielectric permittivities of the composites increased with increasing PZT contents. The inclusion of PZT in the PU matrix constrained the elastic deformation of

PU thus resulting in a higher stiffness. Besides, the relative permittivity of the composites followed the asymmetric Bruggeman model reasonably well. The electrostriction of the pure PU and PZT/PU composites with 2% PZT volume fraction followed a simple quadratic relation with the applied electric field. For the composites with higher PZT volume fraction, switching of strain was obtained under the application of a higher electric field. The switching fields decreased with increasing volume fraction of PZT. The switching results could be considered as the combined effect of the contraction of PU and the polarization reversal of PZT.

The switching phenomenon in a PZT/PU composite could be simulated by a simple model [Wong et al., 2002] that included the effect of interfacial charge on polarization switching of PZT particles in the composite. The model can help explain why the PZT polarization is switched at electric fields much smaller than expected.

1.2.5 Dielectric and Pyroelectric Properties of PZT/PU Composites

Reports about the electrical, dielectric and pyroelectric properties of PZT/PU composites were mostly published by the group of Sakamoto et al. In their group, the PZT/PU composites were prepared from PZT ceramic powder mixed with PU of vegetable origin made from the reaction of isocyanate and ester of ricinoleic acid. The composites were obtained in thin film form by the spin-coating method. In their recent works [Sakamoto et al., 1998; Sakamoto et al., 2002], the dielectric permittivities ε of the composites with various PZT volume fractions were measured at different

frequencies and temperatures. Besides, the pyroelectric coefficients p of the composites were obtained by using the thermal stimulated discharge current measurement. The results showed that both the dielectric permittivity at 1 kHz and the pyroelectric coefficient increased with increasing PZT content. Moreover, the dielectric permittivity increased with increasing temperature and decreased with increasing frequency. The dielectric constant of the composite with 32% volume fraction of PZT measured at 1 kHz and 343 K was about 23 while the pyroelectric coefficient at this temperature was 6×10^{-5} $Cm^{-2}K^{-1}$. As a result, the pyroelectric figure of merit p/ε was 1.5 times higher than that of PZT/PVDF (50 vol. %) [Das-Gupta, 1991] and six times higher than that of pure PZT.

In another work [Sakamoto et al., 1999(a)], the piezoelectric constant d_{33} of a PZT/PU composite with 33% volume fraction of PZT poled at different temperatures and under different applied electric fields was measured [Zimmerman, 1975]. The highest d_{33} value was obtained as 24 pC/N when the composite was poled at 12MV/m and 383 K. [Sakamoto et al., 2000]. The remanent polarization and the coercive field as determined from the hysteresis P-E loop were 0.09 C/m^2 and 3.4 MV/m respectively.

The voltage output of a temperature sensor with a PZT/PU composite (with 32% volume fraction of PZT) as sensor element was measured under a periodic variation of temperature by a lock-in amplifier [Sakamoto et al., 1999(b)]. They found that the voltage output of the composite sensor decreased inversely with frequency. In addition, the voltage output increased with decreasing thickness of the composite. A maximum

voltage output of 0.1 V was generated from a 80 μm-thick sample at 10 Hz.

1.3 Scope of This Study

The main objective of this project is to study the electromechanical and pyroelectric responses of PZT-filled polyurethane composites as well as to fabricate some prototype devices based on PU and PZT/PU composites such as single film or bimorph bending actuators and flexible pyroelectric sensors.

This thesis includes the preparation process of the PZT/PU composite samples with varying ceramic volume fraction. Measurements of the dielectric, pyroelectric and the electromechanical properties are then described. Comparison of the experimental results with theoretical values is also presented. Finally, some prototype devices based on the composites are constructed and their performances are examined.

There are eight chapters in this thesis. Chapter 1 introduces PZT/PU composites. A literature review on PZT, PU and PZT/PU composites is also included in this chapter. Some theories and experimental methodologies are described in Chapter 2. The preparation and characterization of samples are shown in Chapter 3.

Chapter 4 shows the dielectric and pyroelectric properties of the PZT/PU composites. A theoretical model is also provided to describe the relationship between the pyroelectric coefficient and the PZT content. Other thermal properties, such as specific heat capacity, thermal diffusivity and thermal conductivity are introduced in

Chapter 5. Prototype pyroelectric sensors and their performance are also presented in this chapter.

The electrical and electromechanical responses of pure PU, PZT and PZT/PU composites are shown in Chapter 6. The effect of compliant electrodes constructed from mixing carbon black and silicone sealant is also discussed in this chapter.

The fabrication of some bending actuators based on PU and PZT/PU composites is presented in Chapter 7. A bending mechanism of the PU film is also introduced.

Finally, a conclusion of the whole project and some suggestions for future work are mentioned in Chapter 8.

Chapter 2

Theoretical Aspects and Experimental Methodology

2.1 Electromechanical Mechanisms

2.1.1 Piezoelectric Effect

Piezoelectric effect was discovered by Pierre Curie and Paul-Jacques Curie in 1880. It was manifested in the phenomena observed in certain types of crystals in which electrical energy was converted to mechanical energy or vice versa [Jaffe et al., 1971]. It is a linear electromechanical effect that the mechanical strain S and stress X are linear with the electric field E and electric displacement D respectively. That is,

$$S = dE \tag{2.1}$$

$$D = dX \tag{2.2}$$

where d is the piezoelectric coefficient.

The effect in Equation 2.1 is often known as the converse piezoelectric effect in which the sample contracts or expands under the application of electric field and in Equation 2.2 as the direct piezoelectric effect in which charges are generated when

appropriate stresses are applied to the sample. These effects are due to the noncentrosymmetric crystal structure of the materials. They commonly have a perovskite ABO_3 crystal structure. The ABO_3 structure is a face-centered cubic (FCC) structure that consists of a large cation (A) at the corners, a small cation (B) in the body center and oxygen in the center of the faces [Damjanovic, 1998]. Lead Zirconate Titanate $Pb(Zr,Ti)O_3$ (PZT) is of this structure having lead atoms located at the corners, and zirconium or titanium atoms located at the body center randomly. Depending on the atomic ratio of zirconium to titanium, PZT can exist in either the tetragonal, rhombohedral or orthorhombic phase at room temperature as shown in Figure 2.1. In these phases, the unit cell elongates in one direction, causing the center atom (Zr or Ti) to shift towards one of the oxygen atoms in the direction of elongation as shown in

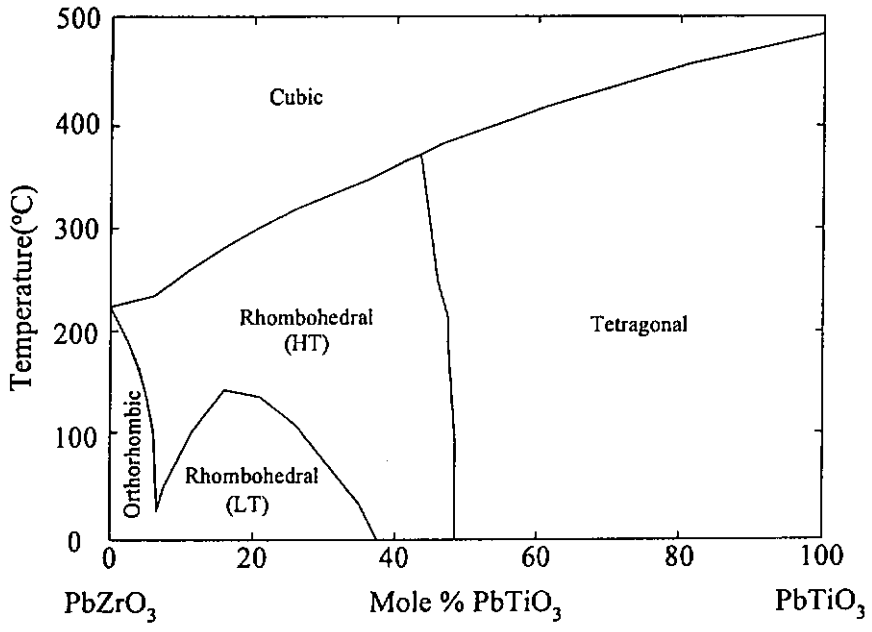

Figure 2.1 Phase diagram of PZT illustrating how the Zr/Ti ratio and temperature affects the phase of the ceramic [Jaffe et al., 1971].

Figure 2.2. As a result, one end of the long axis is more positive than the other end, and then a dipole moment and hence a polarization is produced in the unit cell. When the PZT sample heats above the Curie temperature T_c, which is different for PZT with different Zr/Ti ratio, the unit cell will transform to a cubic phase.

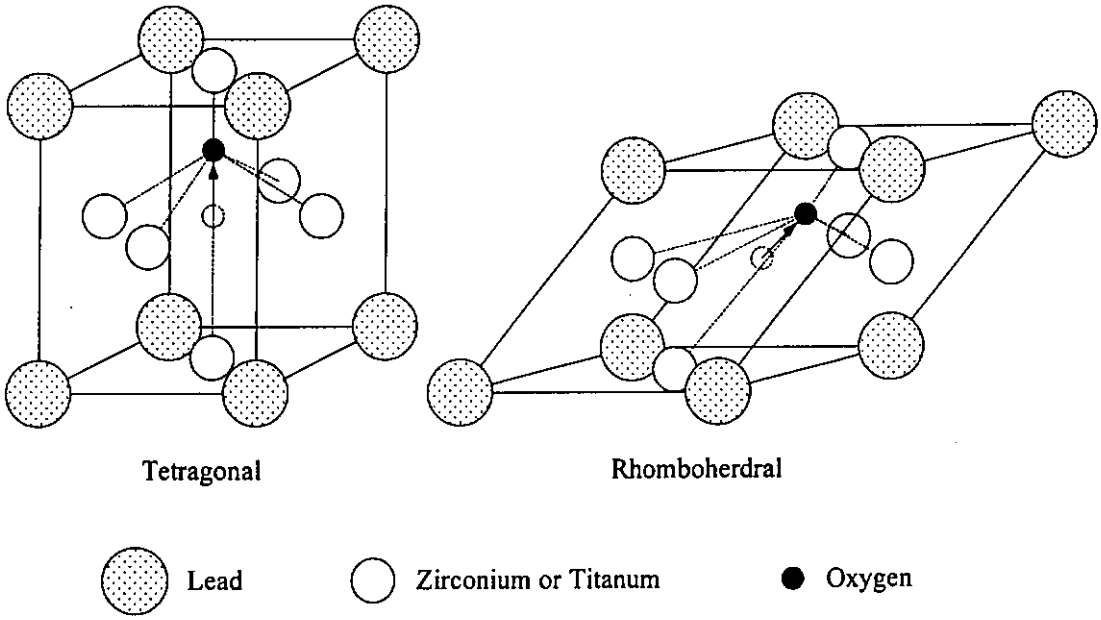

Figure 2.2 The tetragonal and rhombohedral unit cells of PZT.

By adding the linear elastic (Hook's law) and dielectric relations to Equation 2.1 and 2.2 respectively and writing them in the full tensor form, the piezoelectric constitutive equations [Nye, 1987; IEEE Standard on Piezoelectricity, 1988] are obtained as,

$$S_{ij} = d_{kij} E_k + s^E_{ijkl} X_{kl} \tag{2.3}$$

$$D_i = \varepsilon_{ik}^X E_k + d_{ikl} X_{kl} \tag{2.4}$$

where s_{ijkl}^E is the elastic compliance, ε_{ik}^X is the dielectric permittivity, and $i, j, k, l = 1$ to 3. The superscripts E and X refer to the condition under which these quantities are measured. That means compliance is measured under a constant electric field and dielectric constant under a constant stress.

2.1.2 Electrostriction Effect

When an electric field is applied to a dielectric material, it produces a strain proportional to the square of the field. This effect is called the electrostrictive effect [Xu, 1991]. Electrostrictive effect is a quadratic effect and the electrostrictive strain is not related to the sign of the applied field. Unlike the piezoelectric effect, electrostriction may occur in all crystals whether or not the crystals have polarity. On the other hand, the electrostriction effect that is a quadratic dependence of strain or stress on the polarization P exists in all polymers [Yoseph, 2001],

$$S_{ij} = Q_{ijkl} P_k P_l \tag{2.5}$$

where Q_{ijkl} is the charge related electrostrictive coefficient. For an isotropic polymer,

$$S_3 = Q_{33}P^2 \quad \text{and} \quad S_1 = Q_{13}P^2 \tag{2.6}$$

where S_3 and S_1 are the strains along and perpendicular to the polarization direction, known as the longitudinal and transverse strains, respectively. In Equation 2.6, the compressed matrix notation is used. In the matrix notation, ij or kl is replaced by p or q [Nye, 1987; IEEE Standard on Piezoelectricity, 1988], so

$$11\rightarrow1,\ 22\rightarrow2,\ 33\rightarrow3,\ 23 \text{ or } 32\rightarrow4,\ 31 \text{ or } 13\rightarrow5 \text{ and } 12 \text{ or } 21\rightarrow6$$

For an isotropic polymer, experimental evidence and theoretical consideration indicate that Q_{33} is negative and Q_{13} is positive [Kinase et al., 1995; Shkel et al., 1998]. Hence, for a polymer, an increase in polarization will result in a contraction along the polarization direction.

For linear dielectric polymer, the polarization is related to the dielectric permittivity as

$$P = (\varepsilon - \varepsilon_o)E \tag{2.7}$$

where ε_0 is the vacuum dielectric permittivity (= $8.85\text{x}10^{-12}$ F/m). Hence, Equation 2.7 can be converted into

$$S_3 = Q_{33}(\varepsilon - \varepsilon_o)^2 {E_3}^2 = M_{33}{E_3}^2 \tag{2.8}$$

where M is known as the electric-field-related electrostriction coefficient. For an isotropic solid, the longitudinal strain is $S_3 = M_{33}E^2$ and the transverse strain is $S_1 = M_{13}E^2$. As a result, M_{33} is negative while M_{13} is positive for an isotropic polymer. That means it will contract along the thickness direction and expand along the film direction when an electric field is applied across the thickness.

2.1.3 Maxwell Stress Effect

Besides the electrostriction effect, there is another electromechanical actuation mechanism whose strain response is also approximately proportion to the square of the applied field. That is the electrostatic force (Maxwell stress) induced strain, which can be quite significant in soft polymer elastomers. The Maxwell stress may be related to coulombic interaction between charges on electrodes which establishes the required electric field [Krakovský et al., 1999]. For an isotropic solid without mechanical constraints and with Poisson's ratio equal to one half, the expression for the Maxwell stress induced strain in the thickness direction S_3 for a dielectric material has been derived as [Yoseph, 2001]

$$S_3 = -\varepsilon s_{11} E_3^{\,2} = W E_3^{\,2} \tag{2.9}$$

where s is the elastic compliance, ε is the dielectric permittivity and W is the Maxwell stress induced strain coefficient.

2.2 Pyroelectric Effect and Ferroelectricity

2.2.1 Pyroelectric Effect

Pyroelectric effect is the appearance of an electric charge at the surface of a polar material when uniform heating or cooling changes the polarization in the polar material. When the temperature of the crystal is changed, electric charges corresponding to the change of the spontaneous polarization appear on the surface of the crystal. On neglecting magnetic effects, a variation in the electric displacement dD can be expressed as [Xu, 1991]:

$$dD = (\frac{\partial D}{\partial T})^{X,E} dT + (\frac{\partial D}{\partial E})^{X,T} dE + (\frac{\partial D}{\partial X})^{E,T} dX \tag{2.10}$$

where X, E and T are stress, electric field and temperature respectively. Under the condition of a constant stress and a constant electric field, the last two terms of Equation 2.10 vanish. The coefficient of the first term is defined as the pyroelectric coefficient p [Morgan et al., 1983],

$$p = \frac{\partial D}{\partial T} \tag{2.11}$$

D can also be written as

$$D = \varepsilon_o E + P \tag{2.12}$$

where P is the resulting polarization including the spontaneous polarization P_s and the polarization induced by electric field and stress, and ε_0 is the relative permittivity in vacuum. Under the conduction of zero electric field and stress, Equation 2.12 can be expressed as

$$D = P_s \tag{2.13}$$

Hence, the pyroelectric coefficient p can be written as

$$p = \frac{\partial P_s}{\partial T} \tag{2.14}$$

2.2.2 Ferroelectricity

Ferroelectric effect was discovered by Valasek in Rochelle salt in 1921. Most pyroelectric materials exhibit a spontaneous polarization P_s in a certain temperature range and the direction of P_s can be reversed by an external electric field. Such materials are called ferroelectric materials [Xu, 1991].

2.3 Electric Field Induced Strain Measurement

Various techniques, such as resonance, capacitance, inductance, strain gauge and interferometer methods, can be used to measure electric field induced strains in piezoelectric and electrostrictive materials. The choice of a suitable technique for a particular application depends on the geometry of the available sample, the amplitude of the displacement and the desired frequency. In this study, a Michelson interferometer is employed because of its simple construction and high resolution.

Interferometric methods of measuring displacements are well known [Steel, 1983]. Displacements in high resolution can be measured by a Michelson interferometer. Recently, the piezoelectric and electrostrictive strain in ferroelectric ceramics and polymers were investigated by using such interferometers [Zhang et al., 1988; Furukawa et al., 1990].

In this study, the electric field induced strains of the samples under investigation are measured by a modified single beam Michelson interferometer as shown in Figure 2.3. In the figure, it can be seen that a polarized He-Ne laser of 3 mW is employed as the light source of the system. After the laser beam is split into two beams, one of them goes to the sample and the other goes to the reference mirror. Then the two reflected beams recombine at the beam splitter. The interference pattern of the recombined beams is expanded by the objective lens and then detected by a linear photo-diode-array (PDA)

of 1024 elements with pixel separation 25 μm. The PDA is operated with a suitable neutral density (ND) filter that can cut off the light from background. The output signal of the PDA is converted to a fringe pattern and displayed on the computer by using a data acquisition card which maximum sampling frequency is 1.2 MHz. A change in thickness of the sample causes a change in the optical path difference and results in a shift of the fringe pattern. By recording the fringe pattern, the electric field induced strain of the sample can be calculated.

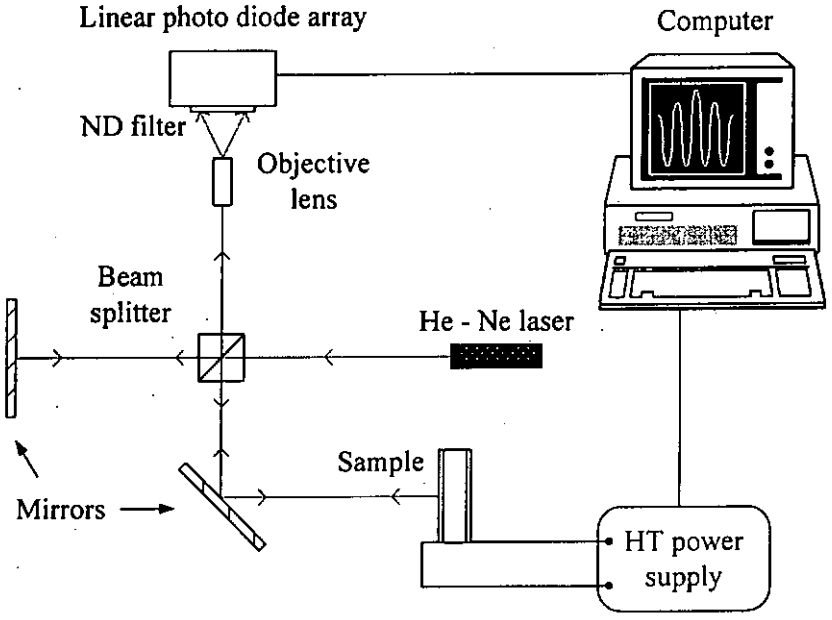

Figure 2.3 Experimental setup of Michelson interferometer.

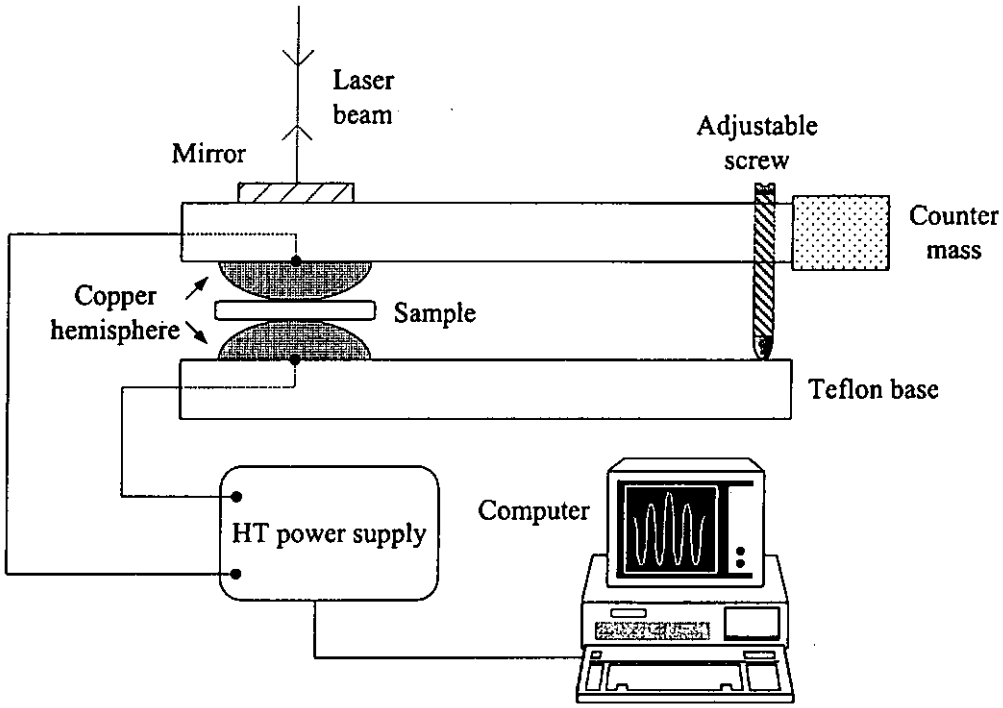

Figure 2.4 Schematic diagram of the sample holder in Michelson interferometric system.

In the measurement, the sample is placed between two copper hemispheres in the sample holder as shown in Figure 2.4. The design of point contact on the sample's surface electrodes can minimize the effect due to bending deformation problem of the sample under an application of electric field. It also allows the sample to deform freely with minimal mechanical constraints. For reducing the extra force that comes from the mass of the top copper hemisphere, a suitable counter-mass is added to the end of holder. A computer controlled high-tension power supply (Oriel 70705) is used to generate a variation of electric field between the copper hemispheres.

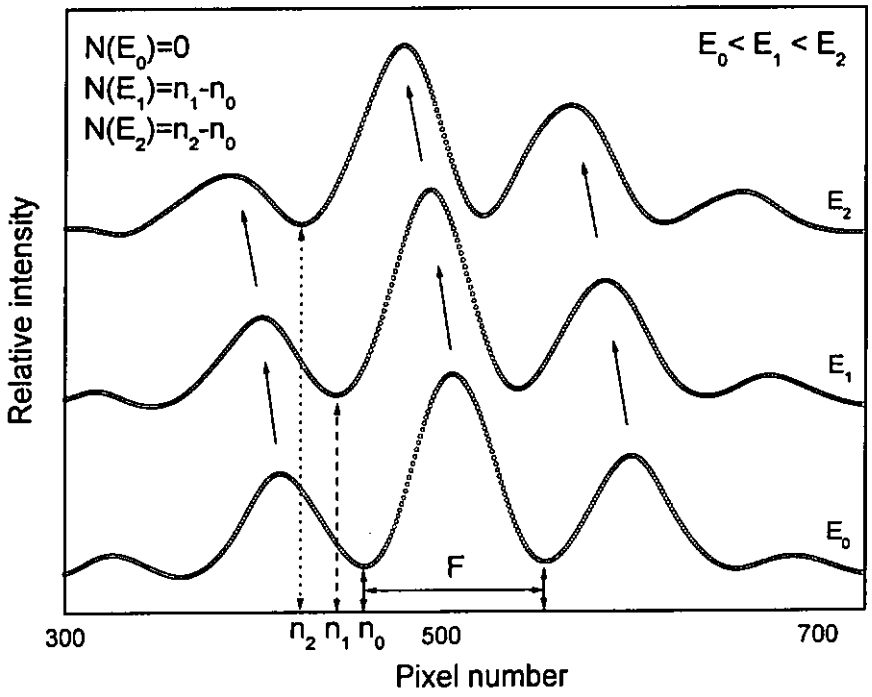

Figure 2.5 Shifting of the fringe pattern under the increasing of the electric field and the definitions of N and F in the interferometric system.

The thickness change ΔL of the sample can be calculated as:

$$\Delta L = \frac{N}{F} \times \frac{\lambda}{2} \tag{2.15}$$

where N is the shift of the interference fringe pattern, F is the separation between two consecutive fringes (Figure 2.5) and λ = 632.8 nm is the wavelength of He-Ne laser. So the electric field induced strain S of the sample can be obtained:

$$S = \frac{\Delta L}{L} \tag{2.16}$$

where L is the original thickness of the sample. For our set-up, the highest resolution of observable displacement is 1/100 fringe separation, which is about 3 nm.

To ensure the reliability of the designed interferometric system, a calibration is performed using of an ordinary PZT ceramic to determine the piezoelectric property. The PZT sample is in disc shape with thickness of 150 μm. Both of its surfaces are coated with circular aluminum electrode with diameter of 8 mm.

Figure 2.6 shows the induced strain of the PZT sample under the application of low electric field. From the slope of the linear fitting line, the piezoelectric coefficient d_{33} can be found as 600 pm/V (a value of 560 pm/V is quoted by Furukawa et al. [Furukawa et al., 1990]).

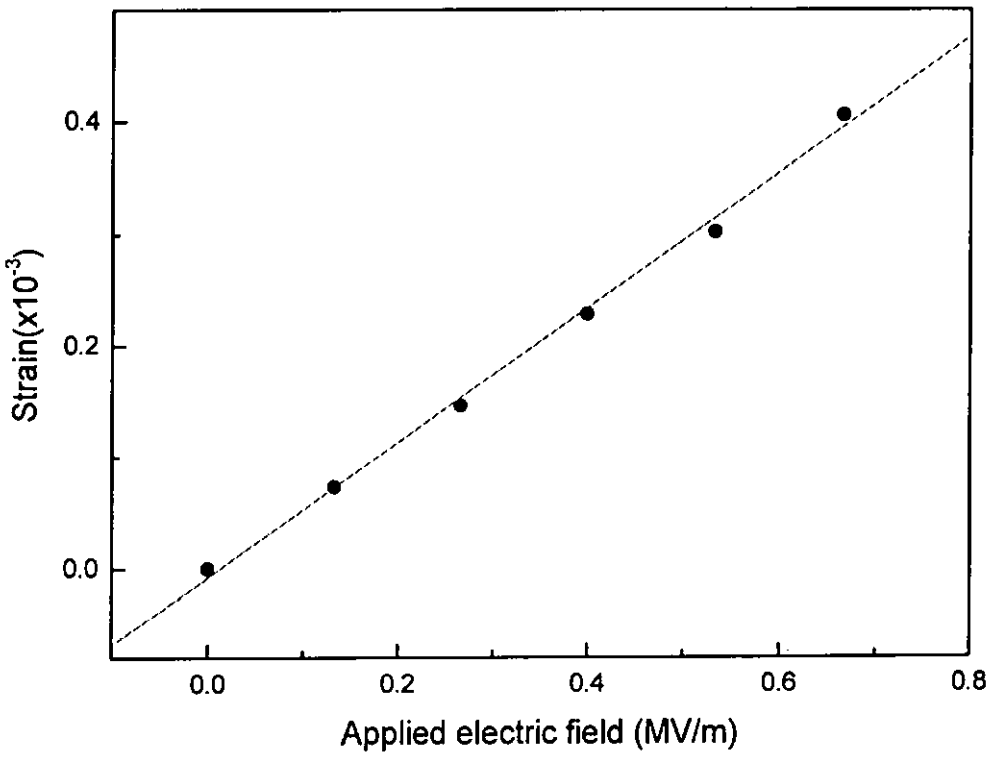

Figure 2.6 Induced strain of the PZT sample under the application of low electric field.

On the other hand, when the applied electric field is high enough, the induced strain of the ordinary PZT ceramic forms a conventional hysteresis loop of butterfly shape (Figure 2.7). It can be seen that the response of the interferometric system is fast enough to track down the fast change in displacement near the switching field at about 0.85MV/m. The details of the strain-field hysteresis loop of PZT will be discussed in Chapter 6.

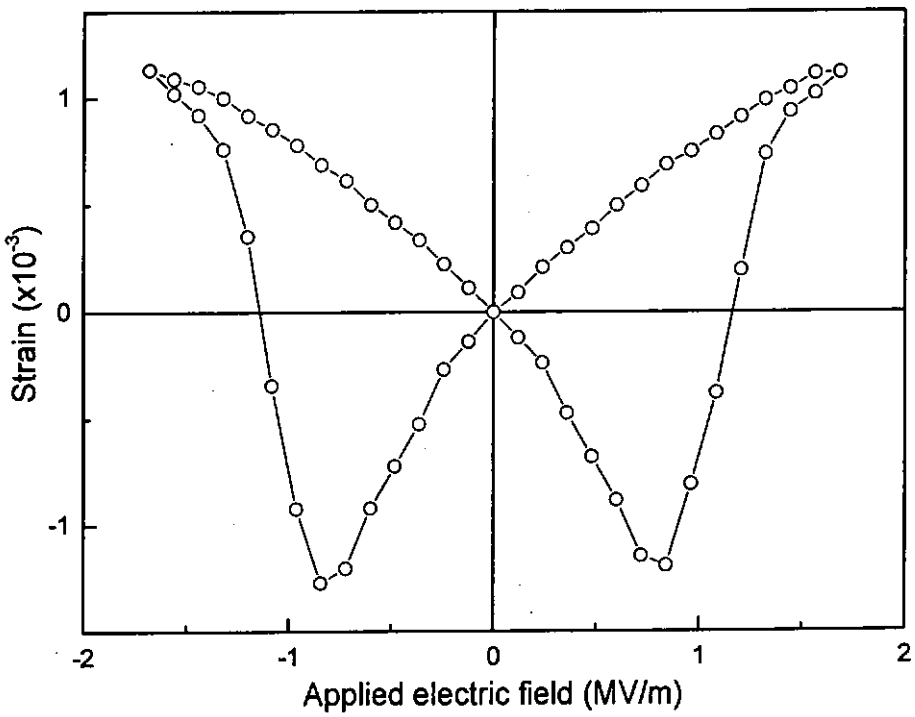

Figure 2.7 Induced strain of the PZT sample under the application of high electric field.

It can be concluded that the interferometric system we assembled is reliable and sensitive enough for the electric field induced strain measurement. It is used to study the electrostrictive effects of pure PU and PZT/PU composites. The results will be discussed in Chapter 6.

2.4 *D-E* Loops Measurement

Electric displacement hysteresis *D-E* loop is one of the important characteristics of the ferroelectric materials. Information such as coercive field and remanent polarization can be obtained from the hysteresis loop. The information is very useful for investigating the electromechanical effect of the ferroelectric material.

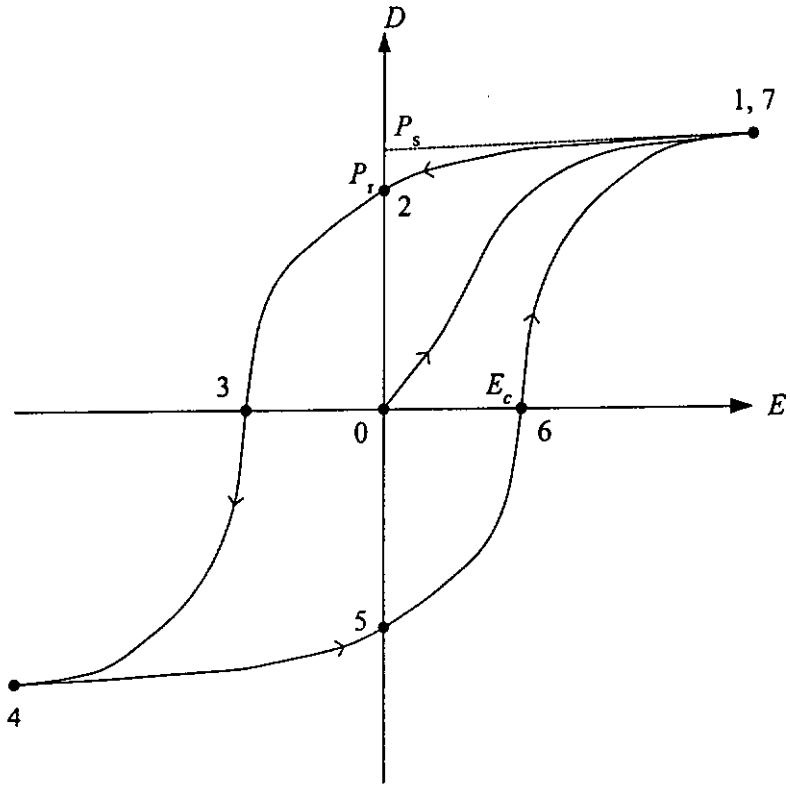

Figure 2.8 A typical ferroelectric *D-E* hysteresis loop.

Figure 2.8 shows a typical *D-E* hysteresis loop of a ferroelectric. A linear relationship between the polarization P and the applied field E is obtained when a small positive electric field is first applied to an unpoled ferroelectric material, because the electric field is not large enough to switch any domain; hence the crystal behaves as a normal dielectric material. When the electric field strength increases, some of the domains (which have a polarization opposite to the direction of the field) can be switched over in the direction along the applied field (positive direction). At that moment, the polarization increases rapidly until all the domains are switched or aligned in the field direction. As a result, a non-linear increment of P occurs. P becomes saturated (point 1) if the field is further increased. When the field is decreased, the polarization decreases to point 2 but does not return to zero at zero field. That means some of domains remain aligned in the positive direction and this polarization is defined as remanent polarization P_r. On the other hand, the extrapolation of the linear saturation segment to the polarization axis is defined as spontaneous polarization P_s. In addition, the remanent polarization can be removed when an applied field in the opposite direction reaches a certain value (at point 3). This strength of the field required to reduce the polarization to zero is called the coercive field strength E_c. As the reverse field is further increased, P will become saturated again at point 4. Then a negative remanent polarization is obtained by decreasing the reverse electric field to zero (point 5). A complete polarization hysteresis loop (point 1 to 7) can thus be obtained by repeating the process by cycling the applied field.

The distinction between P_r and P_s is that P_r is the resultant net polarization after the application of a large enough electric field (poling), while P_s is the maximum polarization that a ferroelectric material may possess.

In this study, the *D-E* loop of the samples is measured quasi-statically using the setup as shown in Figure 2.9.

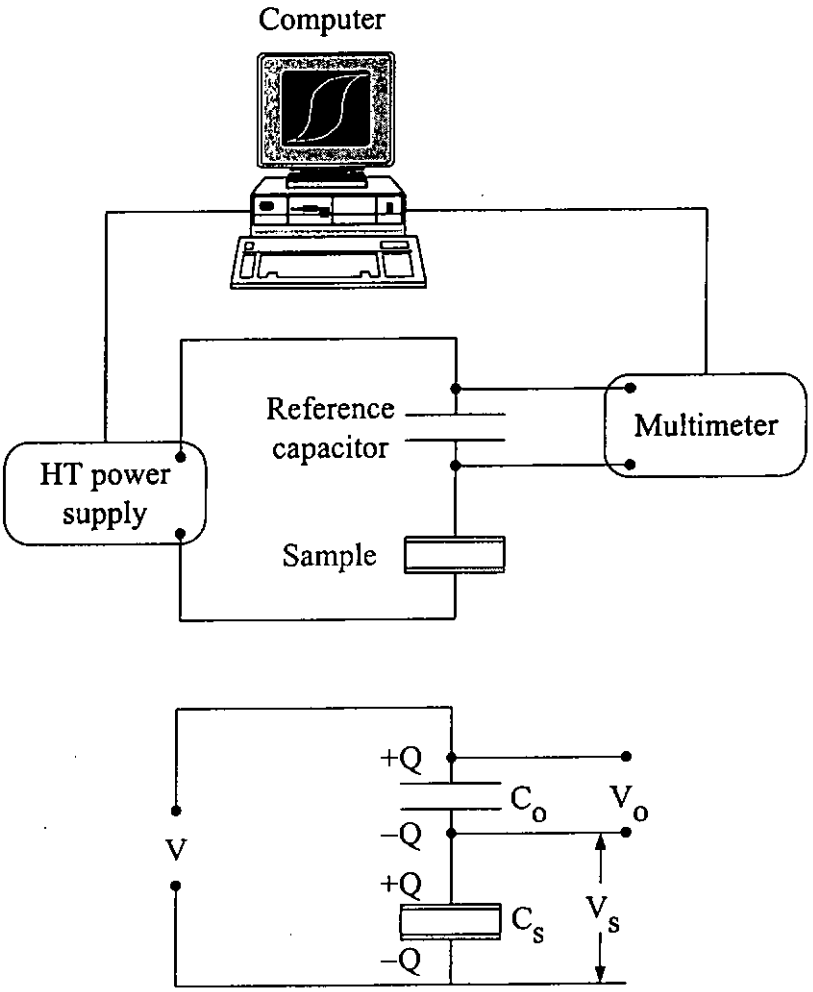

Figure 2.9 Setup and the circuit diagram of the *D-E* hysteresis loop measurement.

In Figure 2.9, it can be seen that a reference capacitor is connected in series with the sample. When an electric field is applied across the sample, a certain amount of charge Q corresponding to the change in the polarization will be induced on the sample's surfaces. At the same time, the same amount of charge will also be induced on the surface of the reference capacitor. Therefore the electric displacement D can be obtained from the following equation:

$$D = \frac{Q}{A} = \frac{C_o V_o}{A} \tag{2.17}$$

where A is the sample electrode area, C_o and V_o are the capacitance and the voltage across the reference capacitor respectively.

On the other hand, if the capacitance of the sample C_s is much smaller that C_o, then a large part of the voltage will be dropped across the sample ($V_s >> V_o$). Then the electric field E applied across the sample can be approximated by V/d_o, where V is the voltage provided by the power supply and d_o is the sample thickness. As a result, the D-E loop can be obtained by measuring V_o under the variation of V.

To verify the setup, quasi-static D-E loops of an ordinary PZT sample were measured by this setup and a traditional Sawyer-Tower bridge respectively. In both measurements, a 5 μF reference capacitor was used while the capacitance of the ordinary PZT sample was about 5 nF. In addition, the duration of each voltage step in

the quasi-static measurement was 1s while the voltage supply in the tradition Sawyer-Tower bridge measurement was driven by a 1 Hz triangular wave. The results are shown in Figure 2.10.

In the Figure 2.10, it can be noted that the same remanent polarization P_r of about 31 $\mu C/cm^2$ is obtained which is very close to the value (32 $\mu C/cm^2$) quoted by Furukawa et al. [Furukawa et al., 1990]. However, the coercive field E_c measured by the quasi-static setup is about 0.85 MV/m and that measured by the tradition Sawyer-Tower bridge is about 1 MV/m (the latter is the same as that reported by Furukawa). As longer time is provided for the switching of polarization in the quasi-static measurement, more dipoles can be switched in a lower electric field and this is why a lower coercive field is obtained. In addition, the coercive field measured in the quasi-static is exactly equal to the switching field in the strain-field measurement. It can be concluded that the quasi-static *D-E* loop measurement setup is reliable and it is suitable for investigating the electromechanical effect of ferroelectric material. Measurements on other samples and the limitation of such measurements will be introduced in Chapter 6.

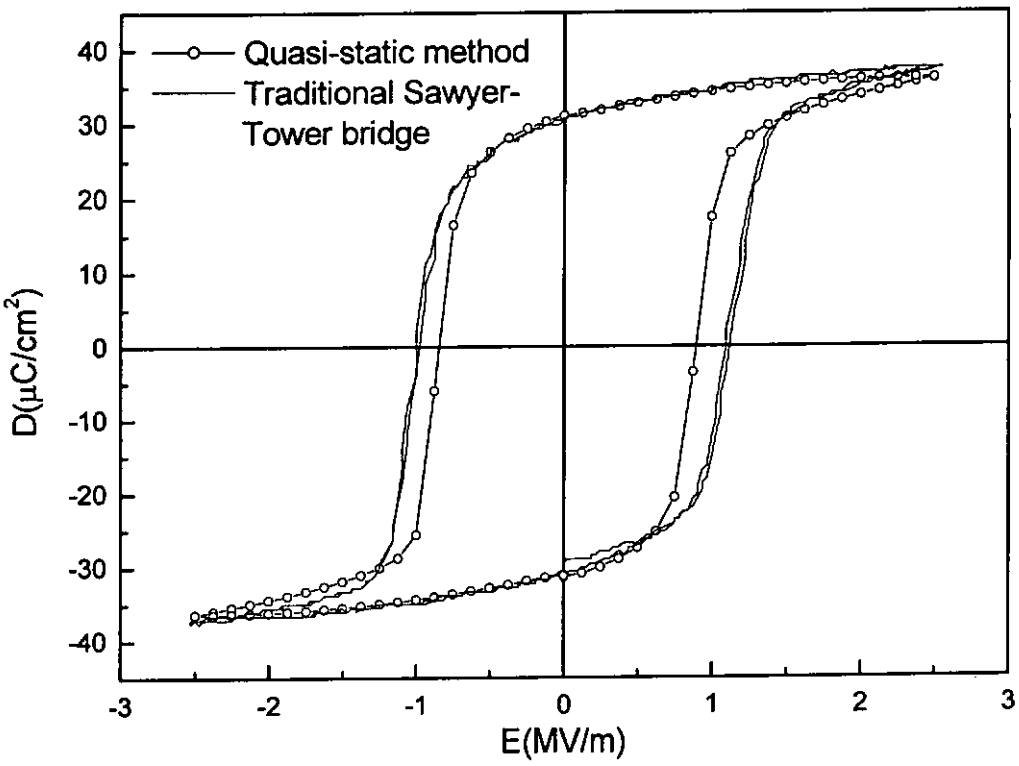

Figure 2.10 *D-E* loops of the ordinary PZT sample measured by a quasi-static method and a traditional Sawyer-Tower bridge.

Chapter 3

Sample Preparation and Characterization

3.1 Sample Preparation

3.1.1 Preparation of PZT Powder

The pre-sintered PZT powder (Navy Type II 502) was purchased from Piezo Kinetics. This type of PZT powder is designed for applications that require high electromechanical activity and high dielectric constant.

The pre-sintered PZT powder was placed into a ceramic crucible and put into a high temperature furnace (Carbolite RHF1600). Then the PZT powder was heated to 550°C at a heating rate of 5°C/min and kept for 2 hours followed by natural cooling to room temperature. This process was used to remove any polymer binder that might be present in the as-received PZT powder. As carbon monoxide was easily produced from organic substances such as the polymer binder at high temperature, sufficient oxygen should be provided during this process. Otherwise, the carbon monoxide would react with lead oxide and the lead content in the PZT powder would be reduced. For keeping the lead content, the ceramic crucible was not covered in the binder removing process.

After removing the organic binder, the PZT powder was then heated at a heating

rate of 5°C/min to 850°C for calcination for 2 hours. The temperature was further raised at a heating rate of 3°C/min to 1280°C for sintering for 1 hour. The powder was then allowed to cool naturally to room temperature in the furnace. For preventing excessive loss of lead at temperatures above 800°C, the ceramic crucible was covered during the sintering process. The time profile for the process is shown in Figure 3.1.

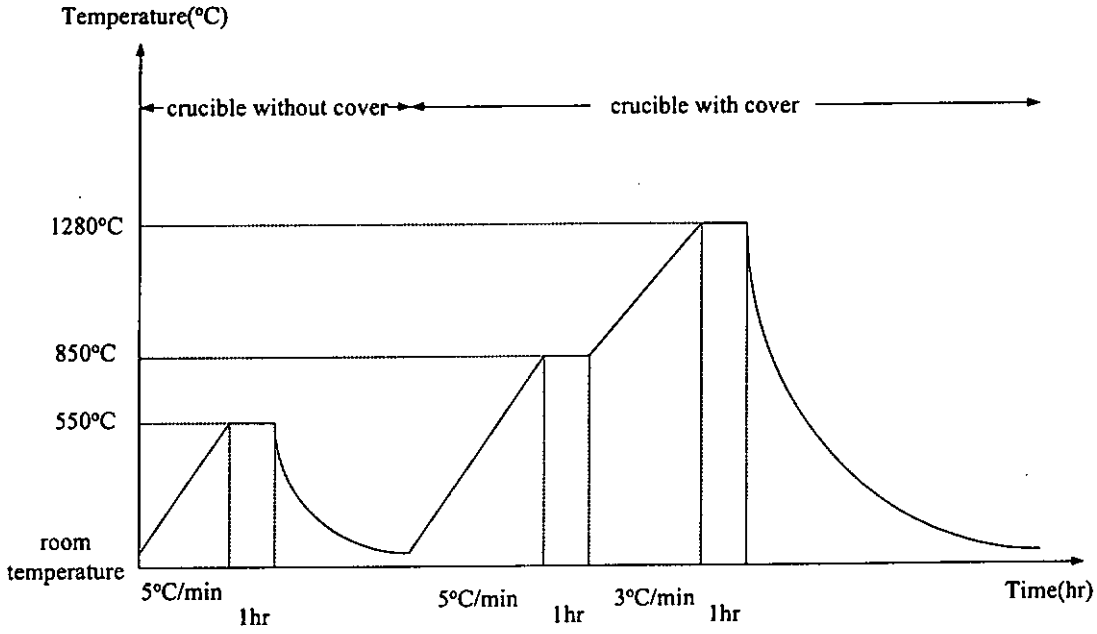

Figure 3.1 Time schedule for heat treatment of PZT powder.

The sintered particles were ground by a ball grinder for 4 hours. In order to obtain a finer powder, initial crunching was needed. Then the ball-milled powder was dried in an oven at 100°C for 12 hours. For reducing aggregation, the dried powder was then hand-milled. The preparation process for the PZT powder is summarized in Figure 3.2.

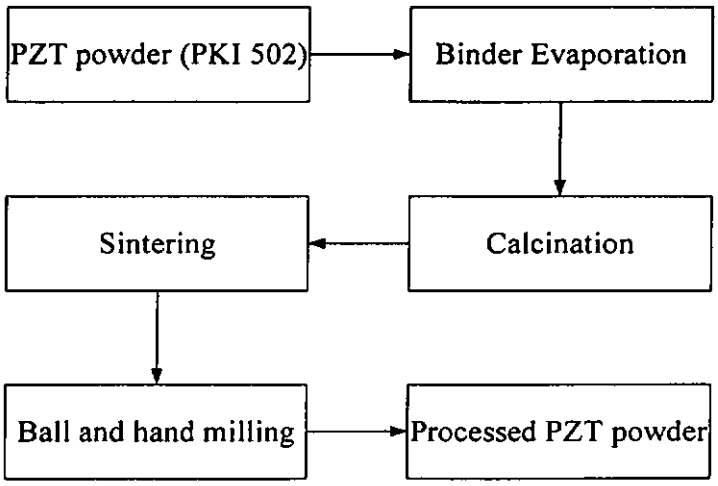

Figure 3.2 Preparation of PZT powder.

3.1.2 Preparation of PU and PZT/PU Composites

In this project, a thermoplastic PU was used. It is softens at about 120°C and is soluble in dimethylformamide (DMF). So PU and PZT/PU composite films can be prepared by hot-pressing, extrusion, or solution-casting. However, for the solution-cast process, particle aggregation is serious in samples with high PZT content. In order to have a better dispersion for PZT powder, the extrusion method was used for the preparation of PZT/PU composites.

Thermoplastic PU pellets were obtained from Dow Chemical (Dow 2103-80AE). They were oven-dried at 50°C for 12 hours before processing. A measured amount of the processed PZT powder was premixed with the dried PU pellets in a grinder, and the

mixture was blended in a single screw extruder (Rancastle RCP0250). The block diagram of the single screw extruder, equipped with a 1/4" screw and a 1 × 40 mm rectangular die, is shown in Figure 3.3. The PZT/PU composites were extruded as a long rectangular sheet. The barrel temperature settings in the four zones and the screw speed of the extruder for fabricating the composites are listed in Table 3.1. The composite sheet was then cut into pellets and refilled into the single screw extruder again for a second extrusion for the homogenizing. Finally, the PZT/PU composite pellets with 2, 5, 13, 18, 26 and 30% in volume fraction of PZT were obtained.

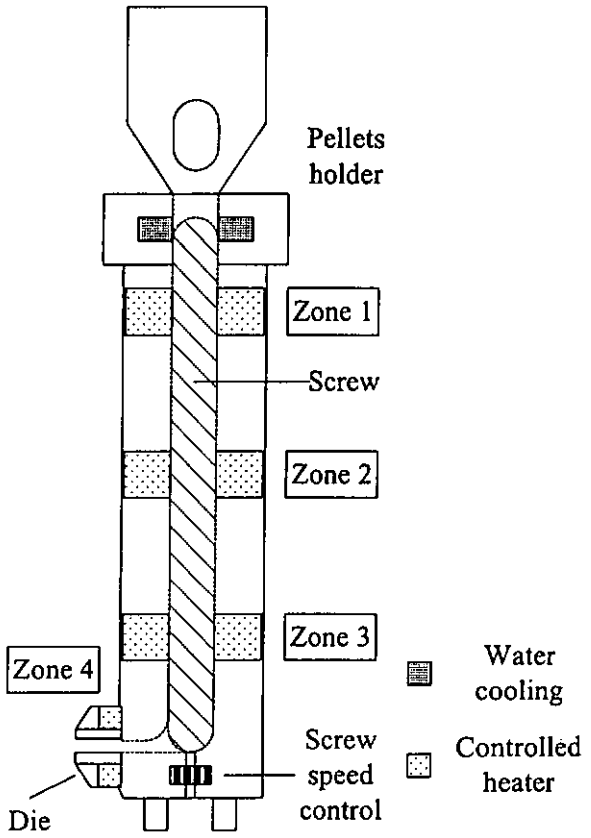

Figure 3.3 Schematic diagram of single screw extruder.

Table 3.1 The barrel temperature settings in the four zones and the screw speed of the extruder for all the composites.

PZT volume fraction (%)	2	5	13	18	26	30
1st zone temperature (°C)	147	145	144	135	134	141
2nd zone temperature (°C)	167	154	147	131	131	135
3rd zone temperature (°C)	174	156	151	135	129	126
4th zone temperature (°C)	168	143	141	132	127	123
Screw speed (rpm)	7.7	7.7	7.7	5	5	4

Thin film samples of thickness from 10 μm to 250 μm were prepared by the hot-pressing method. The PU or PZT/PU composite pellets and the spacers were placed in between two parallel stainless steel plates wrapped in aluminum foil. The stack was put in the hot press machine (Carver 3856) (Figure 3.4) and heated at 160°C for 10 minutes. Then a moderate pressure was applied and kept for 15 minutes. After that, the stack was cooled naturally under the applied force in the machine. A sample preparation flow chart for the PU and PZT/PU composite films is given in Figure 3.5. After measuring the density of the films, a gold electrode of suitable area (dependent on the measurement required) was coated on the both sides by sputtering. In some measurements such as electrostriction, compliant electrodes were used.

The thickness to width or length ratios of the film samples are smaller than 1/10.

With such dimensions, the films can be regarded as parallel plate capacitors and the fringe effect can be neglected.

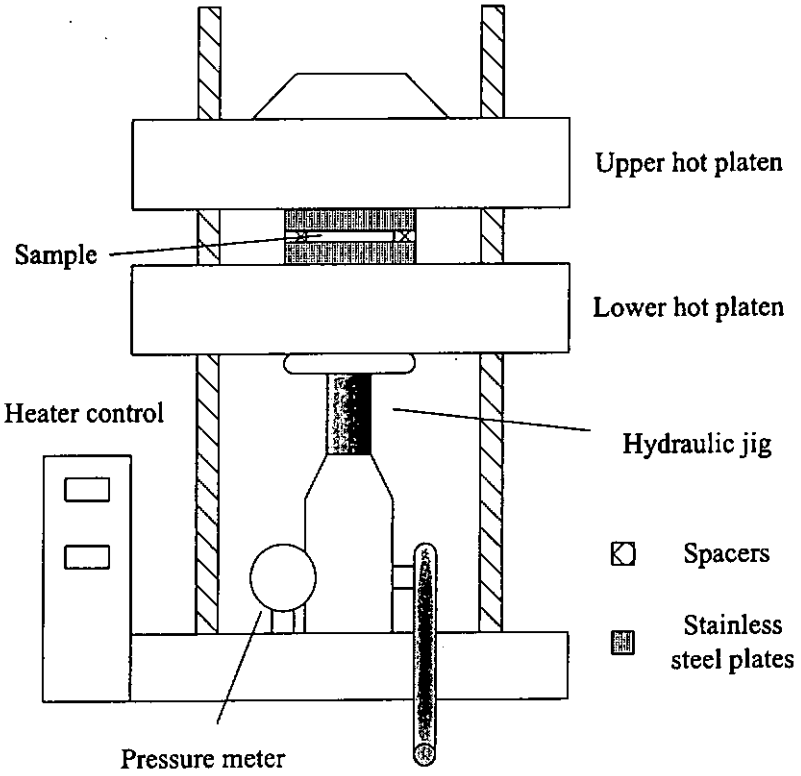

Figure 3.4 Schematic diagram of hot pressing machine.

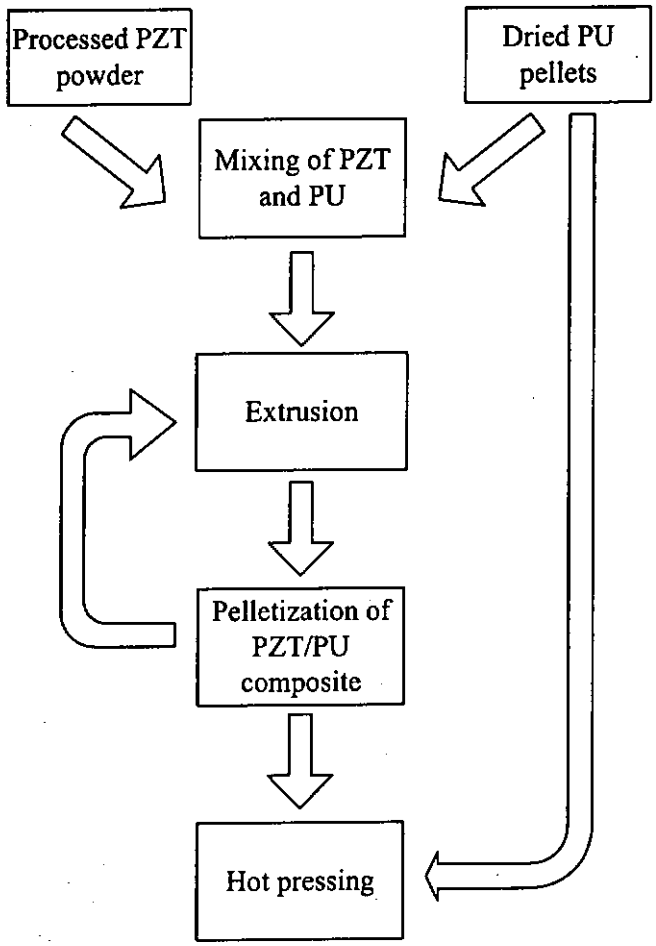

Figure 3.5 Preparation of PU and PZT/PU composite films.

3.2 Sample Characterization

3.2.1 Determination of PZT Volume Fraction

After fabrication, the actual PZT volume fraction of the composites can be found by using the following equation:

$$\rho = \phi_c \cdot \rho_c + (1-\phi_c) \cdot \rho_p \tag{3.1}$$

where ρ, ρ_c, and ρ_p are the densities of the composite, PZT and PU respectively and ϕ_c is the PZT volume fraction. The densities of PU and the composites were measured based on the Archimedes principle as follows:

$$\rho = \frac{m_a}{m_a - m_w} \tag{3.2}$$

where ρ, m_a are m_w are the sample density, sample mass in air and sample mass in water respectively. The measurement setup is shown in Figure 3.6. In addition, the density of the PZT powder was measured by using a 10ml density bottle (Technico BS733). The measurement steps and the calculation are shown in Figure 3.7 and Equation 3.3 respectively.

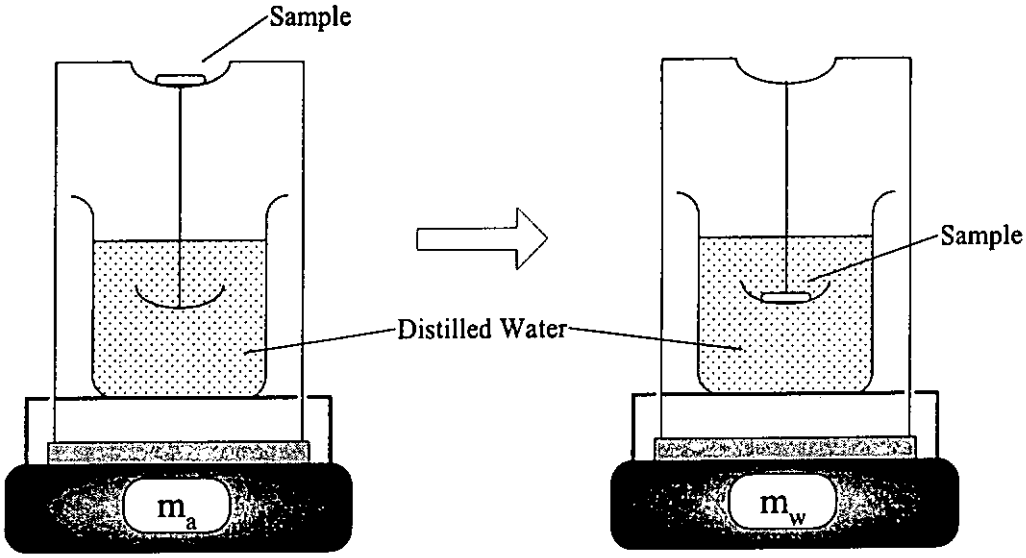

Figure 3.6 Solid film density measurement setup.

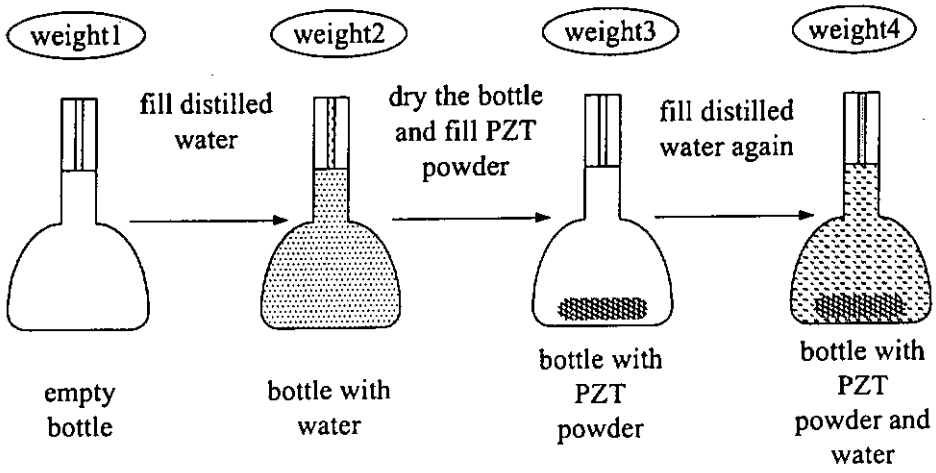

Figure 3.7 Density measurement of PZT powder.

$$\rho_{PZT} = \frac{weight3 - weight1}{(weight2 - weight1) - (weight4 - weight3)} \times \rho_W \quad (3.3)$$

where ρ_{PZT} and ρ_W are the densities of the PZT powder and distilled water at the measuring temperature (obtained from the standard table [Marsh, 1987]) respectively.

3.2.2 Microstructure Analysis

The cross-section morphology of the PZT/PU composite samples were studied by a field emission scanning electron microscope (SEM, Cambridge Stereoscan 440). The composite films were fractured in liquid nitrogen. Then a thin layer of gold was sputtered on the fracture surface. The images of the PZT/PU composites with PZT volume fraction from 2% to 30% are shown in Figures 3.8 (a)-(f) respectively. In the figures, it can be seen that the average size of PZT particles is about 3μm and there is no aggregation even in samples with high PZT content. On the other hand, some voids in the samples, which may have been formed in the preparation process, are observed.

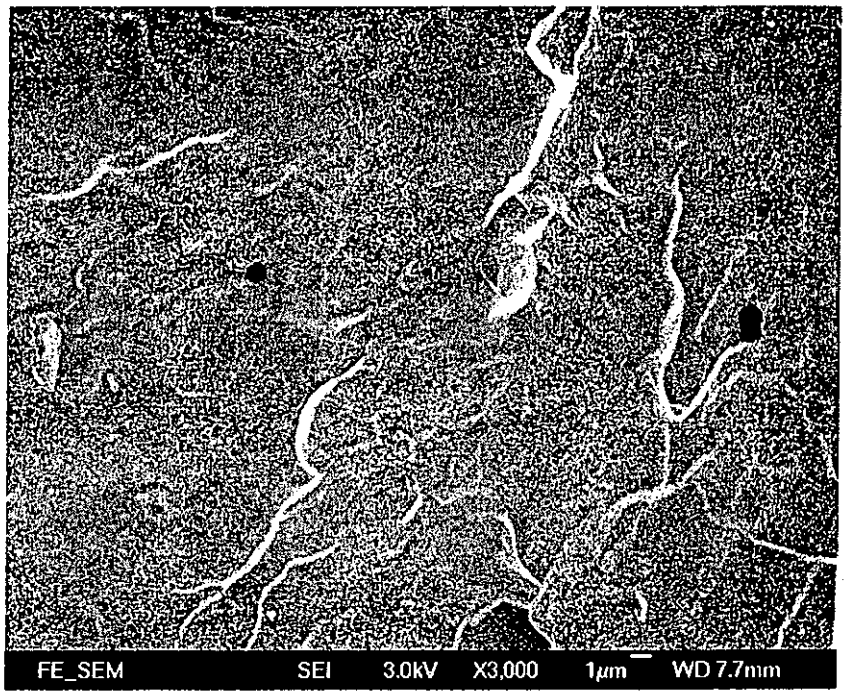

Figure 3.8 (a) SEM image of PZT(2%)/PU composite.

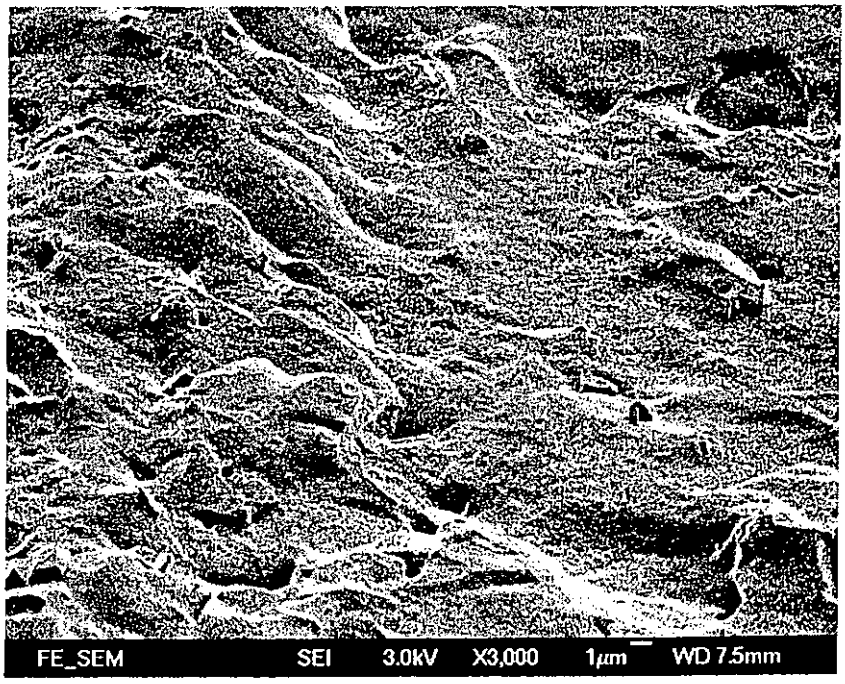

Figure 3.8 (b) SEM image of PZT(5%)/PU composite.

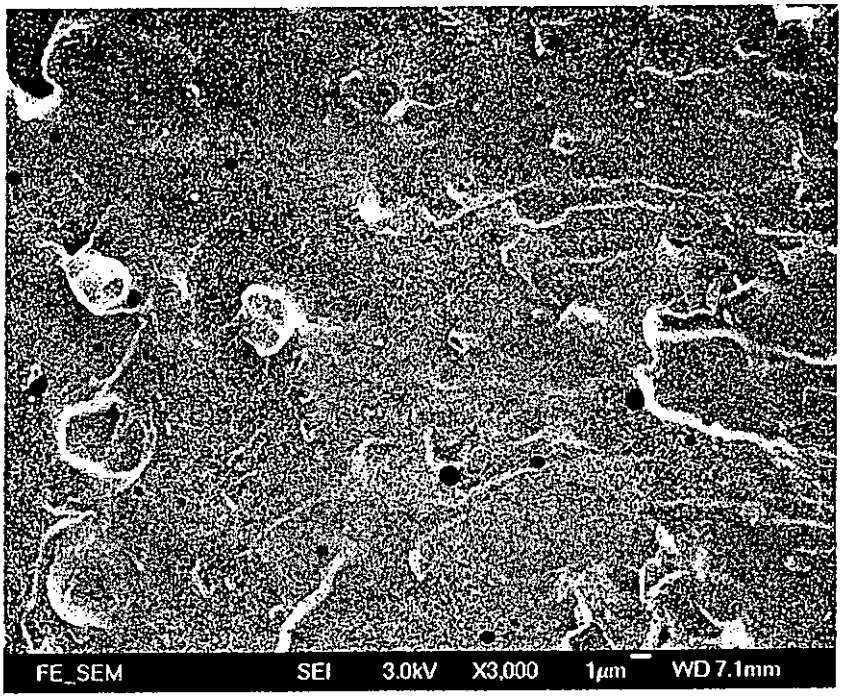

Figure 3.8 (c) SEM image of PZT(13%)/PU composite.

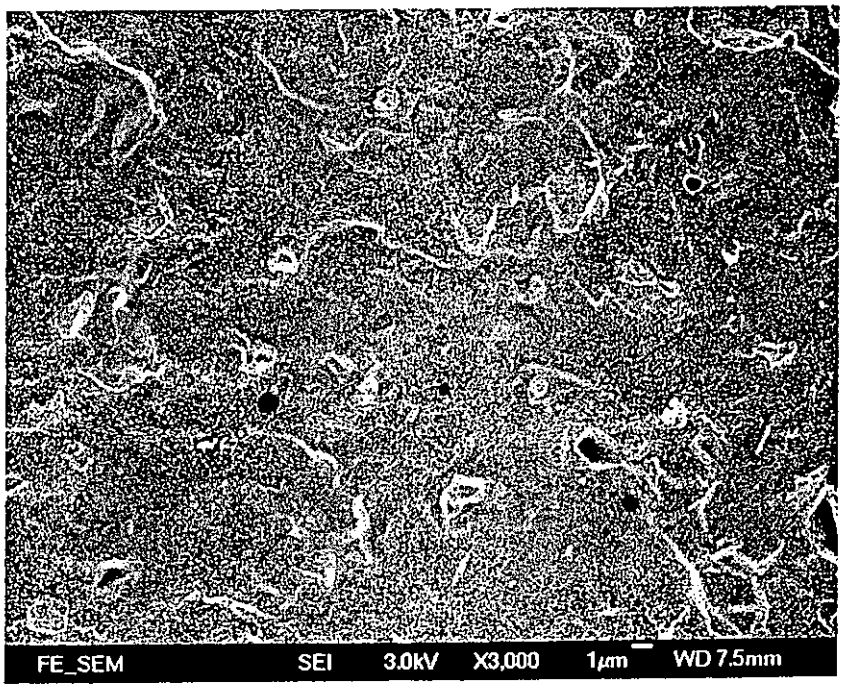

Figure 3.8 (d) SEM image of PZT(18%)/PU composite.

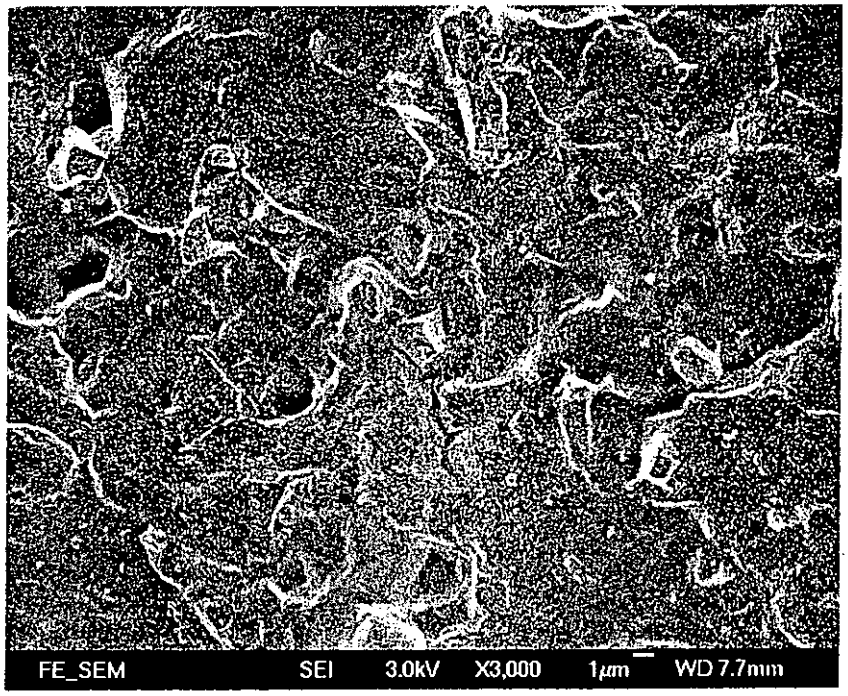

Figure 3.8 (e) SEM image of PZT(26%)/PU composite.

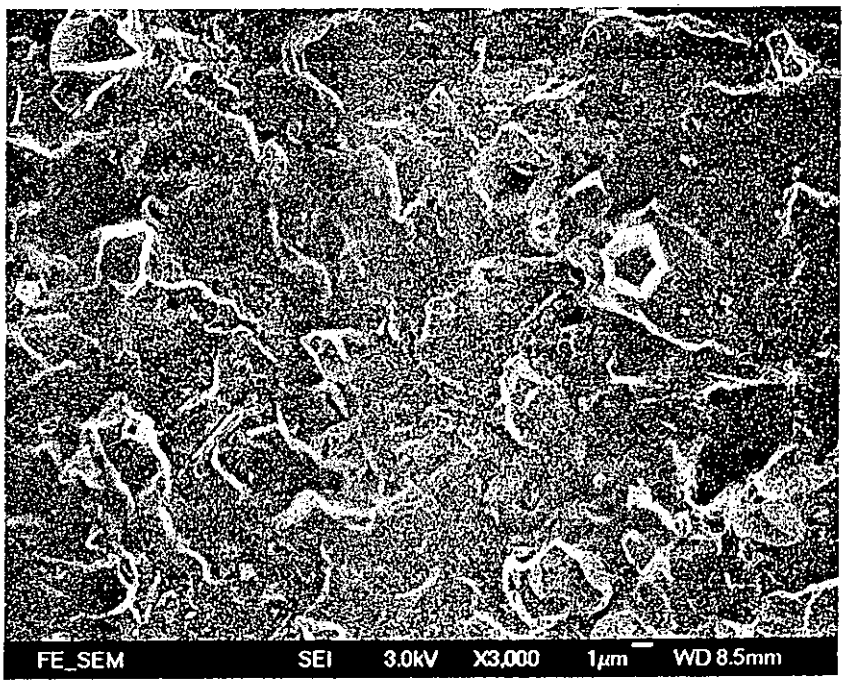

Figure 3.8 (f) SEM image of PZT(30%)/PU composite.

3.2.3 X-Ray Diffraction Analysis

The schematic diagram of X-ray diffraction of a crystal is shown in Figure 3.9. Consider two waves A and B, diffracted from atoms in adjacent planes separated by a distance *d*. They are only in phase if the path difference of wave A over B (x + y in the figure) is a multiple integral of the wavelength λ of the incident beam. The path difference x + y is equal to $2d\sin\theta$, where θ is the incident angle, so that constructive interference occurs when:

$$n\lambda = 2d\sin\theta \tag{3.4}$$

where n is an integer. This equation is also known as Bragg's law.

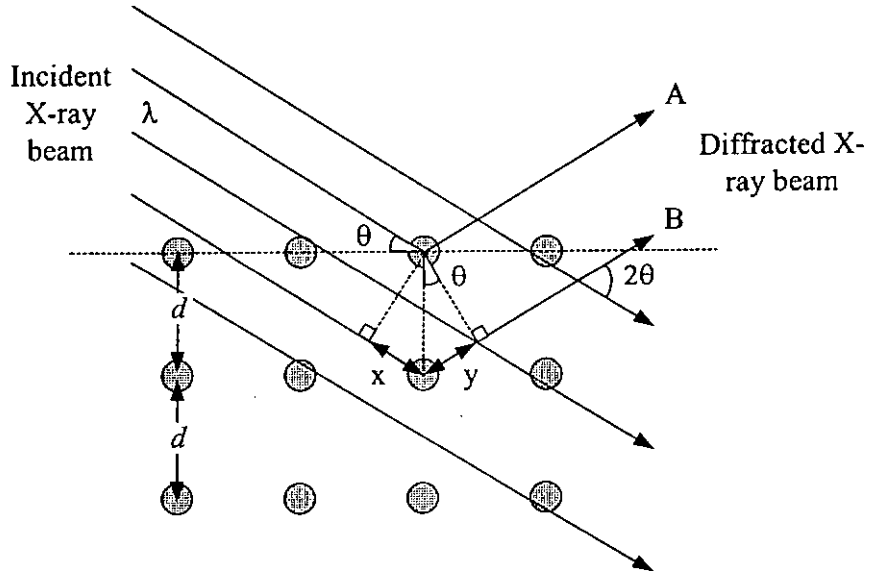

Figure 3.9 Schematic diagram of X-ray diffraction by a crystal.

In general, the observed X-ray diffraction from polymeric materials is due to the diffraction from both crystalline regions as well as the amorphous region. Sharp and well-defined diffraction peaks are attributed to the crystalline phase while the broad "halo" is the contribution from the amorphous phase. Polyurethane elastomers are multi-block copolymers in which hard urethane blocks are separated by flexible aliphatic polyether or polyester soft blocks [Nigar *et al.*, 1996]. PU has a broad "halo" X-ray spectrum which peaks at $2\theta \sim 20^{\circ}$, but it is not simply due to the diffraction from the amorphous phase of a typical polymer. The diffraction pattern results from the structural arrangement of hard segments of urethane blocks in the hard domains which serve as both crosslinks and filler particles in the continuous matrix of soft segments [Noshay et al., 1977].

In this study, the crystalline structure of PU, PZT and PZT/PU composites were studied by wide angle X-ray diffraction (XRD) (Bruker D8 Discovery). CuK_{α} radiation of $\lambda = 0.154$ nm was used. The XRD spectra were obtained by θ–2θ scan of which 2θ was scanned from 10° to 80° in 0.05° steps and 2s per step. The XRD profiles of pure PZT, 2, 13 and 30 vol% PZT/PU composites and neat PU are shown in Figure 3.10. Neat PU has a broad peak at about $2\theta = 20^{\circ}$ which is attributed to the phase segregation of the hard segments from the soft segment matrix in the PU. The sharp peaks at 22° and 32° of pure PZT are assigned to its (001) and (101) planes respectively. As the content of PZT increases, the XRD profiles are gradually dominated by the PZT diffraction and the intensity of the broad peak from PU almost disappears. For the 30 vol% PZT/PU composite sample, the broad peak from PU is very small compared with the peaks of

PZT. It implies that phase segregation in PU is suppressed in the presence of PZT particles.

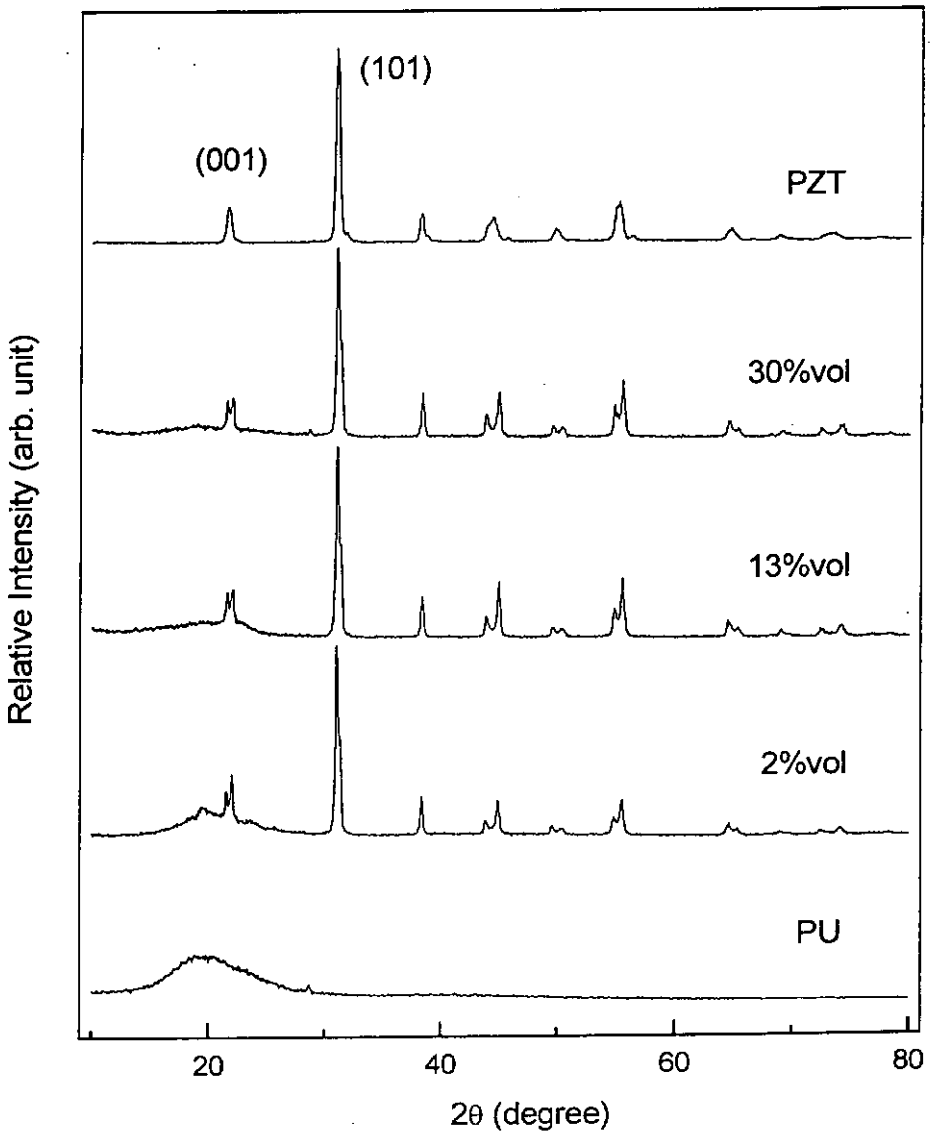

Figure 3.10 The XRD profiles of pure PZT, 2, 13 and 30 vol% PZT/PU composites and neat PU.

3.2.4 Infrared Absorption Analysis

Infrared spectroscopy is an important technique in studying polymeric materials. It is easy to identify the presence of certain functional groups in a molecule. Also, one can use the unique collection of absorption bands to confirm the identity of a pure compound or to detect the presence of specific impurities.

The infrared absorption spectra of pure PZT powder, 2, 13, 30 vol% PZT/PU composites and neat PU were obtained by a Fourier Transform Infrared Spectrometer (FTIR) (Magna-IR 760, Nicolet). For obtaining the IR absorption spectrum of PZT powder, the diffusion reflectance mode was used. In addition, the transmittance mode was used for determining the IR absorption of thin films (10 to 20 μm) of PZT/PU composites and PU. The mid-IR range from 400 to 4000cm^{-1} was chosen in all measurements.

Figure 3.11 shows the IR absorption spectra of pure PZT powder, 2, 13, 30 vol% PZT/PU composites and neat PU. PZT particles exhibit strong IR absorption in the mid-IR range. Therefore the IR absorption of PU is almost obscured by the PZT particles. For the 13 and 30 vol% PZT/PU sample, their IR spectra are almost featureless.

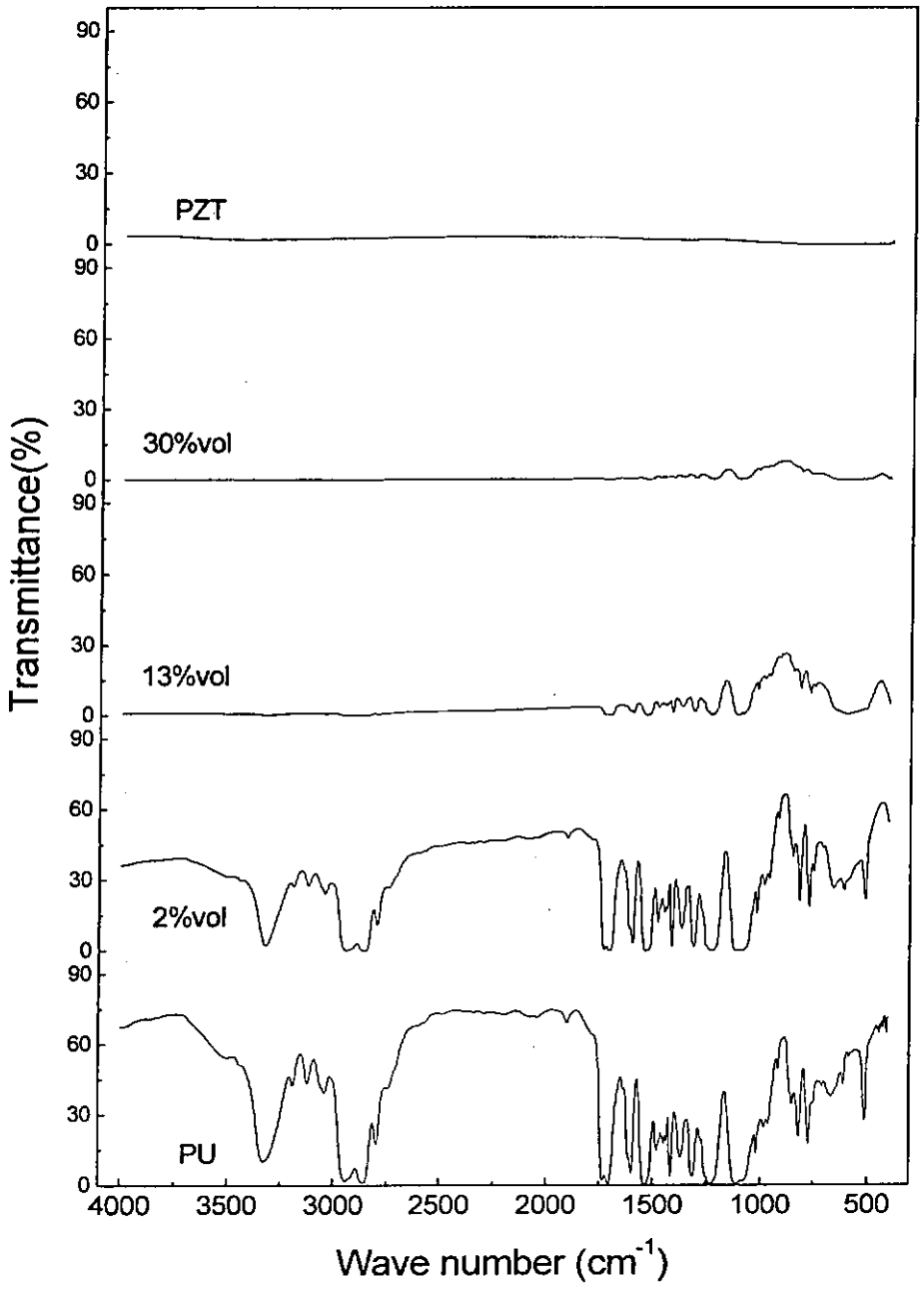

Figure 3.11 FTIR spectrum of pure PZT, 2, 13, 30 vol% PZT/PU composites and neat PU.

Chapter 4

Dielectric and Pyroelectric Properties of PZT/PU Composites

4.1 Dielectric Properties

4.1.1 Dielectric Measurement

In this study, the dielectric permittivity and loss of pure PZT, PU and PZT/PU composites were measured at the frequency of 1 kHz at room temperature. For ferroelectric materials, the dielectric permittivity and loss are important parameters for most of their applications [Xu, 1991]. The relative permittivity ε_r, also called the dielectric constant, of a material is the ratio of the amount of charge that can be stored on an electroded slab of the material subjected to a given voltage to the charge that would be stored by identical electrodes separated by a vacuum at the same voltage. The relative permittivity of the sample is calculated by using the following equation:

$$\varepsilon_r = \frac{CL}{\varepsilon_o A} \tag{4.1}$$

where C is the capacitance of the sample, L is the distance between electrodes, ε_o is the dielectric permittivity of vacuum which is equal to 8.85×10^{-12} F/m and A is the area of

the electrode. The dielectric permittivity of a material usually depends on frequency ω when an ac voltage is applied. In general, the dielectric permittivity ε can be written in complex notation:

$$\varepsilon = \varepsilon' - j\varepsilon'' \tag{4.2}$$

where ε' and ε'' are the real part and imaginary part of the dielectric permittivity respectively. The imaginary part also represents the dielectric loss and the loss tangent tan δ is defined as:

$$\tan\delta = \frac{\varepsilon''}{\varepsilon'} \tag{4.3}$$

By using Equation 4.1, the relative permittivity of the samples can be determined if the capacitance and the dimensions of the capacitor are known.

The capacitance and the loss tangent of the dried film samples were measured by using an HP 4194A impedance/gain-phase analyzer. The measurement frequency was kept at 1 kHz. The average relative permittivity and the dielectric loss of neat PU and PZT/PU composites with PZT volume fraction ϕ from 0.02 to 0.3 are shown in Figures 4.1 (a) and 4.1 (b) respectively. We can see that the relative permittivity and the dielectric loss of the PZT/PU composites increase with the volume fraction of PZT. The Bruggeman model is used to fit the relative permittivity and the dielectric loss.

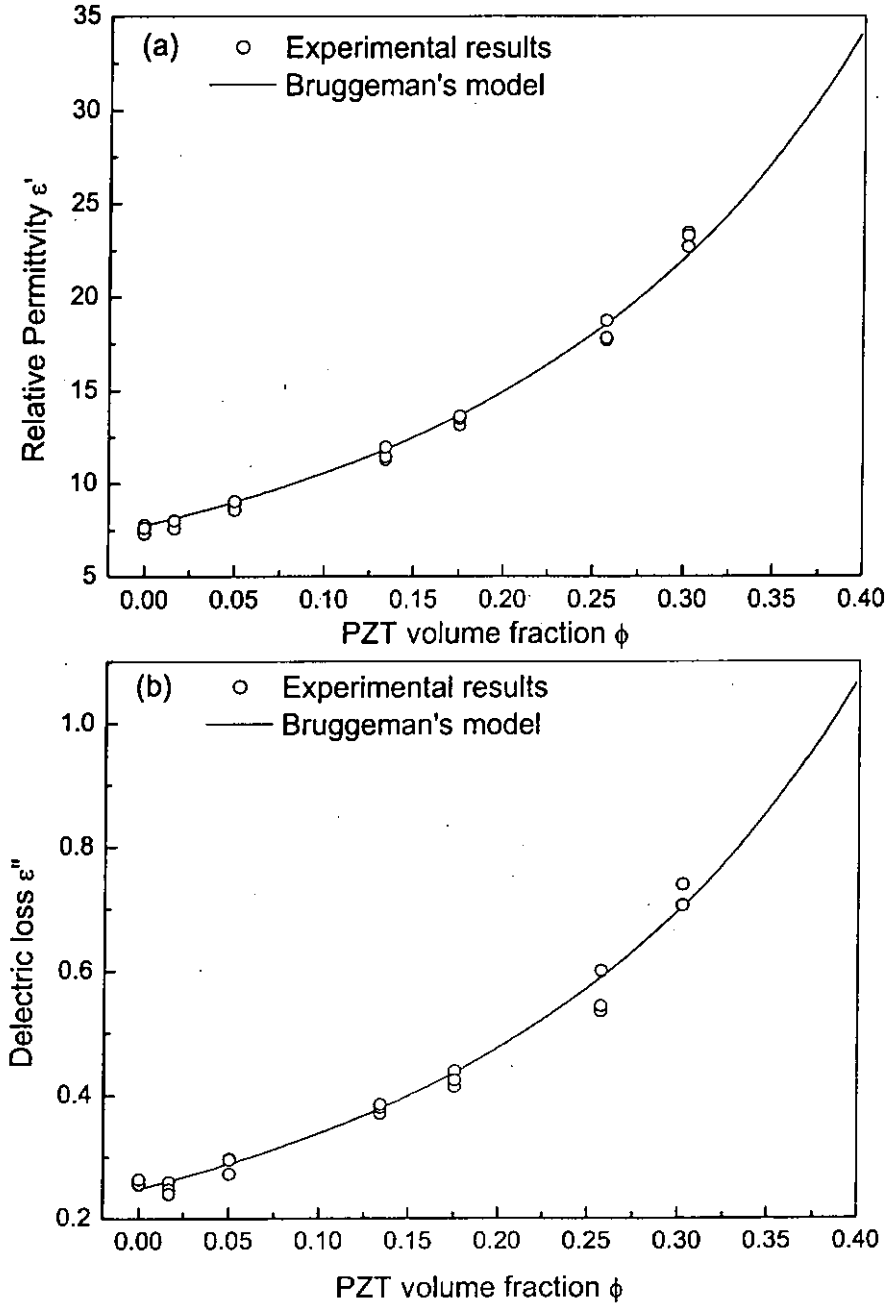

Figure 4.1 (a) Relative permittivity and **(b)** dielectric loss of PZT/PU composites as a function of ϕ at room temperature and frequency of 1 kHz.

4.1.2 Bruggeman Model for the Permittivity of 0-3 Composite

The Bruggeman model was used to describe the dielectric permittivity of the 0-3 composite with particles embedded in a polymer matrix. The asymmetric Bruggeman's equation for the dielectric permittivity ε_c of a composite is given as:

$$\frac{\varepsilon_i - \varepsilon_c}{\varepsilon_i - \varepsilon_m} = (1-\phi)(\frac{\varepsilon_c}{\varepsilon_m})^{\frac{1}{3}} \tag{4.4}$$

where ε_i, ε_c and ε_m are the dielectric permittivity of the inclusion, composite and matrix respectively and ϕ is the volume fraction of the inclusions in the composite. If the dissipation factors (loss tangent) of the constituent materials are small (in this study, the dissipation factors of PU and PZT are 0.03 and 1.5×10^{-4} respectively), by substituting the complex form of dielectric permittivity into Equation 4.4 and taking the first order approximation, it can then be separated into two equations as shown below:

$$\frac{\varepsilon_i{}' - \varepsilon_c{}'}{\varepsilon_i{}' - \varepsilon_m{}'} = (1-\phi)(\frac{\varepsilon_c{}'}{\varepsilon_m{}'})^{\frac{1}{3}} \tag{4.5}$$

$$\varepsilon_c{}'' = \frac{(\varepsilon_i{}'-\varepsilon_c{}')(\varepsilon_i{}'+2\varepsilon_m{}')\varepsilon_c{}'\varepsilon_m{}''}{(\varepsilon_i{}'-\varepsilon_m{}')(\varepsilon_i{}'+2\varepsilon_c{}')\varepsilon_m{}'} + \frac{3(\varepsilon_c{}'-\varepsilon_m{}')\varepsilon_c{}'\varepsilon_i{}''}{(\varepsilon_i{}'-\varepsilon_m{}')(\varepsilon_i{}'+2\varepsilon_c{}')} \tag{4.6}$$

where ε' and ε'' are the real and imaginary part of the dielectric permittivity and the subscripts *i*, *c* and *m* represent the inclusion (PZT), composite and matrix (PU).

Therefore, both the real and imaginary parts of the composite permittivity can be calculated from these two equations.

From the measured relative permittivity and dielectric loss values of PU, $\varepsilon_r' = 7.7$ and $\varepsilon_r'' = 0.25$, and those of PZT, $\varepsilon_r' = 1800$, $\varepsilon_r'' = 0.279$ (from MatWeb.com, The Online Material Database), the real and imaginary of the relative permittivity of the composites are obtained and they are shown in Figures 4.1 (a) and (b) respectively. By comparing the calculated Bruggeman curve with the experimental results, a reasonably good agreement is found for ϕ up to 0.3.

4.2 Pyroelectric Properties

4.2.1 Pyroelectric Measurement

Pyroelectricity arises from the change in polarization of a dielectric material due to a change in temperature. A pyroelectric material presents a spontaneous polarization P_s in the absence of an electric field. The pyroelectric coefficient p is determined from [Sakamoto, 1998]:

$$p = -\frac{\partial P_s}{\partial T} \tag{4.7}$$

where T is the temperature. From Equation 2.13, P_s is equal to the electric displacement D under field-free and stress-free condition. When expressed in terms of charge Q on the electrodes coated on a thin slab of a pyroelectric material in the parallel-plate capacitor geometry, then $P_s = \frac{Q}{A}$ and Equation 4.7 gives,

$$p = -\frac{1}{A}\frac{\partial Q}{\partial T} = -\frac{1}{A}\frac{\partial t}{\partial T}\frac{\partial Q}{\partial t} = -\frac{1}{A}\frac{I_p}{\partial T/\partial t} \tag{4.8}$$

where Q is the surface charge, A is the electrode area, t is time and $I_p = \partial Q/\partial t$ is the short-circuit pyroelectric current.

The pyroelectric coefficient can be determined by dc or ac method. In the dc method, the thermally stimulated discharge current (TSDC) of a poled sample is measured in a temperature range under a constant heating rate for a few runs until a reproducible current is measured [Garn et al., 1982]. The measured current is referred to pyroelectric current I_p. The pyroelectric coefficient can be obtained by substituting the I_p and the heating rate $\partial T/\partial t$ in Equation 4.7.

Another way to measure the pyroelectric coefficient is the ac method. The sample is maintained at temperature T_o and a small sinusoidal temperature variation $T_\Delta sin(\omega t)$ of angular frequency ω and amplitude T_Δ is applied uniformly to the sample. The rate of change of temperature is equal to:

$$\frac{dT}{dt} = \omega T_\Delta \cos(\omega t) \tag{4.9}$$

The induced pyroelectric current density $J(t)$ is equal to:

$$J(t) = \frac{\partial P_s}{\partial t} = \frac{\partial T}{\partial t}\frac{\partial P_s}{\partial T} \tag{4.10}$$

Substituting Equations 4.7 and 4.9 into Equation 4.10, the pyroelectric short-circuit current density can be written as

$$J(t) = -pT_\Delta \omega \cos(\omega t) \tag{4.11}$$

As a result, the pyroelectric coefficient p can be obtained by measuring the component of the observed current density $J(t)$ which is 90° out of phase to the applied temperature variation.

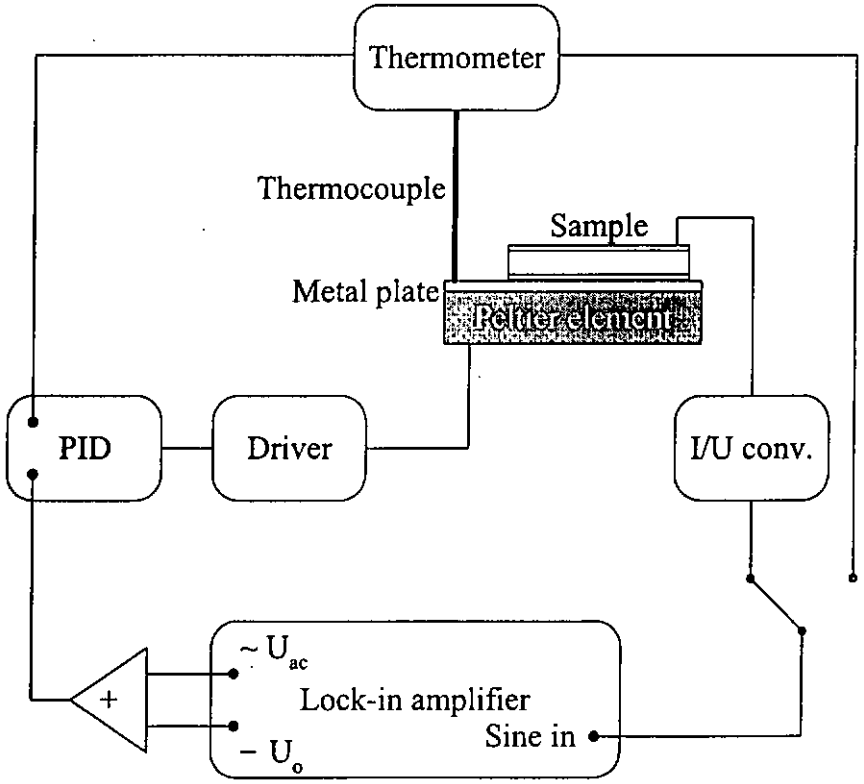

Figure 4.2 Schematic diagram of the dynamic pyroelectric measurement setup.

In this study, an ac method was used to measure the pyroelectric coefficient. The pure PU and PZT/PU composite films were poled under an applied field of 20 MV/m at room temperature for one hour. For preventing air break down, all samples were immersed in silicone oil during the poling process. For removing the extra charges

trapped in the samples, the poled samples were put into an oven and kept at 60°C for at least 10 hours under short circuit condition.

Figure 4.2 shows the block diagram for the ac pyroelectric measurement. A sinusoidal voltage U_{ac} at a frequency f of 5 mHz from the lock-in amplifier was superimposed on the dc voltage U_o from a programmable voltage source to form the reference signal. Then the reference signal was sent to a power regulator equipped with a proportional-integral-differential (PID) temperature controller. The temperature controller compared this signal with the true temperature signal, which was measured by a thermocouple, to control a Peltier element to generate the sinusoidally modulated temperature $T(t) = T_o + T_\Delta sin(2\pi ft)$ with amplitude $T_\Delta = 1$ K at temperature $T_o = 298$ K. The sample film was in contact with the Peltier element. The pyroelectric current was measured by an electrometer and the 90° out of phase component of the current with respect to the temperature modulation (i.e. in phase with the temporal derivative $dT(t)/dt$) was measured by the lock-in amplifier. The pyroelectric coefficient p can be obtained from Equation 4.11. On the other hand, the modulation frequency should be low enough so that a uniform temperature across the thickness of the sample could be established. The upper limit of the measurement frequency [Dias, 1996] can be obtained from the equation

$$f << \frac{D}{2\pi L^2} \tag{4.12}$$

where D is the thermal diffusivity of the sample and L is the sample thickness, otherwise the measurement will be affected by the current due to the temperature gradient formed across the thickness of the sample.

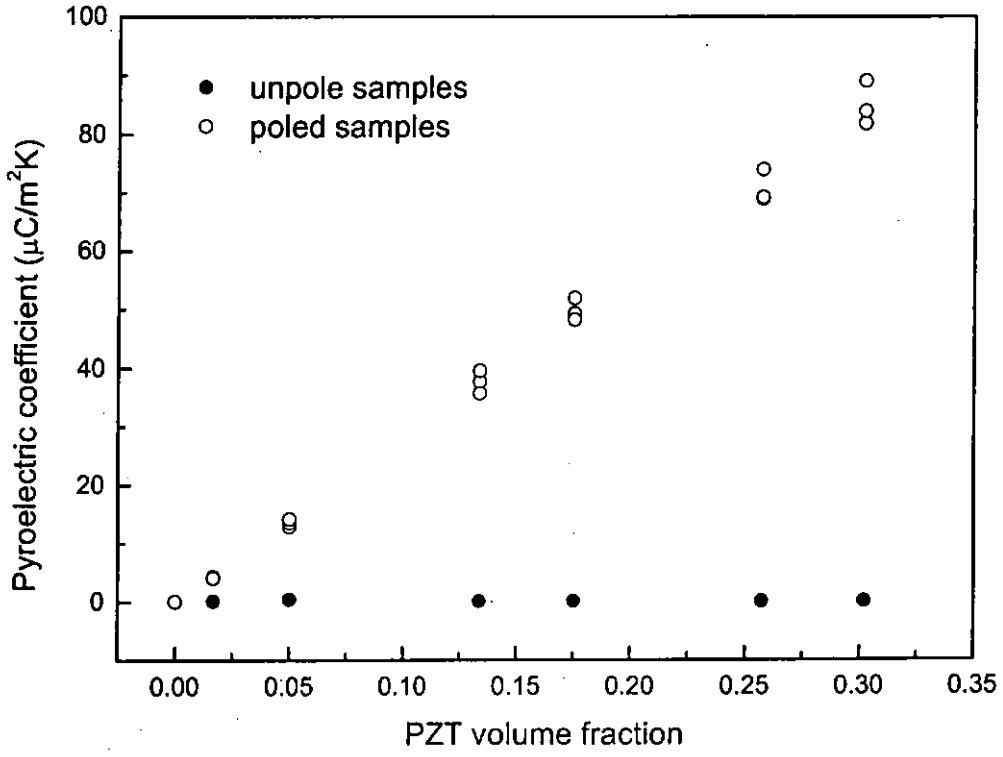

Figure 4.3 Pyroelectric coefficient of pure PU and PZT/PU composites at 25°C as a function of volume fraction of PZT.

The pyroelectric coefficients of the pure PU and PZT/PU composites with PZT volume fraction of 2, 5, 13, 18, 26 and 30% are shown in Figure 4.3. It can be seen that the higher PZT content in the composites the higher the pyroelectric coefficient is obtained. On the other hand, the pyroelectric coefficient of pure PZT was found to be

330 μC/m^{2}K. The relation of the pyroelectric coefficient and the PZT volume fraction is almost linear. This relation can be described by a model which will be presented in the next section.

4.2.2 Modeling of the Pyroelectric Coefficient of PZT/PU 0-3 Composites

There are some models predicting the effective pyroelectric coefficients p of ferroelectric 0-3 composites with a non-pyroelectric matrix [Wada et al., 1981; Das-Gupta et al., 1991]. The pyroelectric coefficient is commonly described by the following equation:

$$p = \phi B_E p_i \tag{4.13}$$

where

$$B_E = \frac{3\varepsilon_m}{(2+\phi)\varepsilon_m + (1-\phi)\varepsilon_i} \tag{4.14}$$

ϕ, p_i and ε_i are the volume fraction, the pyroelectric coefficient and the dielectric permittivity of the inclusion material respectively and ε_m is the dielectric permittivity of the matrix. The above expression [Furukawa et al, 1976] for B_E is derived from the Maxwell-Wagner model, which assumes the inclusions are spherical and ϕ is small.

Putting $\varepsilon_m = 7.7 \times \varepsilon_0$, $\varepsilon_i = 1800 \times \varepsilon_0$ and $p_i = 330$ μC/m^{2}K into Equations 4.13 and 4.14, a plot of pyroelectric coefficient versus ϕ can be obtained and is shown as the dotted line in Figure 4.4. It is obvious that the calculated values are far too small

compared with the experimental results. A detailed study of Equation 4.13 shows that it is derived for composites in which the electric conductivities of inclusion and matrix are both small enough to be neglected in the formulation. However, this may not be true for our case. In this regard, a model for composites with "high" conductivity is necessary. It will be given in the following paragraph.

Consider a composite with a dilute dispersion of spherical inclusion particles in a continuous matrix, the average electric field E and the displacement D in the composite can be obtained as [Furukawa, 1976; Wong, 2001(c)]:

$$E = \phi E_i + (1-\phi)E_m \tag{4.15}$$

$$D = \phi D_i + (1-\phi)D_m \tag{4.16}$$

where ϕ is the inclusion volume fraction, the subscripts i and m denote inclusion and matrix respectively. The relations of displacement and switchable polarization P of the inclusion and matrix [Furukawa, 1986] are:

$$D_i = P_i + \varepsilon_i E_i \tag{4.17}$$

$$D_m = P_m + \varepsilon_m E_m \tag{4.18}$$

Putting Equations 4.17, 4.18 and $P_m = 0$ (for a non-pyroelectric matrix like PU) into Equation 4.16, the electric displacement can be written as:

$$D = \phi(\varepsilon_i E_i + P_i) + (1-\phi)\varepsilon_m E_m \tag{4.19}$$

and

$$\frac{\partial D}{\partial t} = \phi(\varepsilon_i \frac{\partial E_i}{\partial t} + \frac{\partial P_i}{\partial t}) + (1-\phi)\varepsilon_m \frac{\partial E_m}{\partial t} \tag{4.20}$$

For a dilute dispersion of spherical inclusions of permittivity ε_i and electrical conductivity σ_i in a matrix of permittivity ε_m and electrical conductivity σ_m with a uniform electric field applied along the thickness direction, the following equations can be obtained [Wong, 2002]:

$$\frac{\partial E_i}{\partial t} + \frac{E_i}{\tau} = \frac{3[\sigma_m E + \varepsilon_m \frac{\partial E}{\partial t}] - (1-\phi)\frac{\partial P_i}{\partial t}}{\phi 3\varepsilon_m + (1-\phi)(\varepsilon_i + 2\varepsilon_m)} \tag{4.21}$$

where

$$\tau = \frac{\phi 3\varepsilon_m + (1-\phi)(\varepsilon_i + 2\varepsilon_m)}{\phi 3\sigma_m + (1-\phi)(\sigma_i + 2\sigma_m)} \tag{4.22}$$

For pyroelectric current measurement, the sample is connected in short circuit condition. As a result, the electric field $E = 0$. Equation 4.21 can be simplified to

$$\frac{\partial E_i}{\partial t} + \frac{E_i}{\tau} + \frac{(1-\phi)\frac{\partial P_i}{\partial t}}{\phi 3\varepsilon_m + (1-\phi)(\varepsilon_i + 2\varepsilon_m)} = 0 \tag{4.23}$$

and Equation 4.15 becomes,

$$\phi E_i = -(1-\phi)E_m \tag{4.24}$$

Substituting E_i into Equation 4.23,

$$\frac{\partial E_m}{\partial t} + \frac{E_m}{\tau} - \frac{\phi \frac{\partial P_i}{\partial t}}{\phi 3\varepsilon_m + (1-\phi)(\varepsilon_i + 2\varepsilon_m)} = 0 \tag{4.25}$$

From Equations 4.10 and 4.11, we obtain $\frac{\partial P_i}{\partial t} = -p_i \omega T_\Delta \cos \omega t$ and for a sinusoidal variation in temperature, E_i and E_m must also be sinusoidal at steady state, so that the first order differential equations 4.23 and 4.25 can be solved:

$$E_i = \frac{(1-\phi) p_i T_\Delta}{\phi 3\varepsilon_m + (1-\phi)(\varepsilon_i + 2\varepsilon_m)} \frac{\omega\tau}{1+\omega^2\tau^2} (\cos \omega t + \omega\tau \sin \omega t) \tag{4.26}$$

$$E_m = -\frac{\phi p_i T_\Delta}{\phi 3\varepsilon_m + (1-\phi)(\varepsilon_i + 2\varepsilon_m)} \frac{\omega\tau}{1+\omega^2\tau^2} (\cos \omega t + \omega\tau \sin \omega t) \tag{4.27}$$

On the other hand, the current density J is the sum of the electric conduction current density j and the displacement current $\frac{\partial D}{\partial t}$. The conduction current can be written as

$$j = \sigma E = (1-\phi)\sigma_m E_m + \phi \sigma_i E_i \tag{4.28}$$

therefore,

$$J = (1-\phi)\sigma_m E_m + \phi \sigma_i E_i + \frac{\partial D}{\partial t} \tag{4.29}$$

Substituting Equations 4.26 and 4.27 into Equation 4.29 and collecting the terms in *cos(ωt)*, we obtain

$$J^{\cos} = -\omega T_{\Delta} \cos(\omega t) \cdot \phi p_i \left[1 - \frac{(1-\phi)}{3\phi\varepsilon_m + (1-\phi)(\varepsilon_i + 2\varepsilon_m)} F \right] \tag{4.30}$$

where

$$F = \frac{\omega^2\tau^2}{1+\omega^2\tau^2}(\varepsilon_i - \varepsilon_m) + \frac{\tau}{1+\omega\tau}(\sigma_i - \sigma_m) \tag{4.31}$$

J^{cos} is the cosine component of the current density $J(t)$ as shown in Equation 4.11. As a result, the pyroelectric coefficient can be obtained:

$$p = \phi p_i \left[1 - \frac{(1-\phi)}{3\phi\varepsilon_m + (1-\phi)(\varepsilon_i + 2\varepsilon_m)} F \right] \tag{4.32}$$

If the conductivities of the inclusions and matrix are small enough, for example in the order of $10^{-12}\,\Omega^{-1}m^{-1}$, then τ becomes large and F approximately equals to $(\varepsilon_i - \varepsilon_m)$, so that Equation 4.30 becomes Equation 4.13.

In this study, the electrical conductivity of the PU was obtained by measuring its resistance using the Keithley 6517 electrometer. The electric field generated by the voltage source in the electrometer was about 0.04 MV/m which was comparable to the electric field generated in the pyroelectric coefficient measurement. σ_m was found to be $2.3\times10^{-10}\ \Omega^{-1}m^{-1}$. Substituting σ_m, σ_i ($5\times10^{-12}\ \Omega^{-1}m^{-1}$ [Chan, 1995]), the electric

conductivity of PZT, and other parameters into Equation 4.32, the pyroelectric coefficient of PZT/PU composites as a function of PZT volume fraction can be obtained. The results are shown in solid line in Figure 4.4. A very good agreement is evident.

It can be concluded that for a composite with ferroelectric inclusions in a non-pyroelectric matrix, its pyroelectric coefficient at low inclusion volume fraction can be described by Equation 4.32.

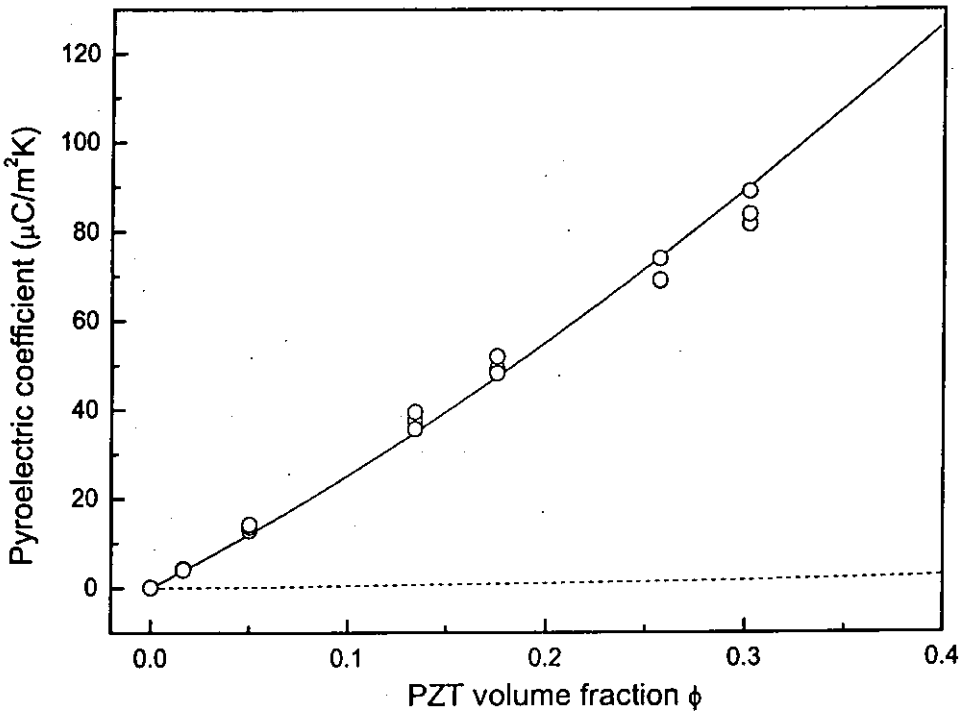

Figure 4.4 Pyroelectric coefficients of PZT/PU composites versus ceramic volume fraction. The open circles refer to the experimental results. The solid and dotted lines refer to theoretical calculations that consider conductivities and neglect conductivities respectively.

Chapter 5

PZT/PU Composites for Pyroelectric Sensor Application

5.1 Thermal Properties of PZT/PU Composites

Thermal properties such as thermal diffusivity, thermal conductivity, and specific heat are factors affecting the thermal response of a material. They are important especially for materials for thermal sensor application.

In general, for heat transfer between two plane surfaces of a film material by conduction, the rate of conduction to the first order approximation is given by:

$$\frac{H}{t} = \frac{\kappa A \Delta T}{L} \tag{5.1}$$

where H is the heat transferred in time t, κ is a thermal conductivity of the material, A is the cross-sectional area, ΔT is the temperature difference between the surfaces and L is the film thickness. Equation 5.1 can be rearranged as:

$$\kappa = (\frac{1}{A}\frac{H}{t})/(\frac{\Delta T}{L}) = \frac{\Phi_Q}{\Gamma} \tag{5.2}$$

which is the common definition of thermal conductivity of a material. It expresses the heat flux Φ_Q (W/m^2) that flows through the material in which a temperature gradient Γ

(K/m) exists. It should be noted that Equation 5.1 is valid only in a static condition, i.e. the temperature gradient is assumed to be constant. If the temperature gradient changes with time, a more complicated equation is required to describe the heat transfer problem. In order to measure the thermal conductivity, it would ideally require a steady thermal condition. This is not easy because it usually requires a carefully planned laboratory experiment and a long time to get the sample in thermal equilibrium. This explains why it is difficult to measure thermal conductivity by a static method. On the other hand, in heat transfer analysis, thermal diffusivity is a useful parameter which measures the heat diffusion coefficient of a material. It is related to the thermal conductivity and the specific heat of the material:

$$D_{th} = \frac{\kappa}{\rho \cdot c} \tag{5.3}$$

where D_{th} (m^2/s) is the thermal diffusivity, κ is the thermal conductivity, ρ and c are density and specific heat respectively. A material with a high D_{th} can rapidly reach temperature equilibrium if any part of the material experiences a temperature disturbance.

Generally speaking, there are a number of methods to measure thermal diffusivity, each suited to a limited class of materials, depending on their thermal properties and the applicable temperature range.

In this study, laser flash radiometry, a non-steady-state technique, was applied to measure the thermal diffusivity of samples. The details of the measurement will be

introduced in 5.1.2.

5.1.1 Specific Heats of PU, PZT/PU Composites and PZT

The specific heats of pure PU, PZT and PZT/PU composites were measured by using a standard differential scanning calorimeter (DSC, Perkin-Elmer DSC-7). The sample mass was about 10mg and the heating rate was 10°C per minute from 0°C to 50°C in a nitrogen atmosphere. The specific heats at room temperature (~23°C) were determined and they were plotted as a function of PZT volume function which is shown in Figure 5.1. From the figure, it is evident that the specific heats of the PZT/PU composites decrease with the increase in PZT content. As the specific heats of pure PU and PZT were determined to be 1.83×10^3 and 0.38×10^3 $JK^{-1}kg^{-1}$ respectively, the specific heats of the composites with different PZT contents can be approximately calculated by using the rule of mixtures:

$$c \approx \phi^m c_i + (1-\phi^m)c_m \tag{5.4}$$

with

$$\phi^m = \frac{\phi\rho_i}{\phi\rho_i + (1-\phi)\rho_m} \tag{5.5}$$

where c, c_i and c_m are the specific heats of the PZT/PU composite, PZT and PU respectively, ϕ^m and ϕ are the mass fraction and volume fraction of PZT respectively.

As a result the specific heats of PZT/PU composites can be calculated. Results are shown in Figure 5.1 as the solid line. It is found that the experimental values are very

close to the calculated values.

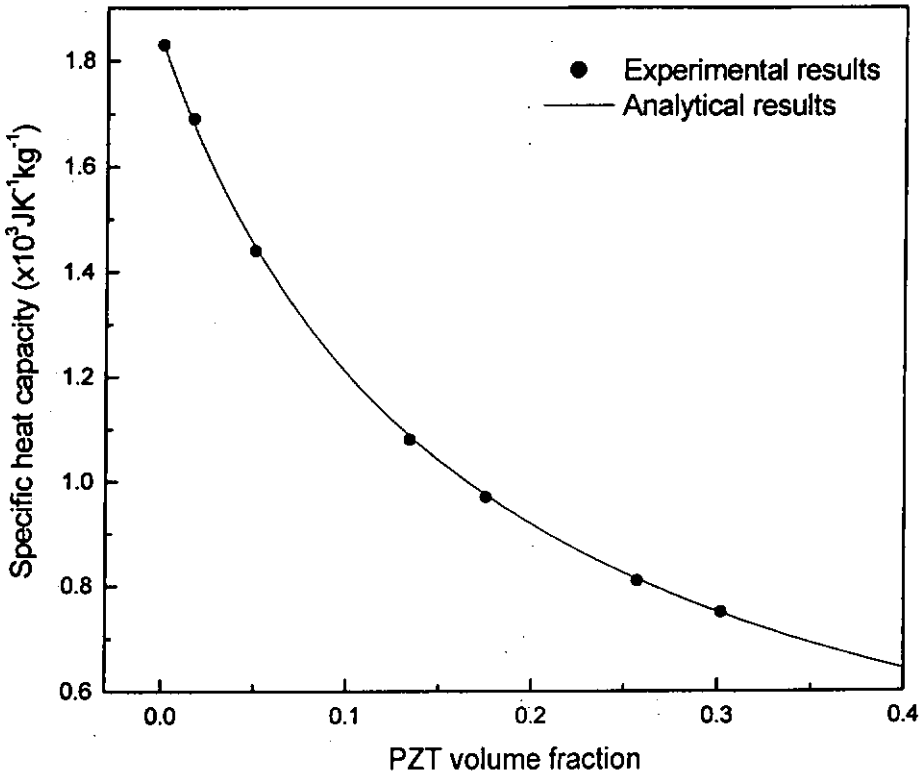

Figure 5.1 Specific heats of PU and PU/PZT composites at room temperature as a function of PZT volume fraction.

On the other hand, the volumetric specific heat C_v is defined as the product of specific heat and the density. The volumetric specific heat of PU, PZT/PU composites and PZT were determined and the analytical values were also calculated by using the following equation:

$$C_v = \phi \rho_i c_i + (1-\phi)\rho_m c_m \tag{5.6}$$

Both the experimental and analytical values of C_v of PZT/PU composites are shown in Figure 5.2.

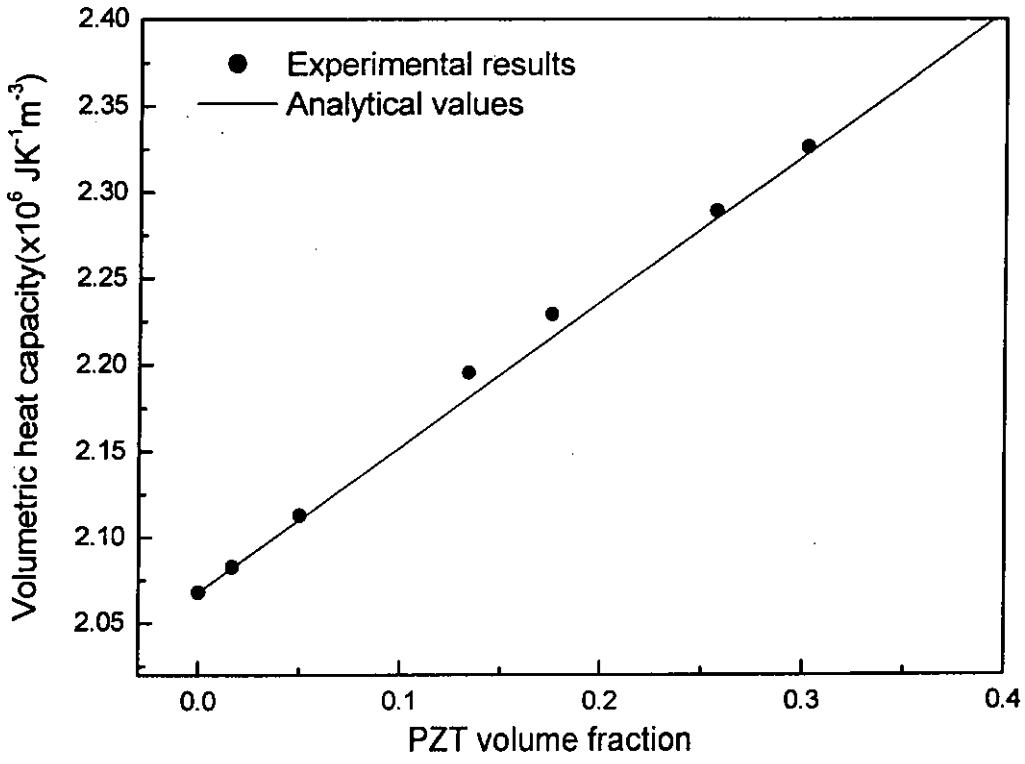

Figure 5.2 Volumetric heat capacity of PZT/PU composites at room temperature as a function of PZT volume fraction.

5.1.2 Thermal Diffusivity and Thermal Conductivity of PU, PZT/PU Composites and PZT

In this study, laser flash radiometry [Choy et al., 1987] was used to measure the thermal diffusivity of PU, PZT/PU composites and PZT. The flash method has proved to

be ideal for measuring the thermal diffusivity of polymer films as the method can be readily applied to small samples [Parker et al., 1961; Chen et al., 1977; Choy et al., 1978]. The method uses a short pulse of laser flashed to the front surface of a sample and measuring the temperature rise at the rear surface as a function of time. In order to reduce the disturbance of the temperature distribution in the sample, an infrared detector was employed to remotely monitor the thermal radiation from the rear surface of the sample.

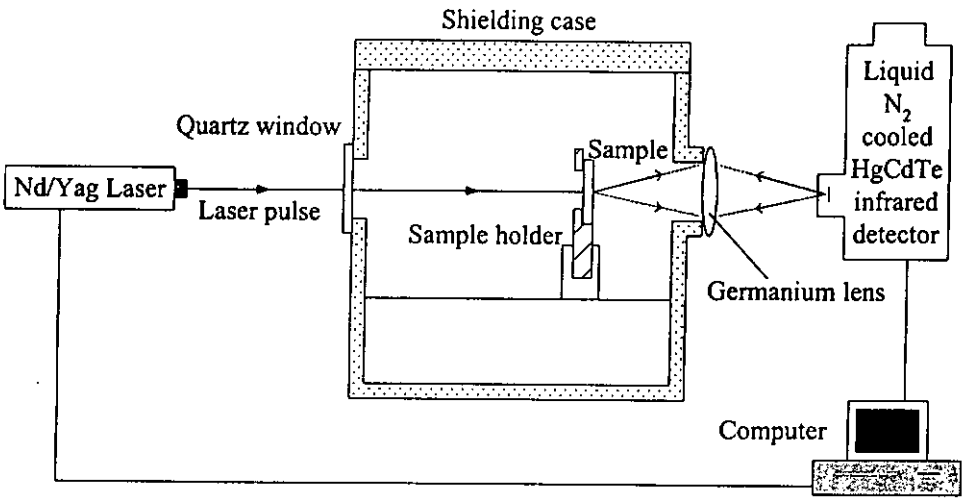

Figure 5.3 The setup of the flash radiometry measurement.

The setup of the laser flash radiometry measurement is shown in Figure 5.3. Samples used are of thickness about 120 to 150 μm. The sample thickness L are limited which should be small enough to meet the criterion $r/L > 10$ [Donaldson, 1972], where r is radius of the laser beam, so that the effect of the radial conduction is neglected. A one dimensional heat transfer analysis can be applied. The sample is clamped on the sample

holder which has a circular window (diameter = 6mm) for laser irradiation. A germanium lens placed at two-focal length from the sample rear surface is used for focusing the emitted thermal radiation onto the infrared detector which is placed at two-focal length on the other side of the lens.

A 10ns Nd/YAG laser pulse of wavelength 532nm was used to provide the thermal excitation. The liquid N_2 cooled HgCdTe infrared detector (Infrared Associates Inc.), operated in photoconductive mode, is particularly sensitive at 8-13 μm infrared radiation, having a rise time of 0.1 μs. The thermal signal detected by the infrared detector was sent to a computer. In order to improve the signal to noise ratio, the experiment was performed by averaging 30 laser shots. A microcomputer was used to control the laser flash and collect the thermal signal from the detector. A theoretical expression for the one dimensional thermal diffusion in the sample is shown below [Leung et al., 1984]:

$$\Theta(t) = \frac{S}{A}\left[(1-e^{-\alpha L})(1-e^{-\alpha' L}) - 2e^{-\alpha' L}\sum_{n=1}^{\infty}\left(\frac{1-(-1)^n e^{\alpha L}}{1+\frac{n^2\pi^2}{\alpha^2 L^2}}\right)\left(\frac{1-(-1)^n e^{\alpha' L}}{1+\frac{n^2\pi^2}{\alpha'^2 L^2}}\right)e^{-n^2 t/\tau_L}\right] \tag{5.7}$$

where $$\tau_L = \frac{L^2}{\pi^2 D_{th}} \quad (5.8)$$

$\Theta(t)$ is the radiometry signal from the rear surface collected at the infrared detector, S is a constant that depends on the flash energy and the heat capacity, temperature, and emissivity of the sample, α is the absorption coefficient of the sample at the excitation wavelength, α' is the infrared absorption coefficient of the sample over the detection spectral bandwidth, τ_L is the thermal diffusion time constant, L is the thickness and D_{th} is the thermal diffusivity. This theoretical expression was used to fit the captured temperature rise time profile and thus the thermal diffusion time constant was obtained. As a result, the thermal diffusivity D_{th} can be calculated by using Equation 5.8. Figure 5.4 shows the thermal diffusivities of PU and PZT/PU composites as a function of PZT volume fractions. From the figure, it can be seen that the diffusivity of PZT/PU composites increases with the increase of PZT content.

The thermal conductivities of the PU and PZT/PU composites can be calculated by substituting the thermal diffusivity, the density and the specific heat into Equation 5.3. The results are shown in Figure 5.5. It is obvious that, similar to thermal diffusivity, the thermal conductivity also increases with the volume fraction of PZT.

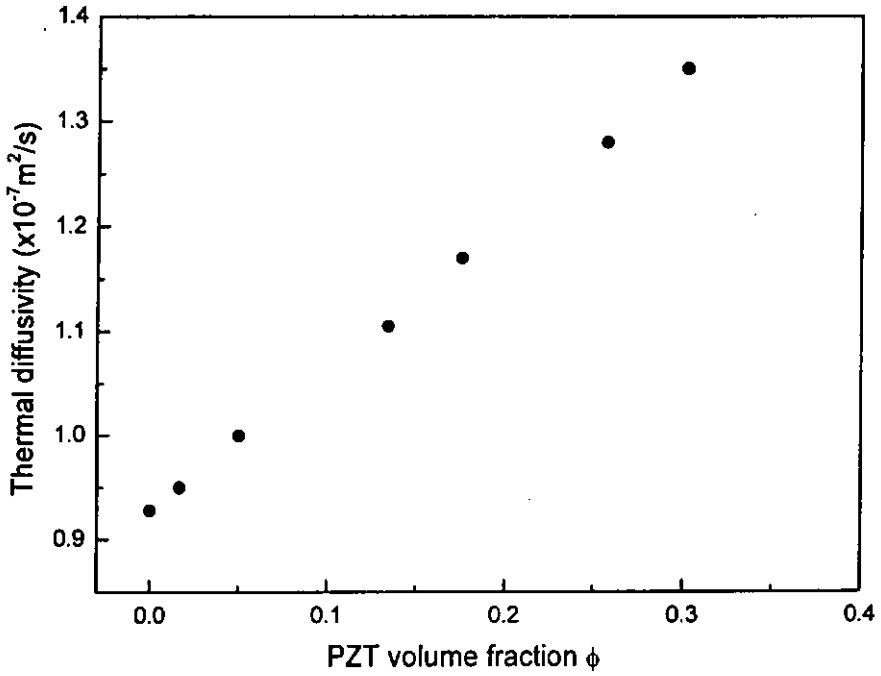

Figure 5.4 Thermal diffusivities of PU and PZT/PU composites.

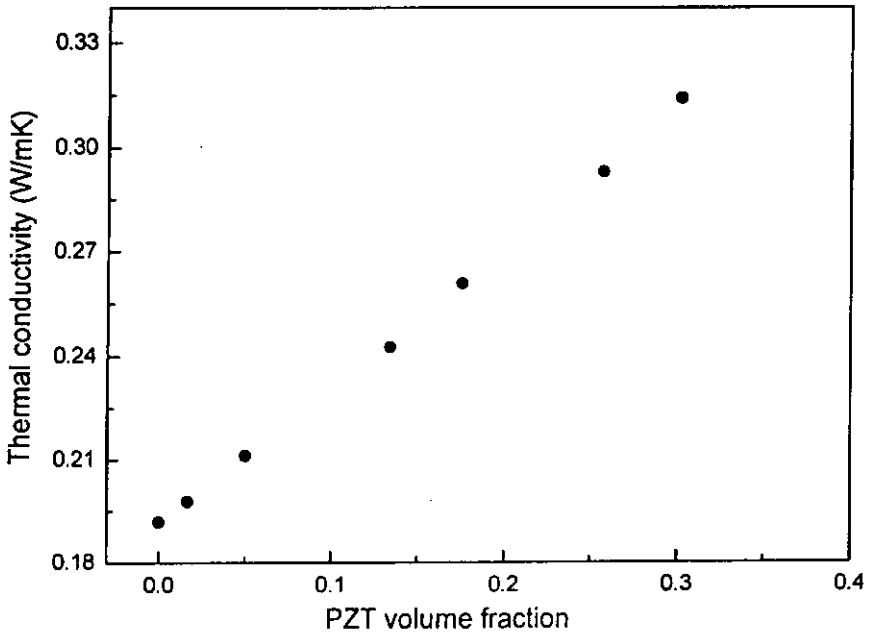

Figure 5.5 Thermal conductivity of PU and PZT/PU composites as a function of PZT volume fraction.

5.2 PZT/PU Composites as Pyroelectric Sensors

PZT ceramic is well known for its large pyroelectric effect and can be used as the sensing material for a thermal sensor. However, it is also sensitive to vibrations due to its strong piezoelectric effect. This will introduce electrical noise in thermal sensing applications. PU is a compliant elastomer and non-piezoelectric, so it would, on the one hand absorb the vibration and, on the other hand it would not generate electrical noise by itself. Therefore, PZT/PU composites are good thermal sensing materials with reasonable high pyroelectric coefficient but low piezoelectric noise due to environmental vibration. In addition, the permittivity of PZT/PU composites (up to 30% PZT) is very small compared with that of pure PZT, and thus there is an advantage in the figures of merit for pyroelectric sensor application [Sakamoto et al., 1998; Sakamoto et al., 2002]. As a result, the performance of PZT/PU composites thermal sensor would be better than pure PZT ceramic in terms of the signal to noise ratio, etc, to be discussed below.

5.2.1 Figures of Merit for Pyroelectric Materials

Besides specific heat, thermal diffusivity and thermal conductivity, figures of merit (FOM) are used to describe the contribution of the physical properties of a material to the performance of a pyroelectric sensor. Many pyroelectric materials have been investigated for sensor applications. However, the choice is not an obvious one as it

depends on many factors including the size of the sensor required, the operating temperature and the frequency. It is possible to formulate a number of FOM's [Whatmore, 1992; Kruse et al., 1997; Rogalski, 2000] which describe the contribution of the physical properties of a material to the performance of a device. For example, the current FOM F_i is defined as:

$$F_i = \frac{p}{C_v} \tag{5.9}$$

where p is the pyroelectric coefficient, $C_v = \rho c$ is the volumetric specific heat, ρ is the density and c is the specific heat at constant pressure. Another one is the voltage FOM F_v defined as:

$$F_v = \frac{p}{C_v \varepsilon_o \varepsilon_r} \tag{5.10}$$

The detectivity FOM F_D is:

$$F_D = \frac{p}{C_v (\varepsilon_o \varepsilon_r \tan\delta)^{1/2}} \tag{5.11}$$

where ε_0, ε_r and $\tan\delta$ are the dielectric permittivity of the vacuum, relative dielectric permittivity and loss tangent respectively.

The first two FOM's describe the influence of the pyroelectric material on the current and voltage responsivity of a pyroelectric sensor, while F_D is related to the specific detectivity D^*. The current and voltage responsivity and the detectivity of the PZT/PU composite materials are given in section 5.2.4.

By substituting the measured values of p, ρ, c, ε_r and $\tan\delta$ into Equations 5.9 to 5.11, the values of F_i, F_v and F_D of pure PU, PZT/PU composites and PZT are calculated and listed in Table 5.1.

Table 5.1 Current, voltage and detectivity figures of merit (FOM) of PZT/PU composites with various volume fraction of PZT.

PZT volume fraction	F_i ($\times 10^{-12}$ m/V)	F_v ($\times 10^{-3}$ m^2/C)	F_D ($\times 10^{-7}$ Pa$^{-1/2}$)
0 (PU)	0.03	0.5	0.2
2	2	29	14
5	6	77	39
13	17	169	96
18	22	183	114
26	32	200	142
30	38	188	153
100 (PZT)	113	7.1	73

Table 5.1 shows that the current figure of merit of the PZT/PU composite is higher when the content of PZT increases. As a result, the PZT/PU composite with higher PZT content should be selected for a pyroelectric sensor operated in the current mode.

On the other hand, the voltage figure of merit of the composite with 26% volume fraction of PZT is 200×10^{-3} m^2/C which is at a maximum amongst other samples. It is also much higher than that of PZT (7.1×10^{-3} m^2/C) and is therefore quite suitable for use

in a pyroelectric sensor operated in the voltage mode.

In addition, a higher value of the detectivity figure of merit can be obtained when the volume fraction of PZT increases. However, it diminishes when there is too much PZT content in the composite and finally reaches 73×10^{-7} $Pa^{-1/2}$ which is the detectivity figure of merit of pure PZT. In this study, the highest detectivity figure of merit of PZT/PU is 153×10^{-7} $Pa^{-1/2}$ which comes from the composite with 30% PZT volume fraction.

In conclusion, from the results of F_i, F_v and F_D of the PZT/PU system, the composites with 26% and 30% PZT volume fraction were selected as sensing materials for fabricating prototype pyroelectric sensors. The details of the fabrication and the performance of the pyroelectric sensors were introduced in the following sections.

5.2.2 Pyroelectric Sensors

A simple pyroelectric detector consists of a slice of pyroelectric material with metal electrodes on opposite faces. The pyroelectric material is poled such that the polarization direction is perpendicular to the electrode faces. Two configurations as shown in Figure 5.6, one with face electrodes and the other edge electrodes, are commonly used; the arrows indicate the polarization direction. Both configurations form a parallel-plate capacitor. In this study, the face electrode configuration is used.

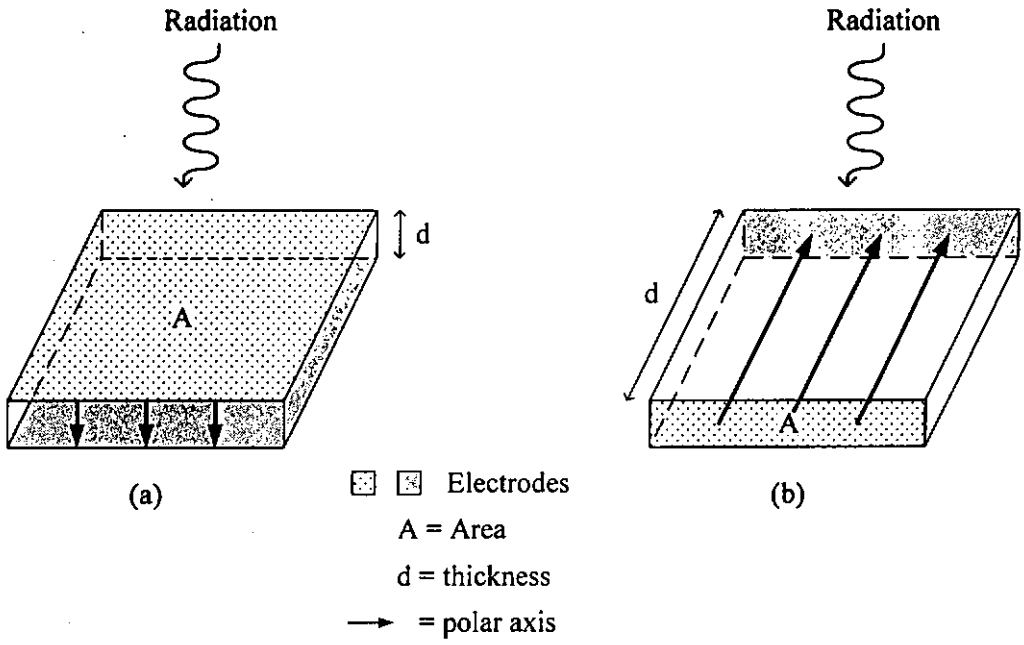

Figure 5.6 Electrode configurations of Pyroelectric detectors. **(a)** Face electrodes **(b)** Edge electrodes

Radiation is absorbed at the front surface and the resulting heat diffuses through the thin film electrode into the pyroelectric material causing a change in temperature as well as in polarization. In addition, for providing a high absorption in the spectral region of interest, the front surface of the sensor is usually "blackened".

A pyroelectric sensor can only respond to temperature change, but produce no signal for a steady temperature. For this reason, a pyroelectric sensor can only be used for an ac radiation and at a frequency high enough for electrical leakage to be ineffective. In other words, the pyroelectric sensor can only be used to detect changes in irradiance.

Generally, the detector output is characterized by a response transfer function to the varying radiation. The radiation may be sinusoidal [Willardson et al., 1970], step-like [Simhony et al., 1971], or rectangular [Shaulov et al., 1972]. Sinusoidal modulation is used in this study to characterize the sensor response.

5.2.3 Principle of Operation of Thermal Detectors

The simple heat model of a thermal detector and the equivalent circuit [Rogalski, 2000] are shown in Figure 5.7. In the equivalent circuit, the detector is represented by a thermal capacitance (or heat capacity) C_{th} parallel with a thermal conductance G_{th} to its surrounding which is represented by a heat sink at a constant temperature T. When the detector receives a radiation input, the rise in temperature is found by solving the heat balance equation [Ristic, 1994; Kanno et al., 1994]:

$$C_{th}\frac{d\Delta T}{dt} + G_{th}\Delta T = \eta\Phi \tag{5.12}$$

where ΔT is the uniform temperature difference between the detector and its surrounding caused by the incident radiation, and η is the fraction of the incident radiation power W that is converted into heat.

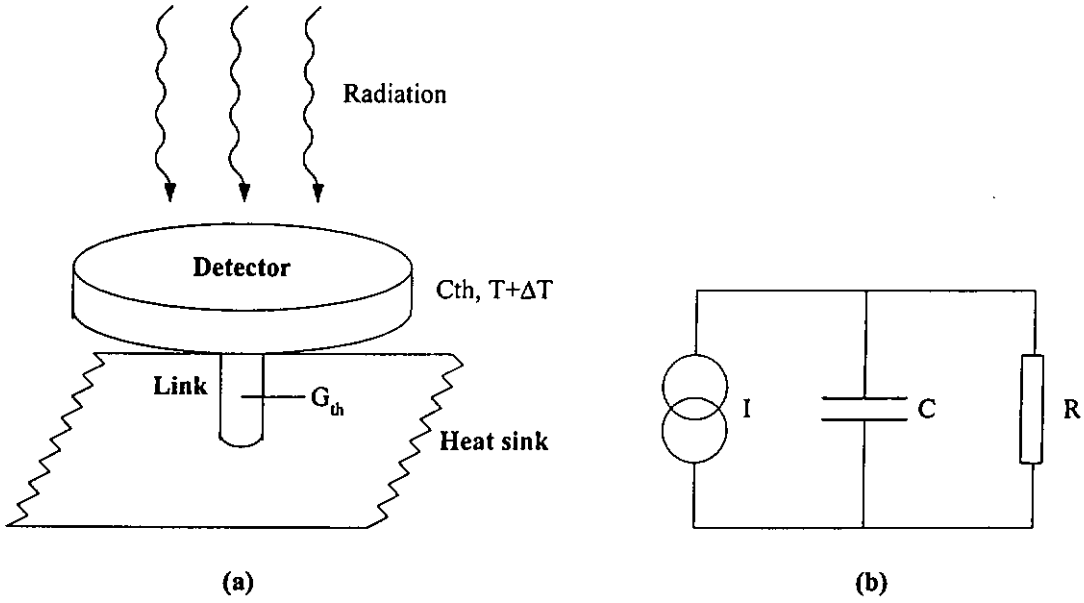

Figure 5.7 (a) The simple heat model of a thermal detector and **(b)** the equivalent circuit.

Assume the radiant power to be a periodic function, $W = W_1 \exp(j\omega t)$ where W_1 is the amplitude of sinusoidal radiation, the steady-state solution of differential equation is:

$$\Delta T(\omega,t) = \frac{\tau_{th}\eta W_1}{C_{th}(1 + j\omega\tau_{th})}\exp(j\omega t) \qquad (5.13)$$

where $\tau_{th} = C_{th}/G_{th}$ is the thermal time constant.

5.2.4 Responsivity, Noise Equivalent Power and Detectivity of Pyroelectric Sensor

5.2.4.1 Current Responsivity

The concept of responsivity has been developed to quantify the sensor output per watt of radiant optical power input [Dereniak et al., 1996]. When the pyroelectric sensor receives an incoming radiation, the temperature difference gives rise to a surface charge on the electrodes and generates a short circuit pyroelectric current as shown in Equation 4.8. Substituting Equation 5.13 into 4.8 gives:

$$\left|I_p\right| = \frac{\eta p A W_1}{C_{th}} \frac{j\omega\tau_{th}}{(1+j\omega\tau_{th})} \exp(j\omega t) \tag{5.14}$$

where A is the electrode area and p is the pyroelectric coefficient. The root mean square value of induced current I_p is given by

$$I_{p,rms} = \frac{\eta p A W_{1,rms}}{C_{th}} \frac{\omega\tau_{th}}{(1+\omega^2{\tau_{th}}^2)^{1/2}} \tag{5.15}$$

The current responsivity R_i is defined as:

$$R_i = \frac{I_{p,rms}}{W_{1,rms}} = \frac{\eta p}{C_v d}\left[\frac{\omega\tau_{th}}{(1+\omega^2{\tau_{th}}^2)^{1/2}}\right] \tag{5.16}$$

where $W_{1,rms}$ is the root mean square value of W_1, $C_{th} = C_v Ad$, C_v is the volumetric heat capacity and d is the thickness.

5.2.4.2 Voltage Responsivity

The induced surface charge ΔQ from the pyroelectric material produces an open circuit voltage ΔV_p across the sensor electrodes as shown below

$$\Delta V_p(\omega,t) = \frac{\Delta Q(\omega,t)}{C} = \frac{Ap\Delta T(\omega,t)}{\varepsilon_o \varepsilon_r (A/d)} = \frac{pd}{\varepsilon_o \varepsilon_r} \Delta T(\omega,t) \tag{5.17}$$

where C is the sensor capacitance and ε_r is the relative permittivity of the sensing material. By substituting Equation 5.13 into 5.17, the root mean square value of the induced voltage can be written as

$$V_{p,rms} = \frac{\eta p W_{1,rms}}{C_v \varepsilon_o \varepsilon_r A} \frac{\tau_{th}}{(1+\omega^2 {\tau_{th}}^2)^{1/2}} \tag{5.18}$$

The voltage responsivity R_v is defined as:

$$R_v = \frac{V_{p,rms}}{W_{1,rms}} = \frac{\eta p}{C_v \varepsilon_o \varepsilon_r A} \left[\frac{\tau_{th}}{(1+\omega^2 {\tau_{th}}^2)^{1/2}} \right] \tag{5.19}$$

5.2.4.3 Noise Equivalent Power

The noise equivalent power (NEP) is defined as the radiant power, W_1, incident on a detector that yields a signal to noise ratio (SNR) of 1 [Dereniak et al., 1996]. For a pyroelectric sensor, the SNR can be expressed in terms of current responsivity as

$$SNR = \frac{R_i W_1}{i_n} \tag{5.20}$$

where i_n is the root mean square noise current and R_i is current responsivity. For SNR = 1, the current NEP is equal to

$$NEP = \frac{i_n}{R_i} \tag{5.21}$$

Similarly, the voltage NEP is equal to

$$NEP = \frac{V_n}{R_v} \tag{5.22}$$

where V_n is the root mean square noise voltage and R_v is voltage responsivity..

5.2.4.4 Detectivity

The disadvantage of using NEP to describe a detector performance is that NEP is

dominated by its dependence on the square root of the detector area and the square root of the bandwidth of the measurement. So the NEP of two materials cannot be compared if their area or measurement bandwidth is different. As a result, a new term, normalized detectivity D*, is defined [Kruse et al., 1962; Dereniak et al., 1996]:

$$D^* = \frac{\sqrt{A\Delta f}}{NEP} \tag{5.23}$$

where A is the electrode area and Δf is the bandwidth of the measurement.

In the case of a sensor dominated by the ac Johnson noise, the noise current can be written as [Johnson, 1928]:

$$i_n = (\frac{4kT\Delta f}{R})^{1/2} \tag{5.24}$$

where k is Boltzmann's constant and T is the absolute temperature. Since the pyroelectric sensors are capacitive and the loss resistance R is equal to $1/(C\ \omega \tan\delta)$ [Kruse, 1997] where C is the capacitance, ω is the angular frequency and $\tan\delta$ is the loss tangent. Putting Equations 5.21 and 5.24 into 5.23, D* can be written as

$$D^* = \frac{\eta p}{d^{1/2}} \frac{1}{\sqrt{4kT\omega}} \frac{1}{C_v \sqrt{\varepsilon_o \varepsilon_r \tan\delta}} \left[\frac{\omega \tau_{th}}{(1+\omega^2 {\tau_{th}}^2)^{1/2}} \right] \tag{5.25}$$

5.2.5 Sensor Fabrication

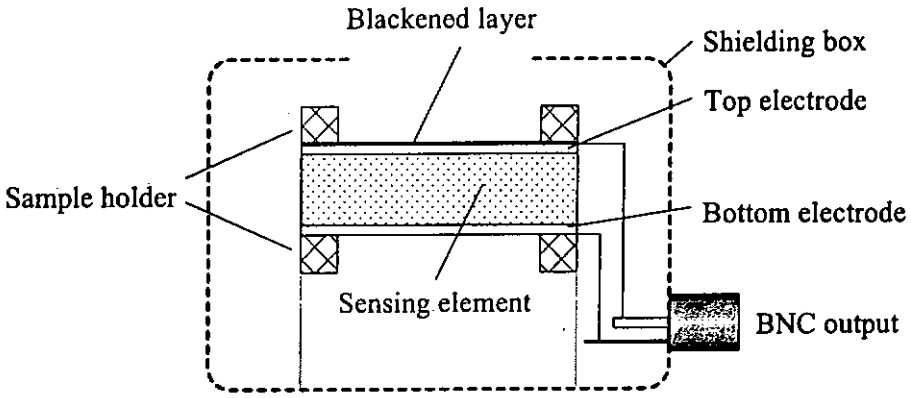

Figure 5.8 Schematic diagram of the pyroelectric sensor.

PZT/PU composites of 26% and 30% PZT were used as the sensing materials for the pyroelectric sensors. Films of different thicknesses were prepared by the hot pressing method. The thinner films (<60 μm) were pressed onto aluminum foil (~13 μm) as the bottom electrode. A 20mm circular gold electrode was sputtered on the top surface. For the thicker films (>60 μm) gold electrodes were sputtered on both surfaces. The films were then poled in silicone oil under a field of 20MV/m for one hour at room temperature. After heating at 60°C for 10 hours in short circuit condition, the film surface to be irradiated was painted with thin black layers. The film was then mounted in a sample holder and put in the shielding box as shown in Figure 5.8 for the following measurements.

5.2.6 Responsivity Measurement

5.2.6.1 Current Responsivity Measurement

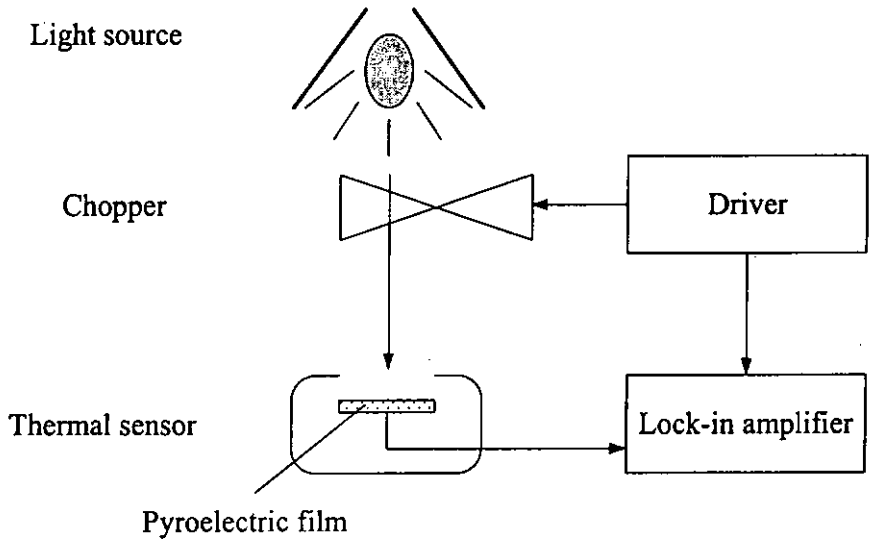

Figure 5.9 Schematic diagram of the current responsivity measurement.

Figure 5.9 shows the experimental set-up of the current responsivity measurement. In order to reduce the electrical noise, the pyroelectric element was mounted in a shielded box. A 20 mm circular window was opened on the box for the incident radiation. Light emitted from a 75W halogen lamp was modulated by a speed controlled optical chopper. The pyroelectric current generated by the element was measured by a lock-in amplifier (SR510 Stanford Research). A chopper driver (BC200 Scitec Instrument) was used to control the optical chopper and also to provide the reference

signal for the lock-in amplifier. The pyroelectric current was measured between 2 Hz and 180 Hz. The incident power of the non-modulated light beam was measured by a power meter (364 Scientech). As a result, the current responsivity R_i was calculated by using Equation 5.16.

Figures 5.10 (a) and (b) show the current responsivity of PZT/PU composite sensor elements of 26% and 30% PZT respectively. From the graphs, we find that the current responsivity of the composites is higher at low frequency especially for the thinner composites (43 μm). As the frequency increases, the current responsivity becomes lower. On the other hand, the current responsivity also exhibits thickness dependence which means that the thinner composite elements produce larger current responses.

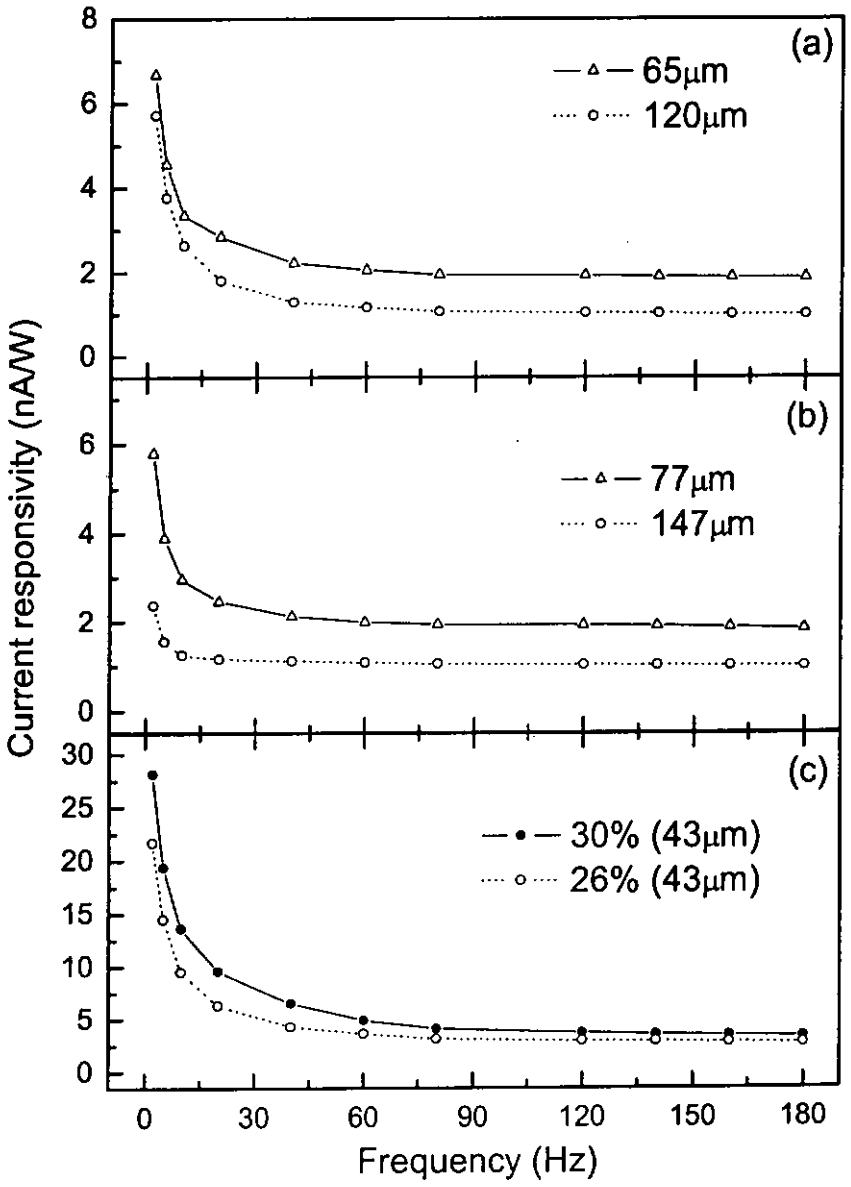

Figure 5.10 Current responsivity of PZT/PU composites of **(a)** 26%, **(b)** 30% and **(c)** 26% and 30% (43 μm) PZT volume fraction versus frequency.

5.2.6.2 Voltage Responsivity Measurement

The experimental setup of the voltage responsivity measurement (Figure 5.11) was similar to that of the current responsivity measurement. The internal impedance of the lock-in amplifier (100 MΩ) was not high enough to couple the PZT/PU pyroelectric sensor for open-circuit voltage measurement. Therefore, the voltage signal from the sensor was coupled to a JFET high impedance circuit before feeding to the lock-in amplifier. The voltage response of the pyroelectric sensor obtained was then used to calculate the voltage responsivity R_v by Equation 5.19. The results are shown in Figure 5.12.

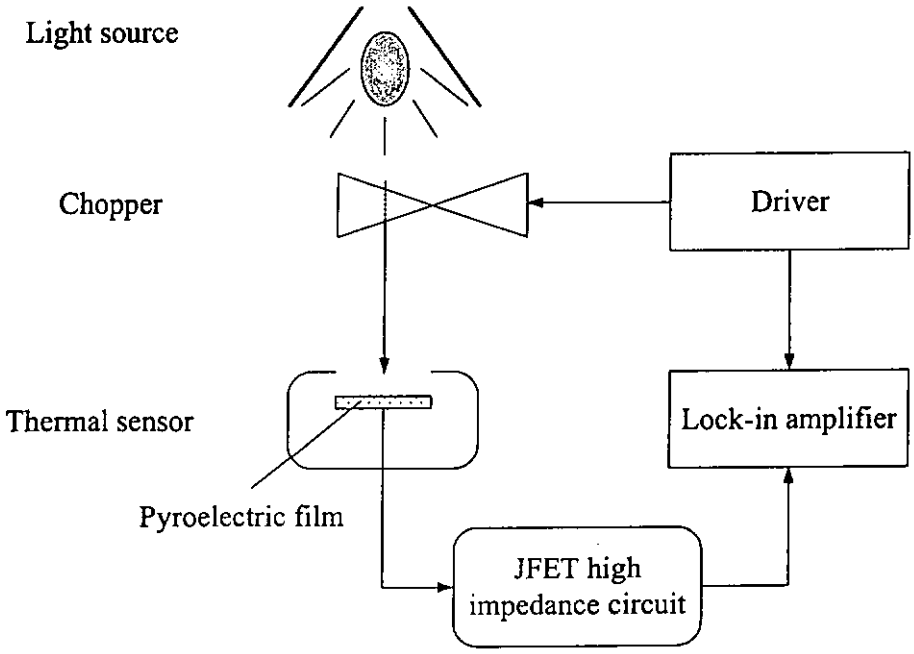

Figure 5.11 Schematic diagram of the voltage responsivity measurement.

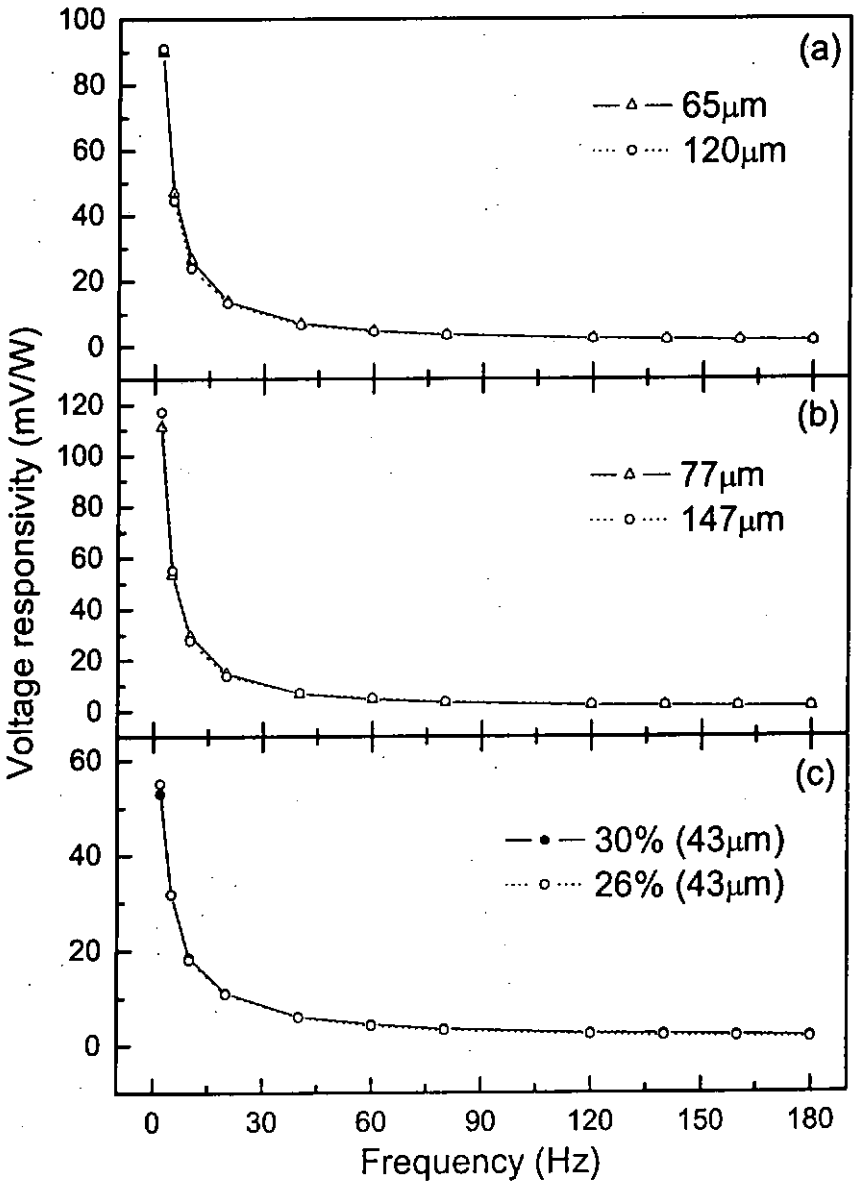

Figure 5.12 Voltage responsivity of PZT/PU composites of **(a)** 26%, **(b)** 30% and **(c)** 26% and 30% (43 μm) PZT volume fraction versus frequency.

As shown in Figure 5.12, the voltage responsivity of the PZT/PU composite sensor elements is similar to that of the current responsivity. The voltage responsivity is higher at lower frequency and drops to almost a constant value at higher frequency. However, the voltage responsivity is independent of thickness of the composites at frequencies higher than 40Hz. At low frequency, the voltage responsivity of thin composites is lower than thicker composites. It may be due to the higher heat capacity of the aluminum substrate at the rear surface, so that the temperature difference between the surfaces is reduced, thus producing a lower voltage at the electrodes. At higher frequencies, the temperature difference is already small, thus the influence of the substrate heat capacity is no longer significant.

5.2.6.3 Noise measurement

The setups for the noise measurements of current noise and voltage noise of the pyroelectric sensor are shown in Figures 5.13 and 5.14 respectively. Both the current noise and the voltage noise were measured by the lock-in amplifier at 1 Hz equivalent noise bandwidth at different frequencies. In order to obtain a more stable noise value, the window of the pyroelectric sensor was covered by a metal film so that the pyroelectric sensor box was completely shielded. The noise equivalent power (NEP) and the detectivity D^* are calculated by using Equations 5.21 to 5.23. The results are shown in Figures 5.15 to 5.18.

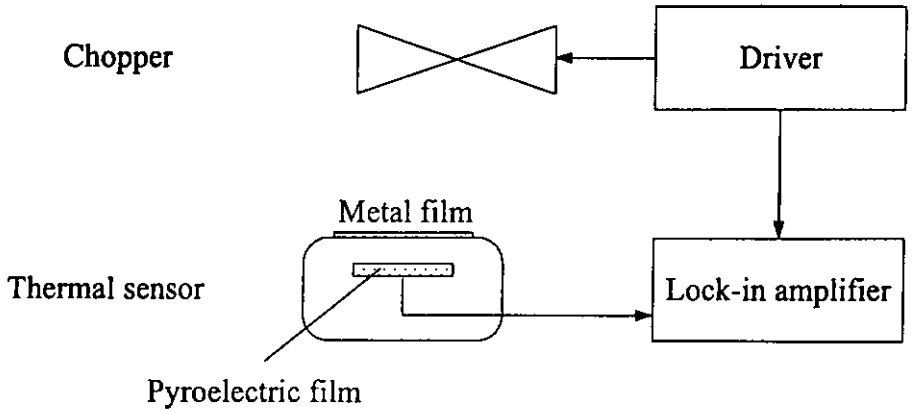

Figure 5.13 Schematic diagram of the current noise measurement.

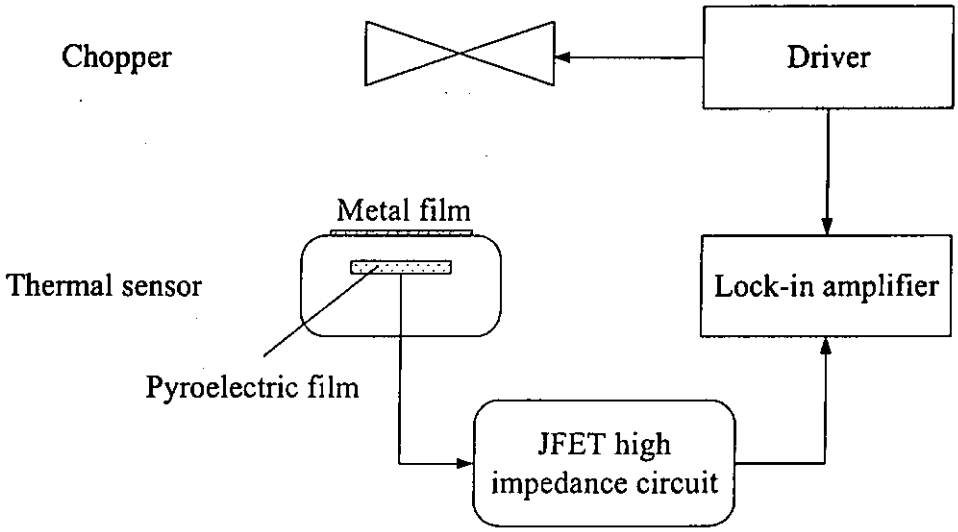

Figure 5.14 Schematic diagram of the voltage noise measurement.

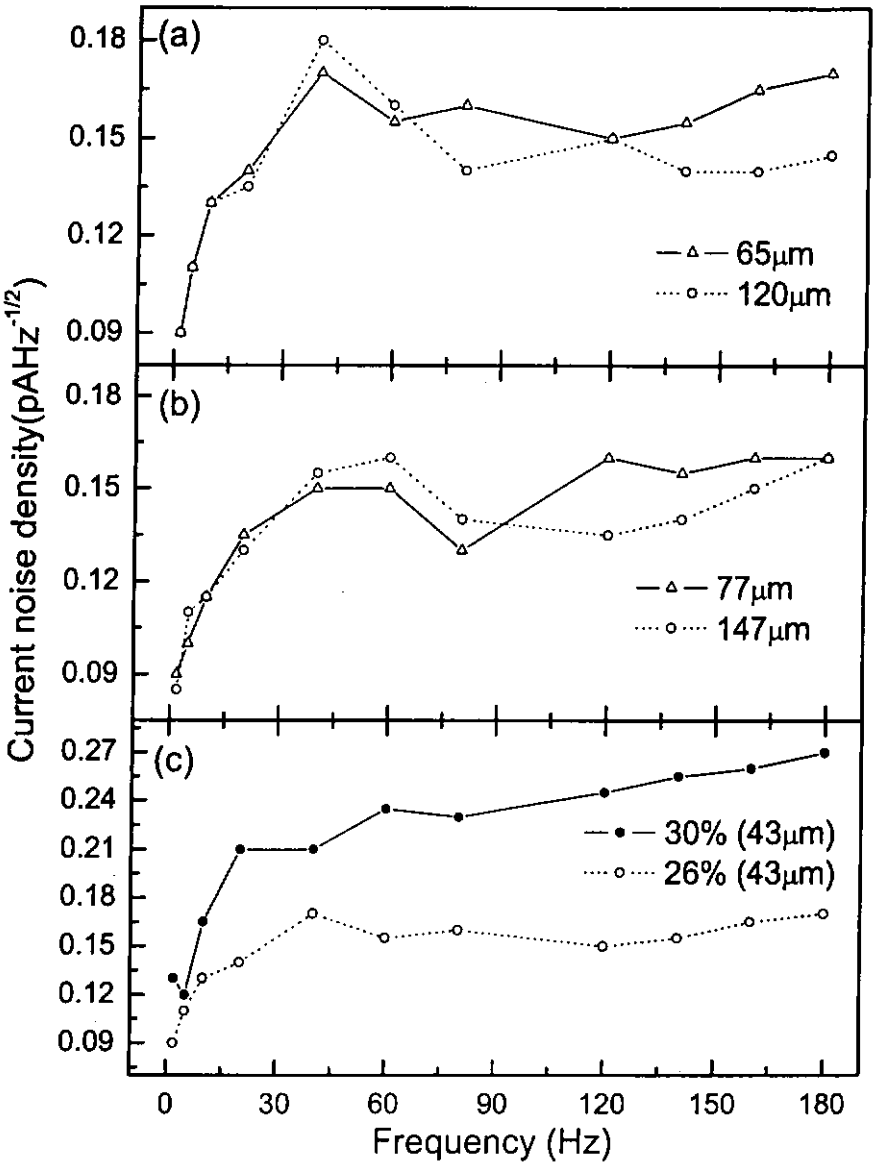

Figure 5.15 Current noise of PZT/PU composites of **(a)** 26%, **(b)** 30% and **(c)** 26% and 30% (43 μm) PZT volume fraction versus frequency.

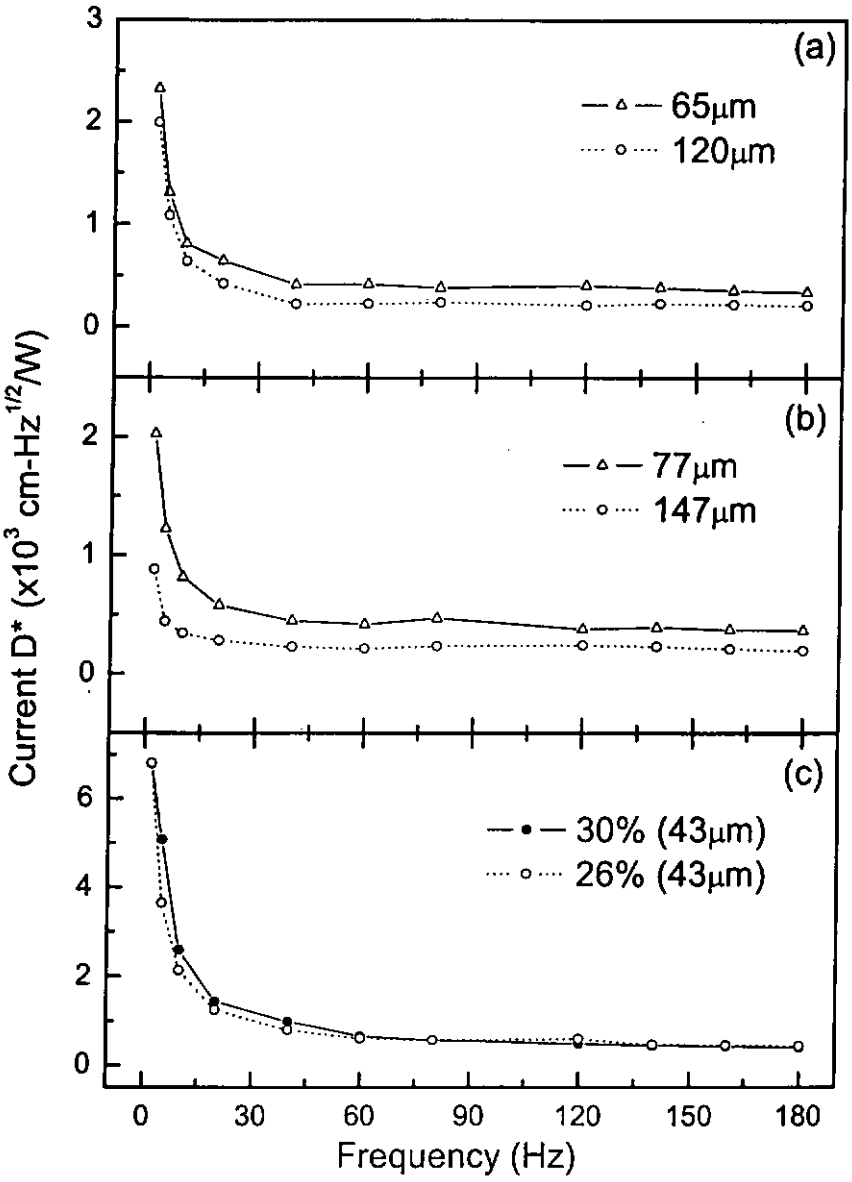

Figure 5.16 Current detectivity D* of PZT/PU composites of **(a)** 26%, **(b)** 30% and **(c)** 26% and 30% (43 μm) PZT volume fraction versus frequency.

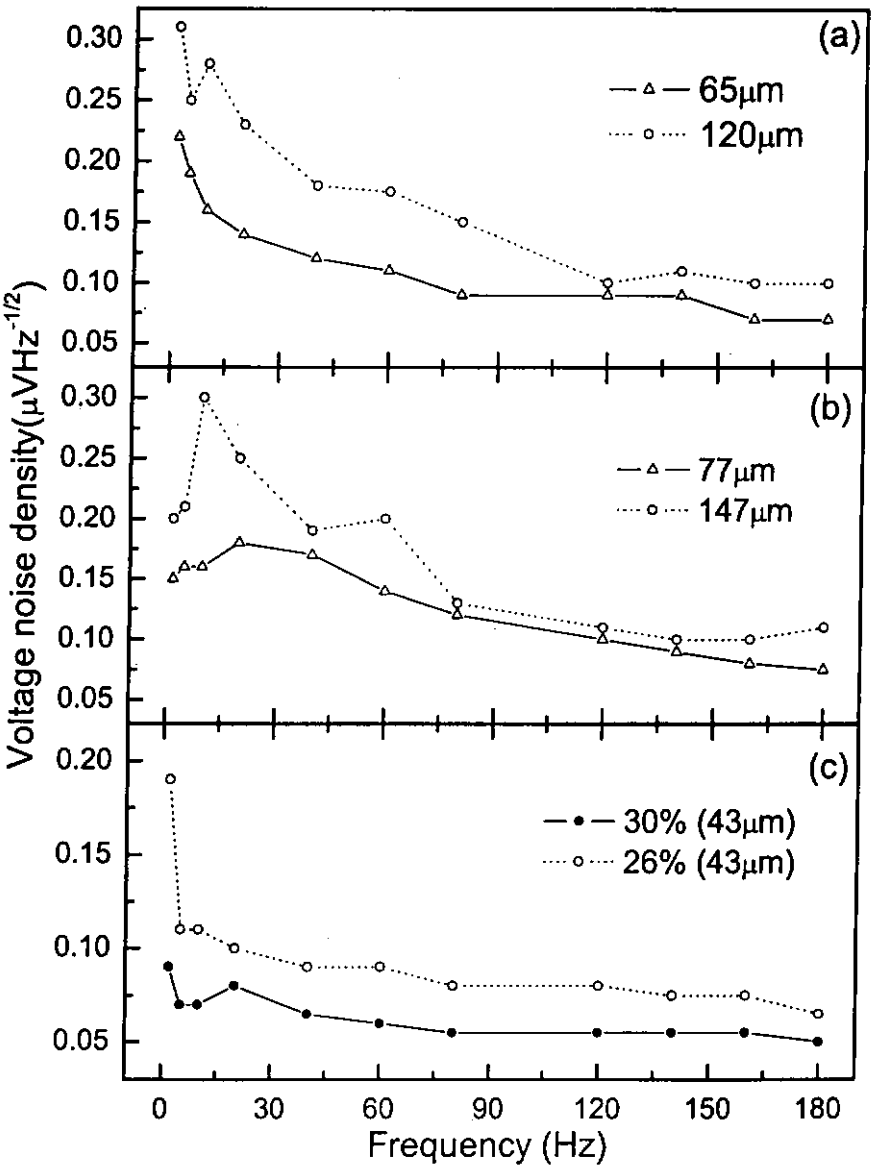

Figure 5.17 Voltage noise of PZT/PU composites of **(a)** 26%, **(b)** 30% and **(c)** 26% and 30% (43 μm) PZT volume fraction versus frequency.

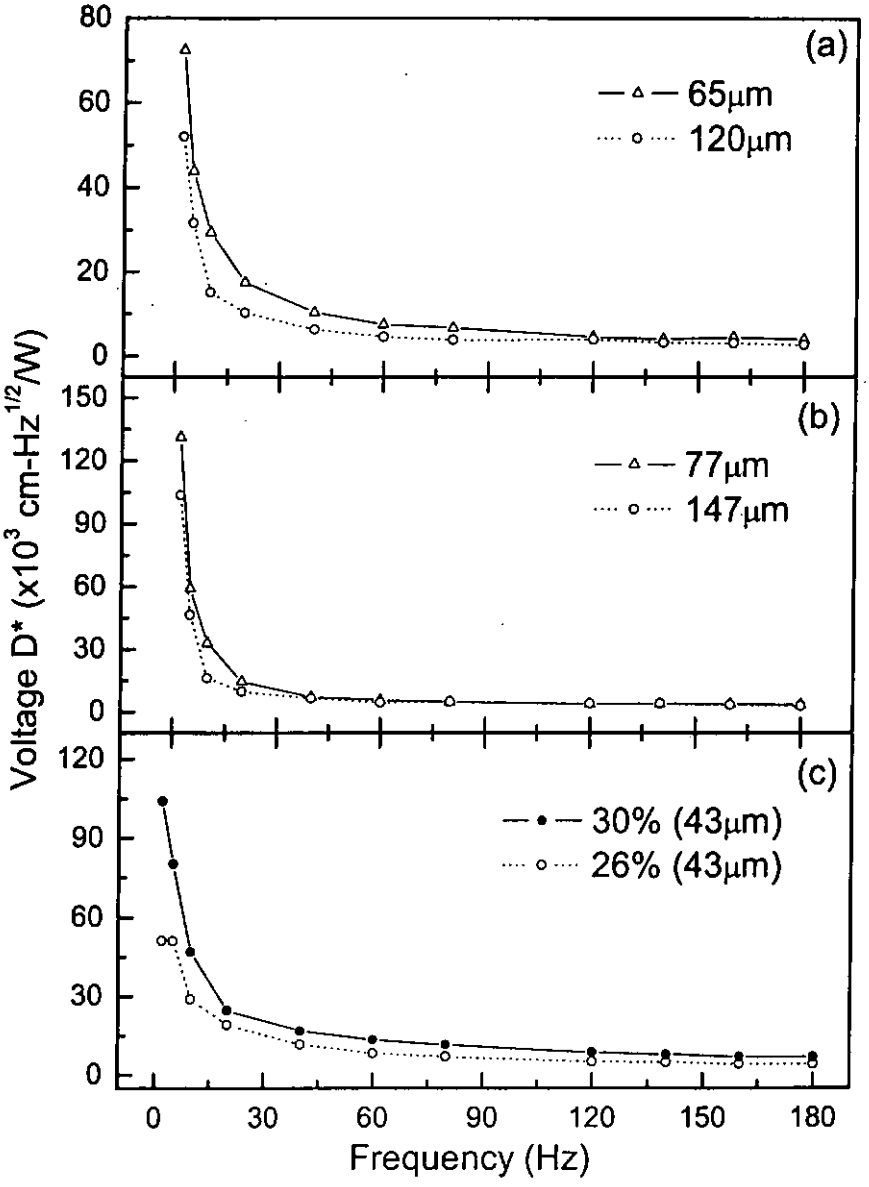

Figure 5.18 Voltage detectivity D* of PZT/PU composites of **(a)** 26%, **(b)** 30% and **(c)** 26% and 30% (43 μm) PZT volume fraction versus frequency.

From Figure 5.15, it can be seen that the current noise increases with frequency. The thinnest samples exhibit the highest current noise especially for the 30% PZT composite. Despite their higher current noise, the overall detectivity in current measurement (Figure 5.16) is still higher, particularly at low frequency. At high frequency, the current detectivity of the thinner composites is still slightly higher than the thicker composite samples. As a result, it is preferable to have thin sensors to achieve a higher detectivity in current measurement.

On the other hand, for voltage measurement, the voltage noise is higher at low frequency and decreases at higher frequency. The thickness dependence is contrary to that in the current noise; the noise of thicker samples is larger which also affects the overall voltage detectivity. Figure 5.18 shows the voltage detectivity of the thinner composite sensor element is larger; it is more evident at the low frequency region. In conclusion, similar as in the current measurement, a thinner composite sensor element is preferable to achieve have a better detectivity performance for the voltage measurement.

Chapter 6

Electrostriction of PZT/PU Composites

6.1 Electric Field Induced Strain of PZT/PU Composites

Electric field induced strain of pure PU and PZT/PU composites with 5%, 13%, 18%, 26% and 30% volume fraction of PZT were measured by a modified Michelson interferometer under the application of the "stepped" electric field shown in Figure 6.1. The details of the measurement setup were already given in Chapter 2. The thicknesses and electrical conductivities of the samples are given in Table 6.1. The electrostrictive responses of pure PU and the PZT/PU composites are shown in Figure 6.2. There is a great difference in the electrostrictive responses of pure PU and the composites. For PU, as the electric field increases, a negative strain was observed. It implies that PU always contracts in the direction of the field. It is interesting to point out that the strains were proportional to the square of the electric fields, following the electrostrictive nature of

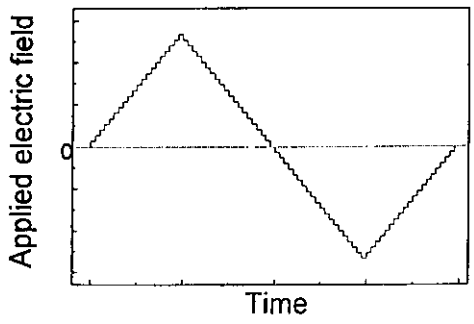

Figure 6.1 Time profile of the application of the "stepped" electric field.

Table 6.1 Thicknesses and conductivities of the PZT/PU composites with different PZT content.

PZT volume fraction (%)	Thickness (mm)	Conductivity (10^{-10} $\Omega^{-1}m^{-1}$)
5	180	3.4
13	142	5.7
18	150	5.9
26	151	4.5
30	153	6.0

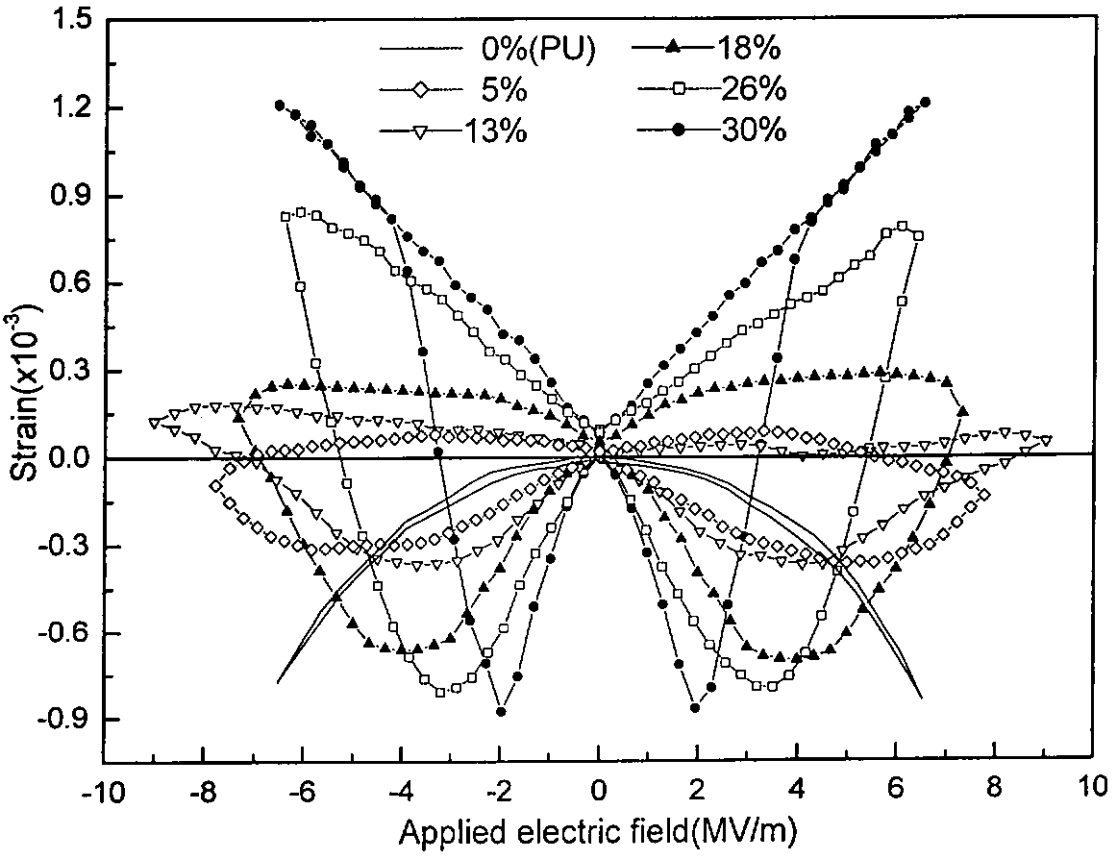

Figure 6.2 Induced strains of PU and PZT/PU composites under the "stepped" electric field.

the polymer. The maximum strain was -0.08% at a field of 6.5 MV/m. For the 5% and above PZT/PU composites, contractive strains were observed at low fields. As the field increased, the composites reached a maximum contraction and then "expanded" at higher fields. The strains increased from negative to positive if the applied fields were sufficiently high. As the field decreased, the strains of most composite samples decreased almost proportionally to the applied fields. The electrostrictive responses of the samples under the reversed electric field experienced a similar change as in the previous field history. As a result, symmetrical electromechanical hystereses for PZT/PU composites were observed. It is believed that the electromechanical behaviors of the composites are mainly a result of the polarization changes in the PZT inclusions in the PU matrices.

Another interesting feature of this electrostrictive response is related to the electric field and contraction strain at which the sample switches from contraction to expansion. As shown in Figure 6.3, the higher the PZT content, the lower the external field required to switch the polarizations of the PZT inclusions in the PU matrix and the higher the maximum contraction strain. As the PZT content increases, the local field of the PZT inclusions increases correspondingly [Wong et al., 2002] therefore a lower external switching field is needed to flip the anti-parallel polarization. On the other hand, broader switching regions are observed in the induced strain hysteresis loops of the composites with lower volume fraction of PZT. The electrostrictive responses of the composites are the results of competition between the contraction of PU and the hysteretic electromechanical response of PZT.

The expansion of the composites under the action of electric fields in the same direction as the polarization of the inclusions may be exploited for applications, especially for the composites with higher PZT volume fraction. In comparison with pure PU, the magnitude of the expansion of the 30% PZT/PU composite is larger than that of the contraction of pure PU even at fields as large as 6 MV/m. In addition, this expansion is repeatable and almost linearly dependent on the applied field. As a result, PZT/PU composites with relatively high volume fraction of PZT are suitable for actuators.

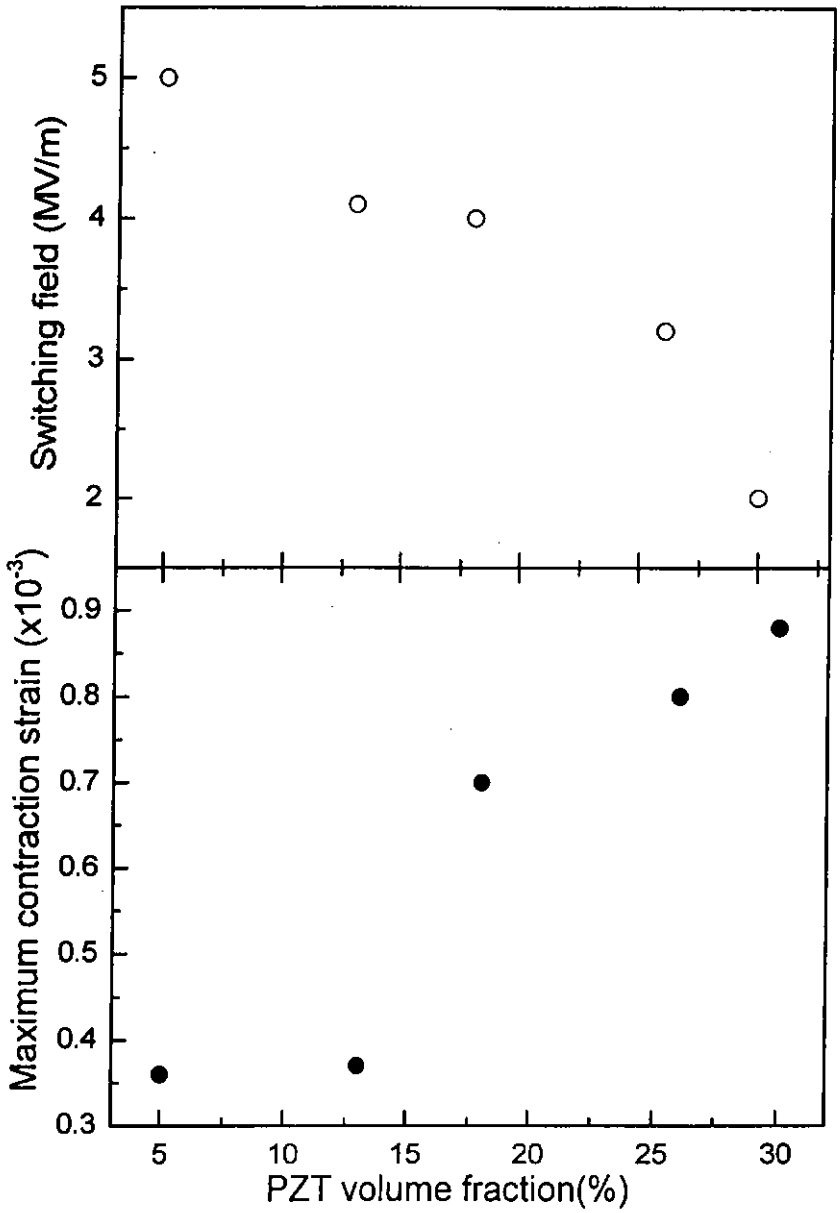

Figure 6.3 Switching field and maximum contraction strain of the PZT/PU composites versus PZT volume fraction.

6.2 *D-E* Loops of PZT/PU Composites

In order to realize the relation of the induced charges and the electrostriction of PZT/PU composites, the electric displacement and the electric field induced strain were measured at the same time under the application of a "stepped" electric field as shown in Figure 6.1. The block diagram of the measurement setup is shown in Figure 6.4. For the measurement of electric displacement, a 10 μF reference capacitor was connected serially with the sample. The voltage across the reference capacitor was measured by a multimeter (HP 34401A). Electric displacements were calculated from Equation 2.17.

The electric field induced strain and the instantaneous electric displacement of the pure PZT, PU and PZT/PU composite with 30% volume fraction of PZT were measured. The sample thickness of the pure PZT film was 150 μm and both of its surfaces were coated with 8 mm circular aluminum electrodes. The thicknesses of the hot pressed PU and the PZT/PU composite samples were 230 μm and 153 μm respectively. Circular gold electrodes of 6 mm diameter were coated by sputtering. The measurement results of the pure PZT, PU and the PZT/PU composite are shown in the Figures 6.5, 6.6 and 6.8 respectively.

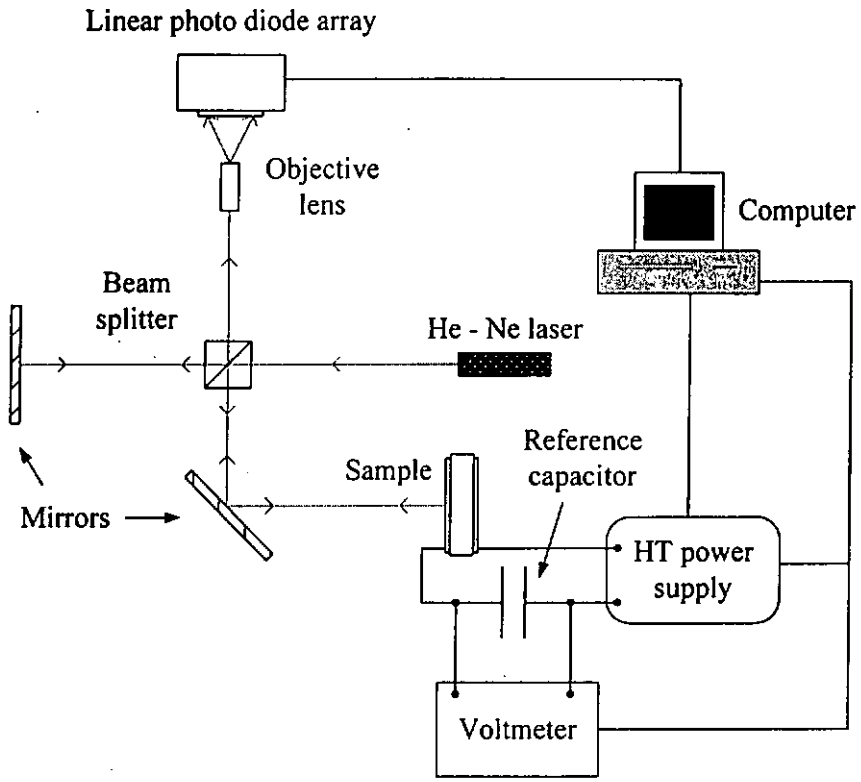

Figure 6.4 Setup of the electric field induced strain and instantaneous electric displacement measurement.

In Figure 6.5, the strain of PZT in the thickness direction forms a hysteresis loop of butterfly shape under the application of the stepped electric field with 5s time duration for each step. At the same time, the electric displacement also forms a conventional square-like *D-E* hysteresis loop. The remanent polarization of the sample is about 30 $\mu C/cm^2$ and the coercive electric field is about 0.85 MV/m. In addition, a switching in the strain, i.e. from a contraction to a sudden expansion, occurs when the electric displacement exhibits an abrupt change at around the coercive field. It is the flipping of the PZT dipoles which induces the large electric displacement as well as the sudden change in strain.

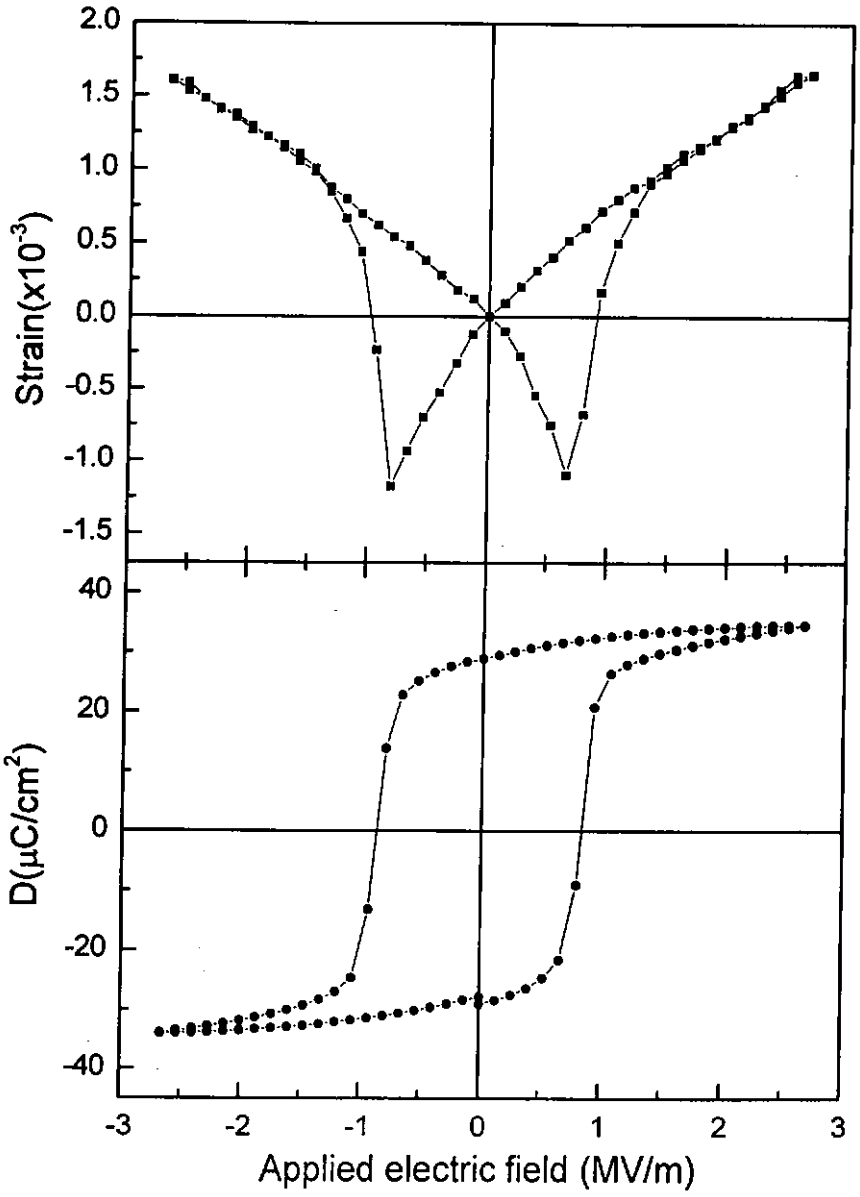

Figure 6.5 Electric field induced strain and instantaneous electric displacement of pure PZT under the application of the "stepped" electric field.

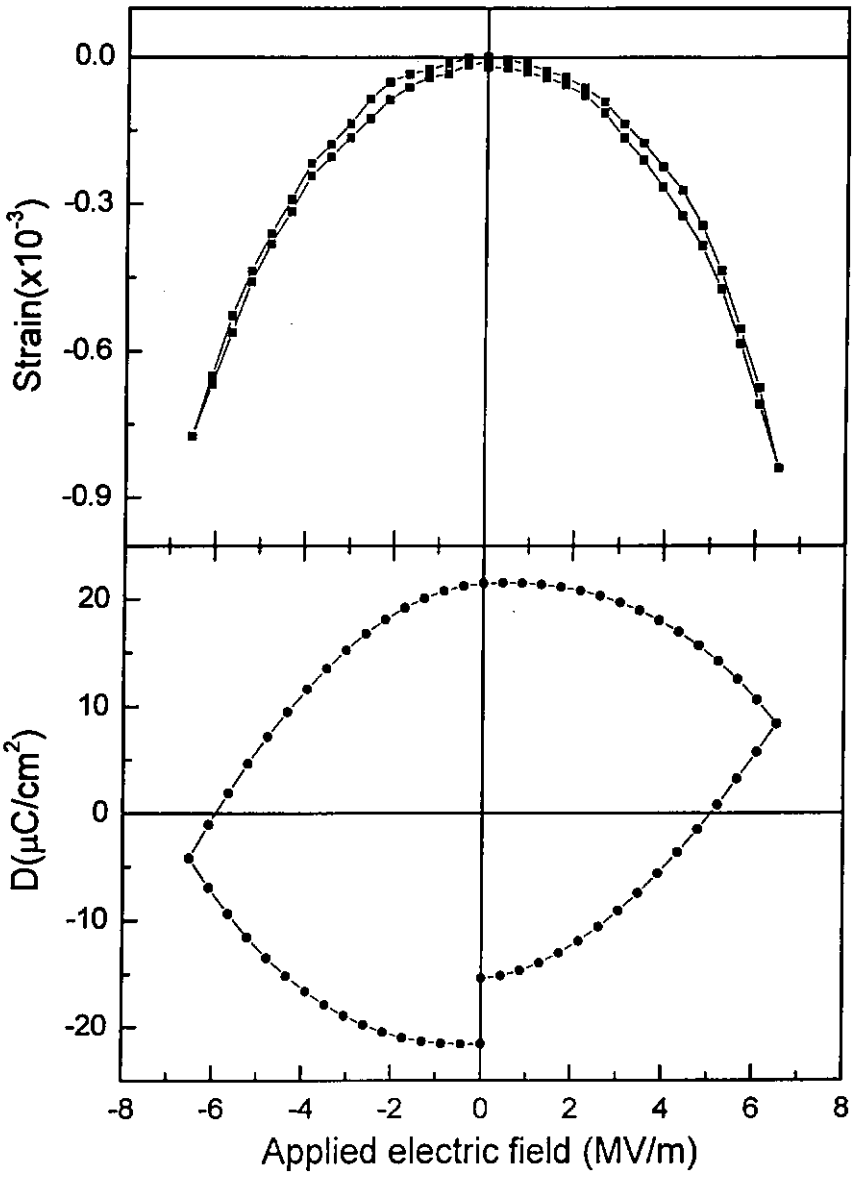

Figure 6.6 Electric field induced strain and instantaneous electric displacement of pure PU under the application of the "stepped" electric field.

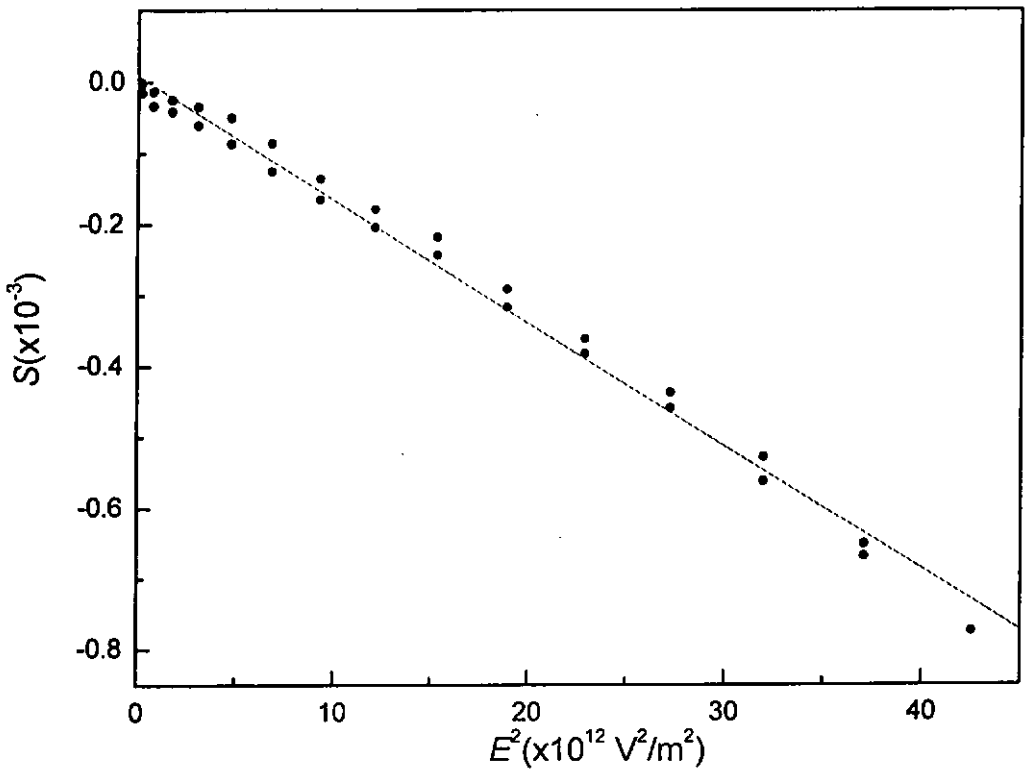

Figure 6.7 Induced strain S of PU against the square of applied electric field E.

In Figure 6.6, we find that the relationship between the induced strain S of PU and the applied electric field E follows a quadratic equation $S = ME^2$ where M is the electrostriction coefficient. A plot of S against E^2, as shown in Figure 6.7, is almost linear. Therefore, M can be obtained from the slope of the best fit straight line. It is about $-1.7\times10^{-17}\ m^2/V^2$.

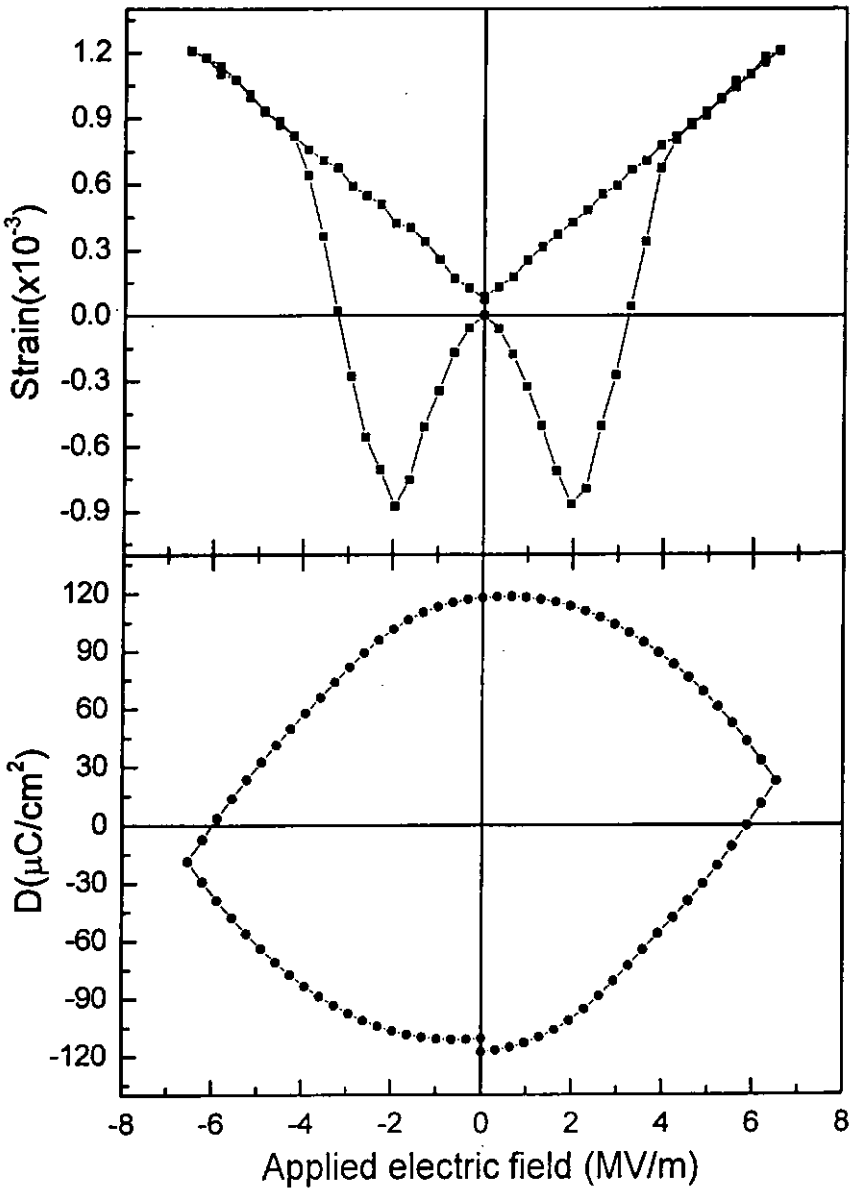

Figure 6.8 Electric field induced strain and instantaneous electric displacement of PZT/PU composite with 30% volume fraction PZT under the application of the "stepped" electric field.

In Figure 6.8, the induced strain of the PZT/PU composite forms a similar hysteresis loop of butterfly shape as the pure PZT under the application of the stepped electric field with 10s time duration for each step. The switching of the induced strain occurs at about +/–2 MV/m and is likely due to the flipping of PZT dipoles in the PU matrix. However, the electric displacement of the composite does not exhibit any sharp change even at the switching electric field, unlike in the case of PZT. On the other hand, as shown in the electric displacement graph of Figure 6.6, the remanent polarization is as large as 118 $\mu C/cm^2$ and the coercive field is equal to 5.8 MV/m which is far beyond the switching field of the induced strain. This electric displacement hysteresis loop is similar to that of pure PU. The oval shape of the hysteresis of both pure PU and the composite may be a result of the high conductivity of the PU. This will be discussed more thoroughly in the following section.

6.3 Current-Electric Field Loops of PZT/PU Composites

The *D-E* loop measurement method is introduced in the previous section. It correlates the polarization change to the electric field induced strain of the pure PZT sample. However, the oval-shaped *D-E* loop of the PZT/PU composite is different from the conventional square-like *D-E* hysteresis loop of pure PZT. For getting more information, the reference capacitor in the *D-E* measurement setup is replaced by a 1 kΩ reference resistor so that the current passing through the circuit can be obtained. Graphs of current-time (*I-t*) and current-electric field (*I-E*) for the pure PZT sample are shown in Figure 6.9. In the *I-t* graph, we see that sharp peaks occur at the instant when each step is applied. The peaks correspond to the charging or discharging currents. In addition, two more significant current peaks are present. These large changes in current correspond to the flipping of PZT dipoles, thus producing the large displacement currents. In the *I-E* graph, it is evident that the large changes of current occur at around +/–0.85 MV/m which is equal to the coercive electric field and also near the switching field of the induced strain of the pure PZT sample.

Similarly, the *I-t* and *I-E* graphs of the pure PU sample and the 30% PZT/PU composite can be obtained under the same experimental conditions; the results are shown in Figures 6.10 and 6.11 respectively. Comparing with the pure PZT, sharp current peaks, due to the charging and discharging processes, also occur at the beginning of each voltage step in the *I-t* curves of pure PU and the PZT/PU composite. However, the current does not drop to zero as in pure PZT. This implies that in addition

to the displacement current there is a conduction current which is dependent on the applied voltage.

As shown in Figure 6.10, the current in the *I-t* curve is partly due to the conduction current of the sample. Similarly, the current in the *I-t* curve of the PZT/PU composite, as shown in Figure 6.11, also includes a conduction current. In addition, there are "hums" at about +/–2 MV/m which correspond to the switching fields in the induced strain measurement. These hums do not occur in Figure 6.10 for the pure PU sample. It is evident that the existence of the hums is manifested by the flipping of the PZT dipoles in the composite. However, the hum area under the *I-t* graph is a small part of the total area. As a result, it produces no significant change in the *D-E* loop of the PZT/PU composite.

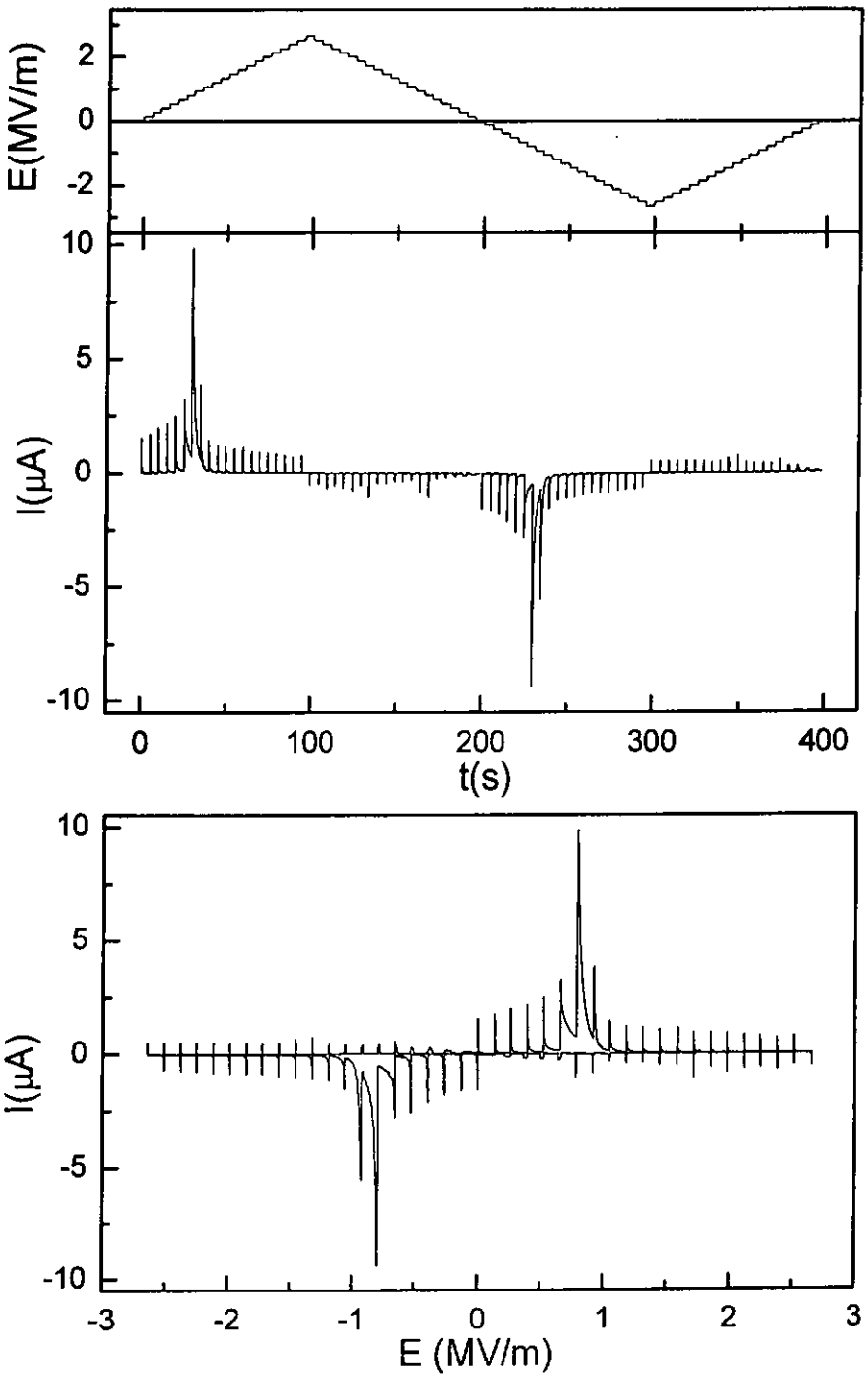

Figure 6.9 *I-t* graph and *I-E* graph of pure PZT under the application of the "stepped" electric field.

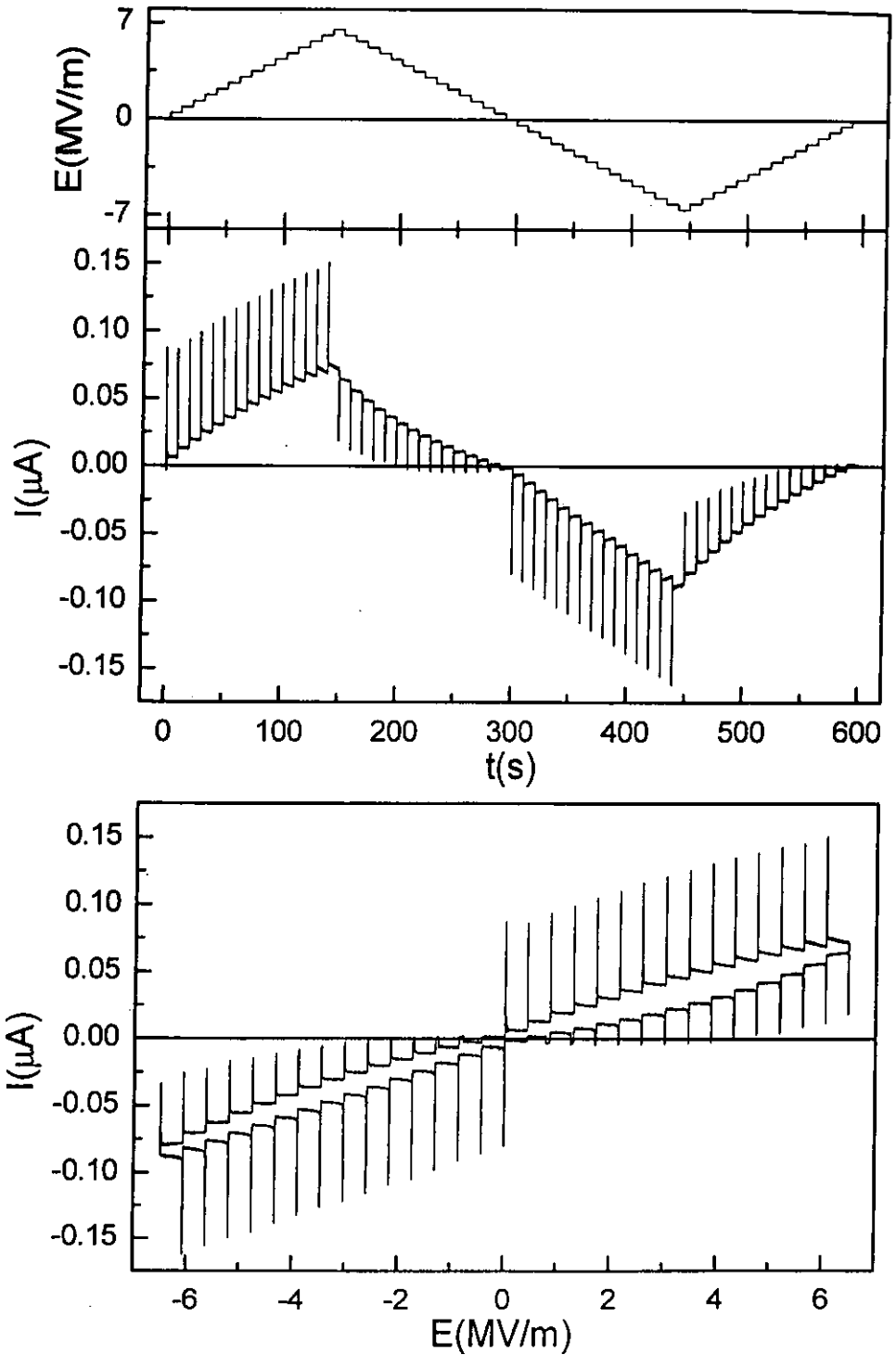

Figure 6.10 *I-t* graph and *I-V* graph of pure PU when under the application of the "stepped" electric field.

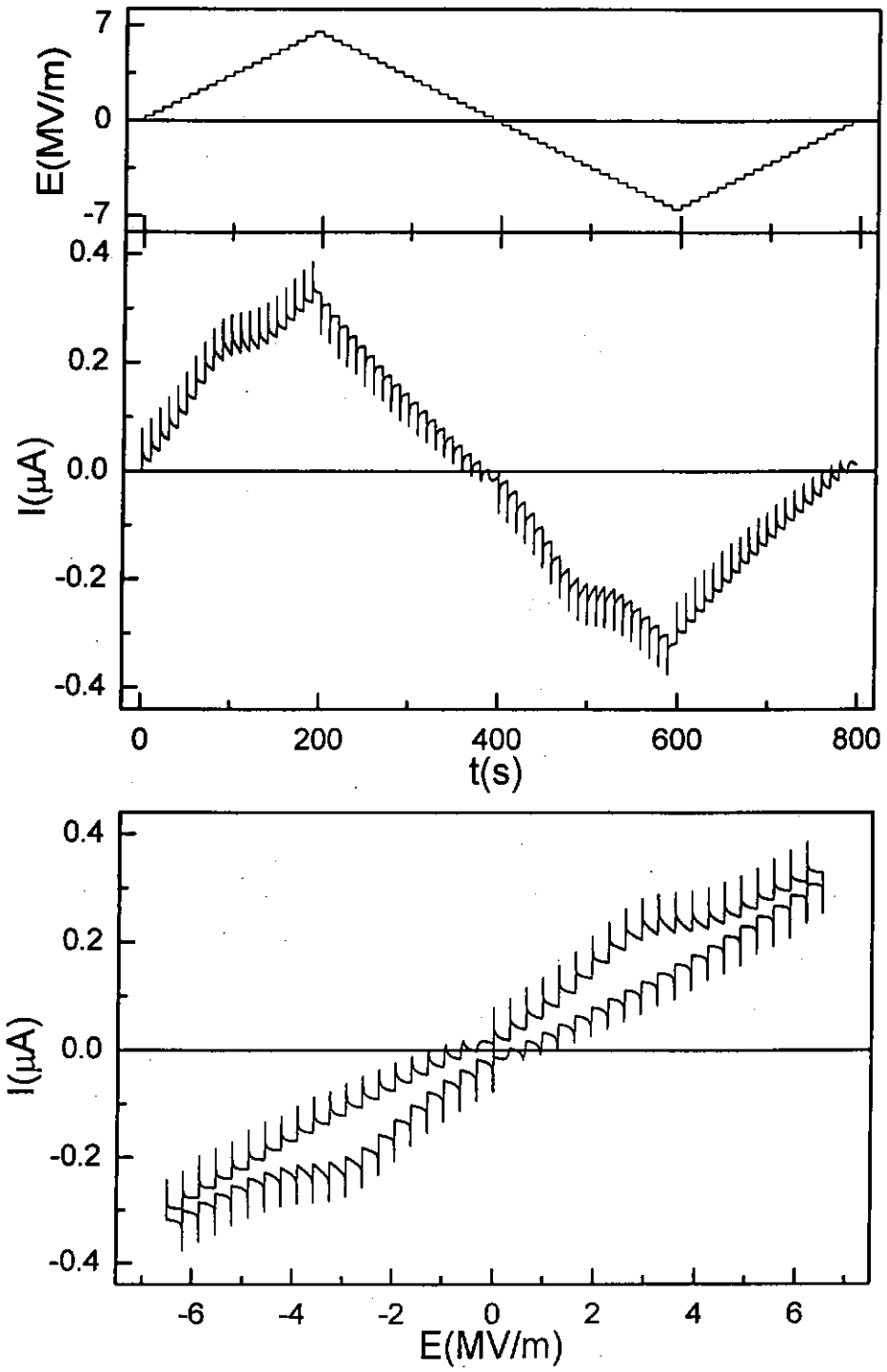

Figure 6.11 *I-t* graph and *I-E* graph of PZT/PU composites with 30% volume fraction of PZT under the application of the "stepped" electric field.

Another interesting feature of the oval *D-E* loops of PU and its composite is the fact that it is an open curve, likely due to conductivity. This behavior also occurs in the bending displacement measurement which will be discussed in Chapter 7.

In summary, we find that the electric displacement measurement does not provide much information for samples which have relatively high conductivities. For example, in this study, the conductivities of the PU and the PZT/PU composites are in the order of 10^{-9} to $10^{-10}\,\Omega^{-1}m^{-1}$ which is about three orders of magnitude higher than that of pure PZT. In addition, the current measurement method is more suitable for observing the relatively small displacement current even though conduction current is present.

6.4 Compliant Electrodes

Metallic electrode clamping is one of the constraints on the piezoelectric properties of electro-active polymers [Wang et al., 1993; Su et al., 1997(a)]. This problem is serious when the elastic compliances of the polymers are much larger than that of the metallic electrodes. For solving this problem, compliant electrodes are used instead of metallic electrodes. In recent years, a variety of materials and techniques have been used to produce compliant electrodes, such as lift-off stenciling techniques for powdered graphite, selective wetting of ionic conductive polymers, spray coating of carbon blacks and fibrils in polymeric binders [Pelrine et al., 1998] and using wrinkled polypyrrole as electrode material [Watanabe et al., 2002].

In this project, carbon black blended in silicone (Dow Corning, 734) was used as the compliant electrode material since it could provide a conductive layer with high compliance. The electric field induced strain of pure PU with the compliant electrodes and gold electrodes were tested and compared.

First of all, a suitable amount of carbon black was blended with silicone uniformly. The mixture was painted on both surfaces of the sample and cured for 24 hours. The thickness of the compliant electrode was about 10 μm while the thickness of the hot pressed PU was 230 μm. The conductivity of the cured carbon black/silicone was $2.5\times10^{-4}\ \Omega^{-1}m^{-1}$, about six orders of magnitude larger than that of pure PU ($10^{-10}\ \Omega^{-1}m^{-1}$).

The electrostriction of pure PU with compliant electrodes and gold electrodes are shown in Figure 6.12 for comparison.

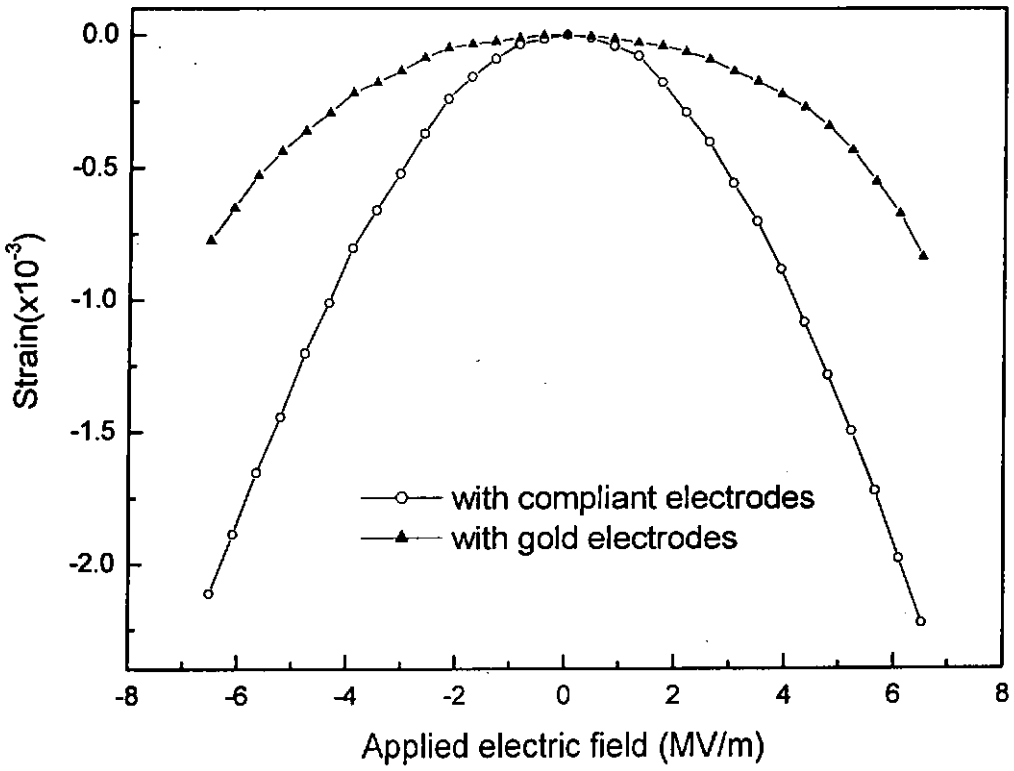

Figure 6.12 Electrostriction of pure PU with compliant electrodes and gold electrodes.

From Figure 6.12, we find that there is a great improvement in electrostriction with compliant electrodes. At high electric field, the induced strain of the PU sample with compliant electrodes is about three times larger than that with gold electrodes. A plot of

the induced strain S against the square of the applied electric field E is shown in Figure 6.13. The electrostrictive coefficients determined with compliant electrodes and gold electrodes are $-5.3\times10^{-17}\ m^2/V^2$ and $-1.7\times10^{-17}\ m^2/V^2$ respectively. These results, on the one hand verify the existence of clamping effect, and on the other hand show that the carbon black/silicone composite can be used as conductive material for compliant electrode.

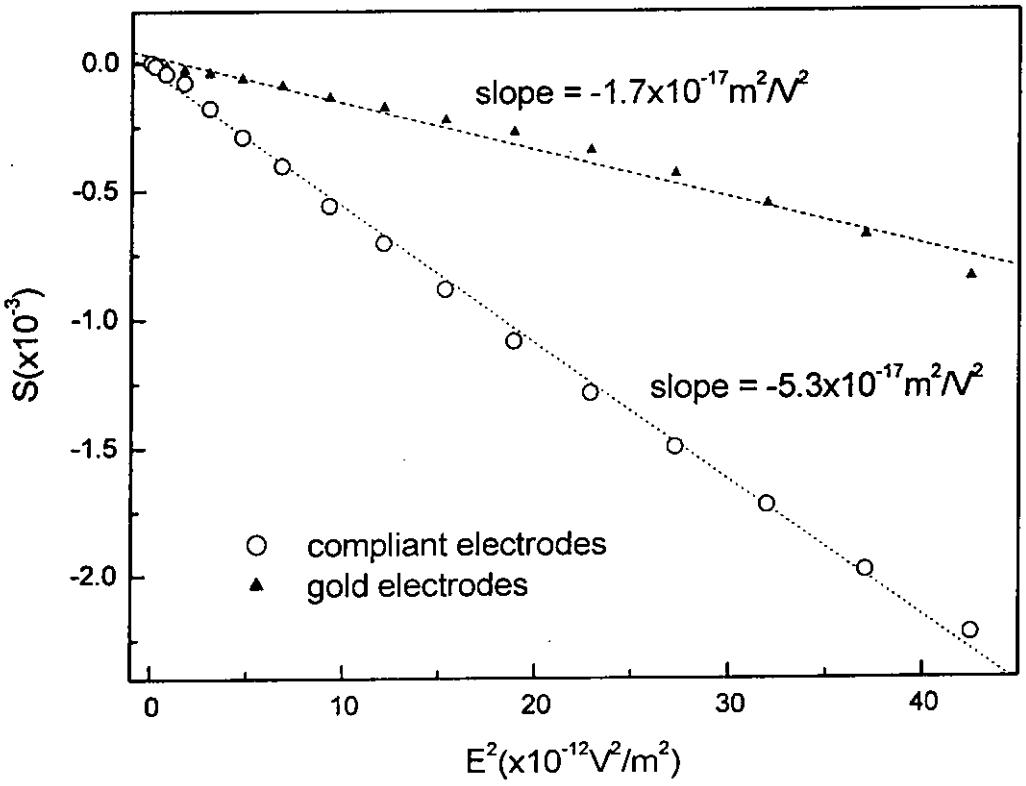

Figure 6.13 Induced strain S of PU with compliant electrodes and gold electrodes against the square of applied electric field E.

Chapter 7

Bending Actuation of PU and PZT/PU Composites

7.1 Bending Actuation of Polyurethane Film

It has been found that a strip of polyurethane film clamped on a fixture at one end and free at the other bends to one side if a voltage is applied across its surface electrodes. Both the magnitude and direction of bending depend on the polarity and the time duration of the applied field. Some thoughts about of the bending mechanism of the PU film are also discussed in this chapter.

7.1.1 Sample Preparation and Measurement Setup

Thermoplastic polyurethane pellets were dried for 24 hours and then hot pressed at 160°C. The films obtained were naturally cooled to room temperature in the press. Their thicknesses were about 100 μm to 130 μm and were cut into rectangular shape. The films were coated with 5 × 30 mm (for electric field dependence measurement) and 5 × 25 mm (for time dependence measurement) gold electrodes on both surfaces by using ion sputtering. To remove internal stresses and charges during fabrication, all films were annealed at 60°C under short circuit condition for 10 hours.

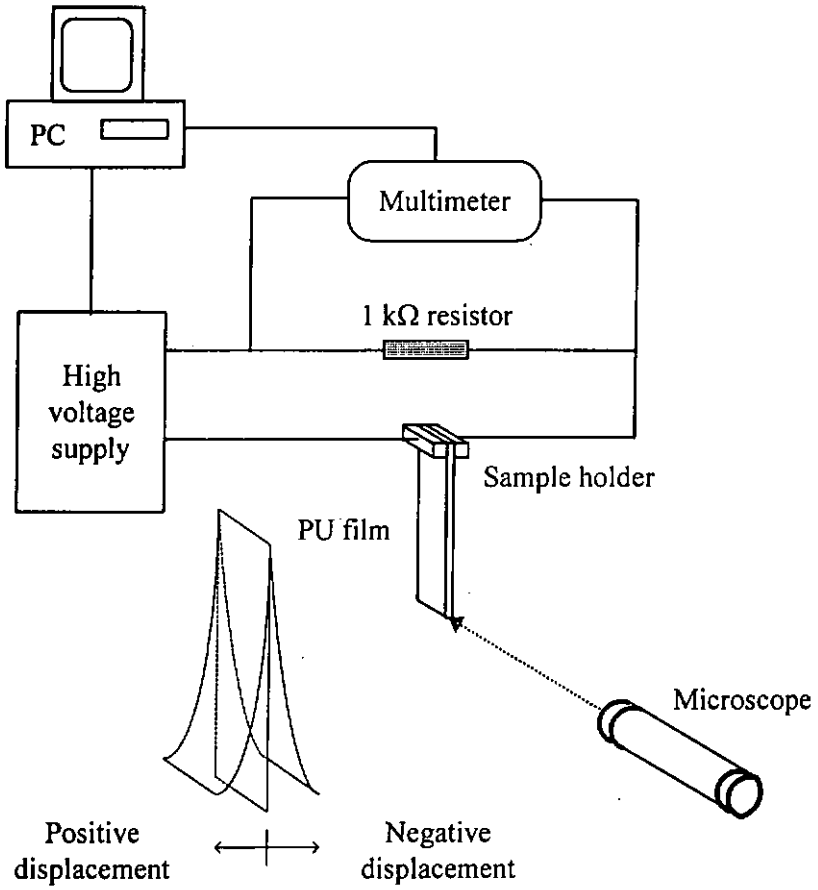

Figure 7.1 Experimental setup for electric field induced bending measurement

Figure 7.1 shows the experimental setup for electric field induced bending measurement. The rectangular film sample is vertically suspended in air and one end of the film was fixed to the sample holder. While a dc voltage was applied, the horizontal displacement of the film's free end (bending displacement) was measured through a microscope with a built-in reticle. The measurement resolution was about 25 μm. On the other hand, the current was measured by monitoring the voltage across a 1 kΩ resistor in series with the sample by a multimeter (HP34401A).

7.1.2 Electric Field Dependence

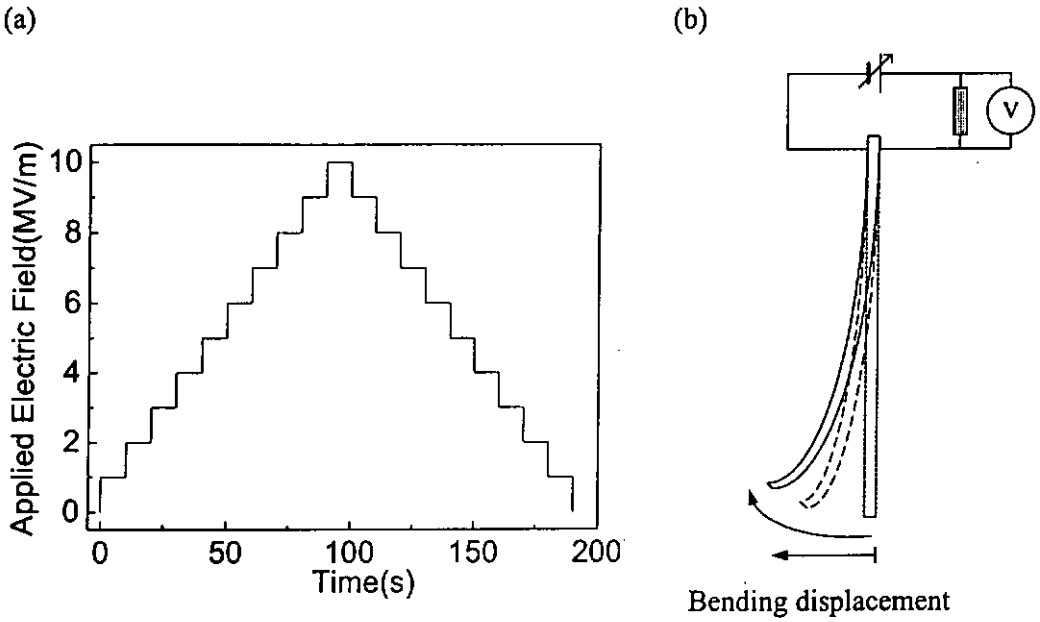

Figure 7.2 (a) Time profile of the "stepped" E-field and **(b)** simplified electric circuit in the PU actuator performance testing.

A "stepped" triangular voltage variation, as shown in Figure 7.2(a), was applied to a 100 μm rectangular shaped PU film as shown as Figure 7.2 (b). The corresponding electric field was increased from zero to 10 M/m and then decreased back to zero in steps of 1 MV/m. The step duration was 10s; in other words, a complete "cycle" lasted for 200s.

The displacement of the free end was used to represent the bending magnitude. As the field acted on the sample, the film bent to the cathode side. Bending magnitude and the corresponding currents for five "cycles" were measured. For clarity, only the 1st, 3rd

and 5th cycle results plotted against applied field are shown in Figures 7.3 (a) and (b). From the graphs, we see that both the bending displacement and current increase with increase in applied electric field. In particular, the bending displacement almost follows a quadratic relation with field. This is verified by the linear relation of the bending magnitude with squared electric field as shown in Figure 7.4. On the other hand, both the bending magnitude and current decreases in subsequent cycles. This phenomenon will be clarified after the description of the time dependence of bending.

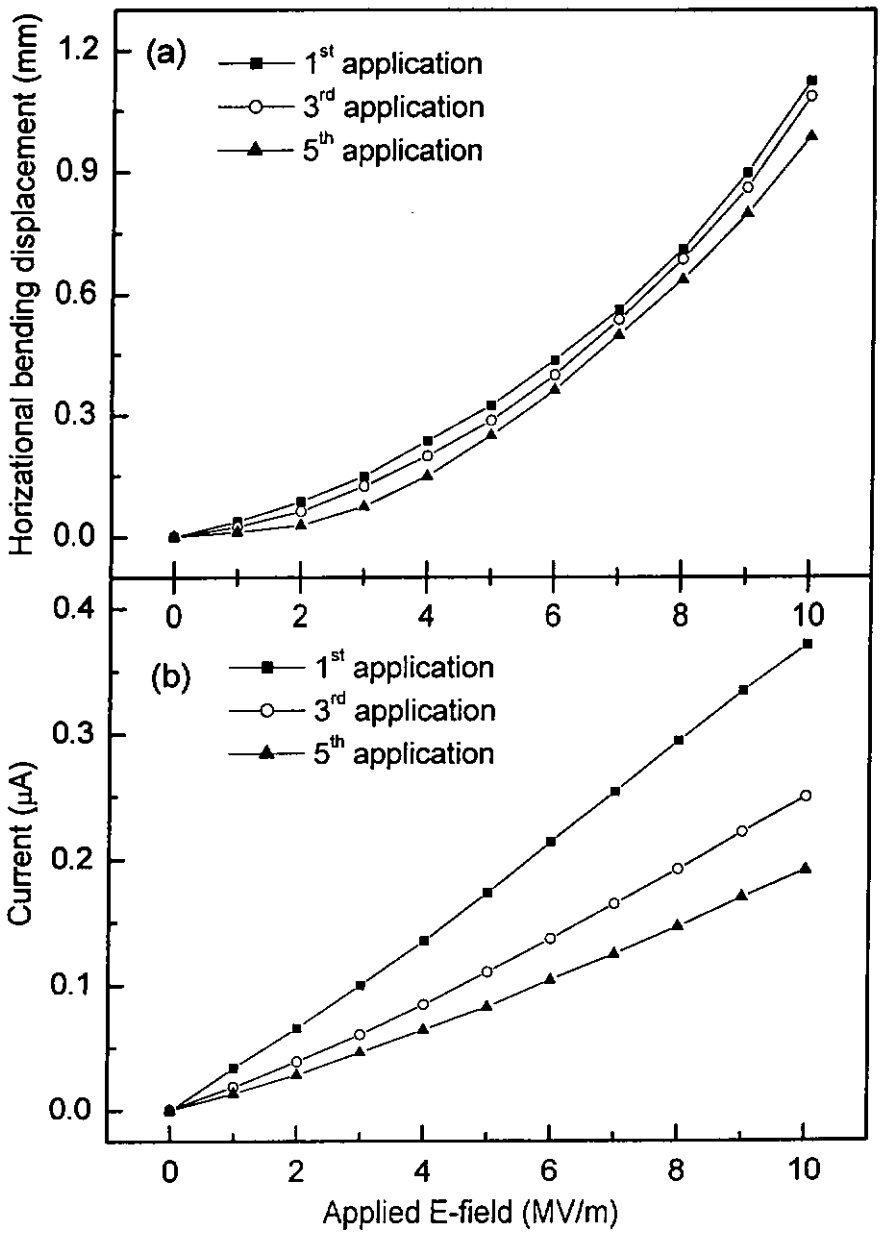

Figure 7.3 (a) Bending displacement of PU actuator and **(b)** current in the circuit under the "stepped" triangular field.

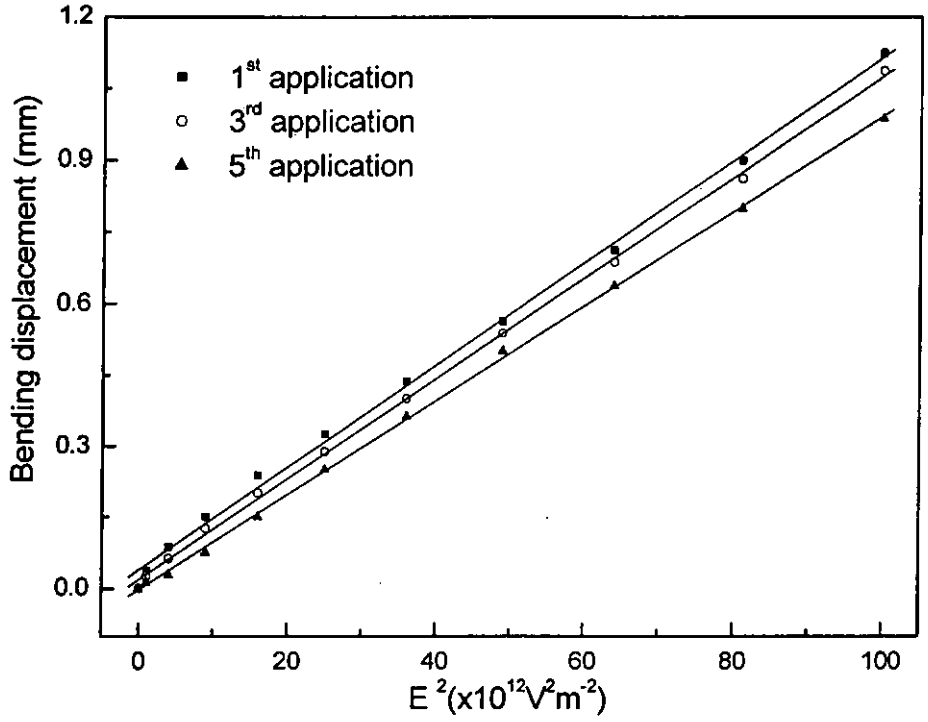

Figure 7.4 Bending displacement of PU versus square of electric field.

7.1.3 Time Dependence

A series of on and off dc voltage of 1200V was applied to a 130 μm thick PU film and the duration of the "on" state was 6 minutes and that of the "off" state 30 seconds. An "on" state followed by an "off" state constituted a "cycle". The bending displacement of the free end of the film was measured simultaneously. The whole time profile of the applied electric field *E* and the bending displacement are shown in Figures 7.5(a) and (b) respectively. In the first cycle the film bent toward the cathode side. It

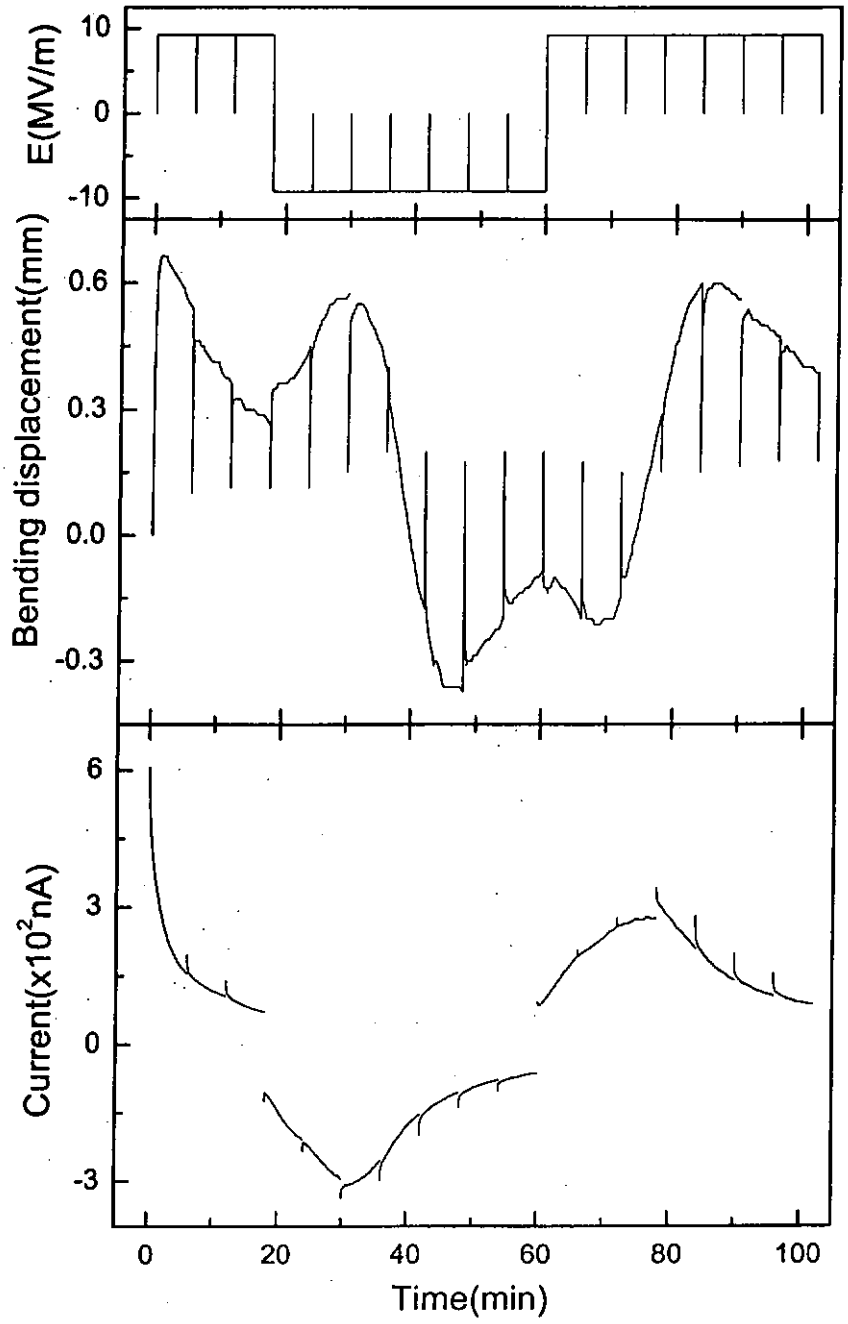

Figure 7.5 (a) Electric field-time profile; time dependence of **(b)** bending displacement and **(c)** current of PU.

reached a maximum position as the field was switched on and it gradually moved back from the maximum position at constant field. It returned to the neutral position as the field was switched off. In the subsequent cycles, the film was only bent to the position at which the field switched off in the previous cycle. It looks like that the bending has a memory effect. When the polarity of the electric field was reversed, the film still bent to the same side (at this point it was the anode side) and the bending displacement increased in the subsequent two cycles. After two cycles, the bending displacement started to decrease and then the film bent rapidly toward the cathode side. In subsequent cycles the bending displacement decreased. Similar bending behavior but in opposite direction in the following cycles was observed. Figure 7.6 shows schematically the bending behavior of the film in a reversing field sequence.

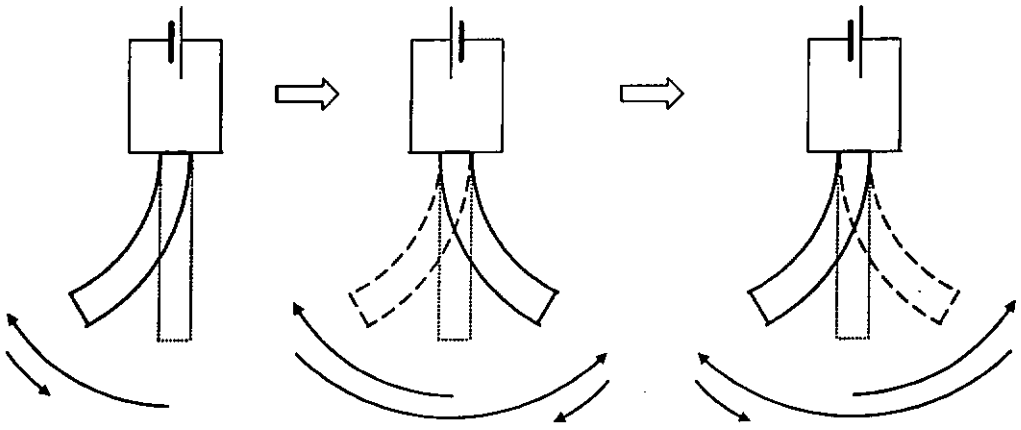

Figure 7.6 The bending sequence of PU film under the reversion of the polarity of applied field.

7.1.3.1 The Charging and Discharging Currents

The charging and discharging currents were monitored by the potential drop across a resistor in series with the sample during the application of electric field in the bending measurement. The results are shown in Figure 7.5(c). Comparing with the bending pattern shown in Figures 7.5(b) and (c), it can be seen that the currents are closely related to the bending behavior. Similarly to the bending behavior, the currents passing through the sample exhibit a memory effect. In subsequent applied voltage cycles, the current can only reach the magnitude at switch off in the previous cycle. Another interesting feature shown in the current diagram is the change from an increasing current to a decreasing current at the 5^{th} to 6^{th} and 12^{th} to 13^{th} cycles. The bending directions also changed simultaneously although the applied voltage remained in the same polarity in these cycles.

7.1.3.2 A Thinking of Bending Mechanism of PU

We believe that the bending behavior of the PU film is an electrostrictive effect as a result of inhomogeneous distributed charges in the film. The inhomogeneous charge distribution is likely caused by charge injection from the external circuit. The externally applied electric field on the one hand injects charges into the film, and on the other hand produces an asymmetric internal field along the thickness of the film as a result of the inhomogeneous charge distribution.

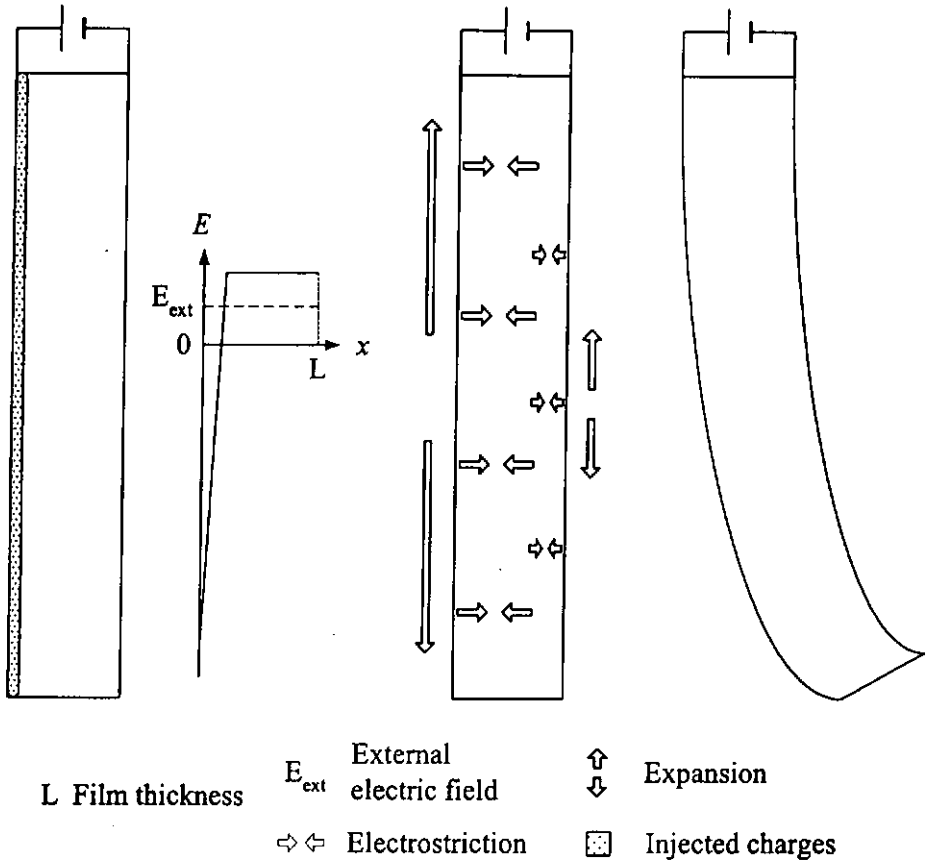

Figure 7.7 Schematic diagram of the bending of PU under application of electric field.

At the moment the electric field is applied to the sample as shown in Figure 7.7, charges are injected at the anode side, producing a thin layer of charge near the film surface to provide a larger absolute value of electric field at the anode. The higher absolute electric field at the anode side of the sample perpendicular to the film results in a larger compressive electrostriction which is proportional to the square of electric field. Since compression of the elastic PU in the thickness direction will extend the lateral dimension of the film, a higher compression and therefore extension at the anode side

produces a bending toward the cathode. In other words, film bending is explained as a result of the asymmetric electrostriction along the film thickness.

After a period of time of the field application, the injected charges driven by the electric field may drift inward. A mild gradient of the charge distribution along the film thickness is developed, thus reduces the absolute electric field as well as electrostriction difference between the two sides of the film. As a result, the bending decreases. When the external electric field is switched off, the bent film restores the normal shape because the electrostriction due to the external electric field vanishes. However, the charge gradient still remains in the film, therefore the film bends to the previous position as the field is switched on again. On the other hand, this also explains that a reversed polarity does not change the film's bending direction, since electrostriction does not depend on the field direction. After the reversion of the polarity of the electric field, the charge gradient begins to develop on the new anode side of the film and after a certain period of time the film bends to the cathode side again. The whole bending process is repeated as the field is reversed again, as shown in Figure 7.5(b).

The bending behavior of polyurethane films is here suggested as a direct result of the charge distribution in the film and the applied electric field. The film does not exhibit observable bending without the application of electric field even when a charge gradient exists in the film. This seems to rule out a plausible alternative mechanism of charge repulsion leading to bending.

7.1.4. Electrode Clamping Effect on Bending

Another factor affecting the performance of the bending is the electrode clamping effect which is similar to the clamping effect on electrostriction. Figure 7.8 shows the bending displacement of two identical samples of different gold electrode thicknesses. It is obvious that the thicker electrode (100 nm) will produce larger clamping and thus smaller bending than the thinner electrode of thickness about 20nm.

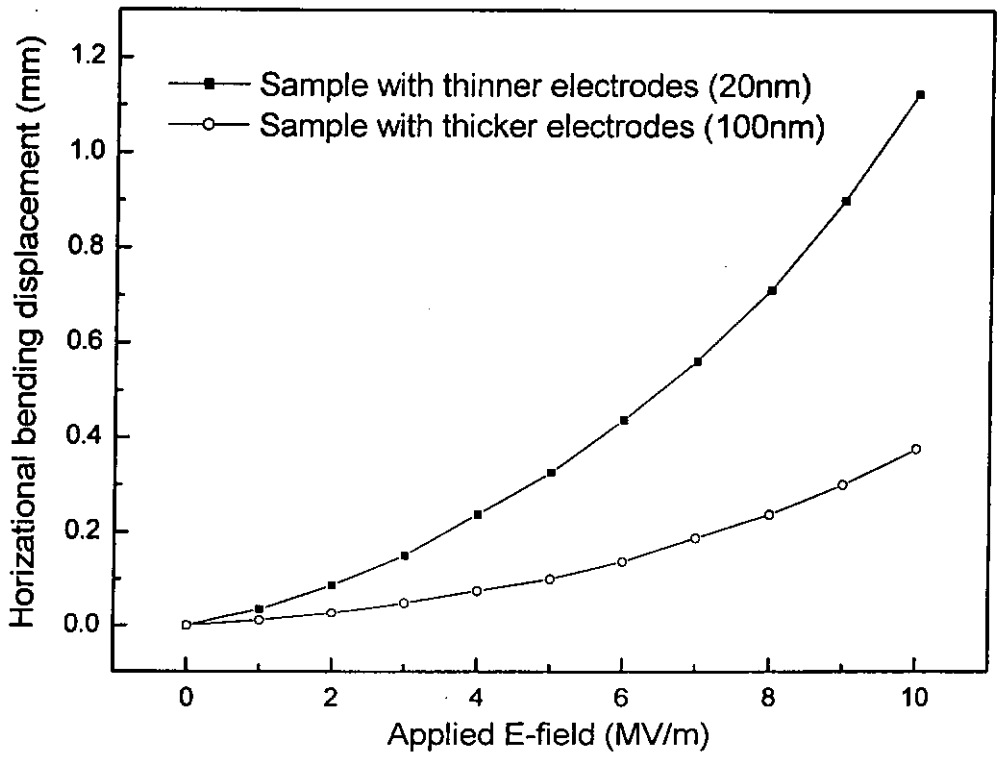

Figure 7.8 Bending displacement of PU films of different electrode thicknesses.

7.2 Bending Actuation of Bimorph

In this section, the bending behaviors of bimorphs consisting of a combination of PU film bonded to a PZT/PU composite film will be discussed. Bimorphs considered here are of two types; active-active type and active-passive type. Both layers in the active-active bimorph will be activated when functioning while only one layer in the active-passive bimorph will be activated. The bending mechanism, performance and limitations of the bimorph bending actuators will be discussed in detail in the following sections.

7.2.1 Fabrications of Bimorph

PU films and PZT/PU composite films with 30% volume fraction were used to construct the PU-PZT/PU composite bimorph bending actuators, the other combination was the composite- composite actuators. All of the films were cut into 6 × 31 mm and coated with 5 × 30 mm gold electrodes (~20 nm thick) on both surfaces. Silicone (Dow Corning 734) was applied for bonding the two films. The structures of the active-passive type and active-active type bimorph bending actuators are shown in Figure 7.9.

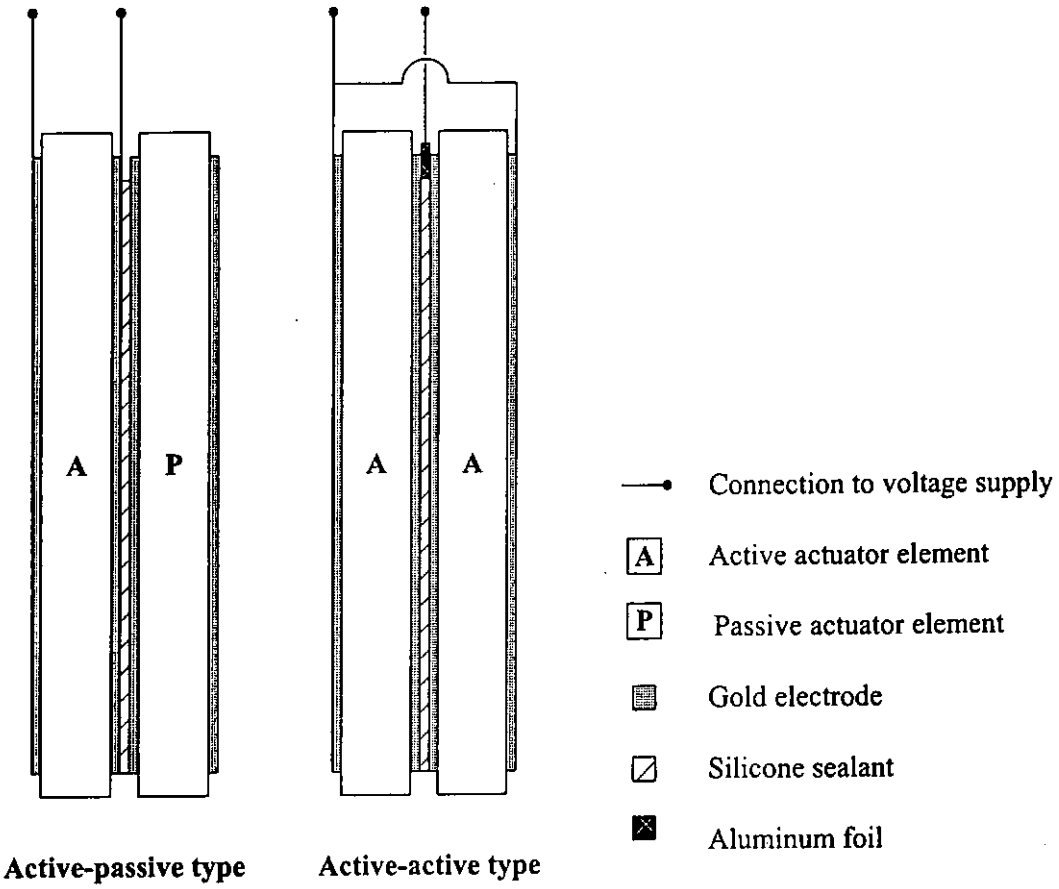

Figure 7.9 Structures of the active-passive type and active-active type bimorph bending actuators.

7.2.2 Bending Performance

To understand the different bending behaviors of the bimorph bending actuators, it is necessary to consider the electrostriction of PU and PZT/PU composite under the application of electric field. Figure 7.10 shows the bending mechanisms of an active-passive bimorph bending actuator with PZT/PU composite as the active layer.

The actuator will bend toward the active layer side when the applied electric field direction is opposite to the polarization of the PZT inclusions. On the other hand, the actuator will bend toward the passive layer side when the applied electric field is in the same direction of the polarization.

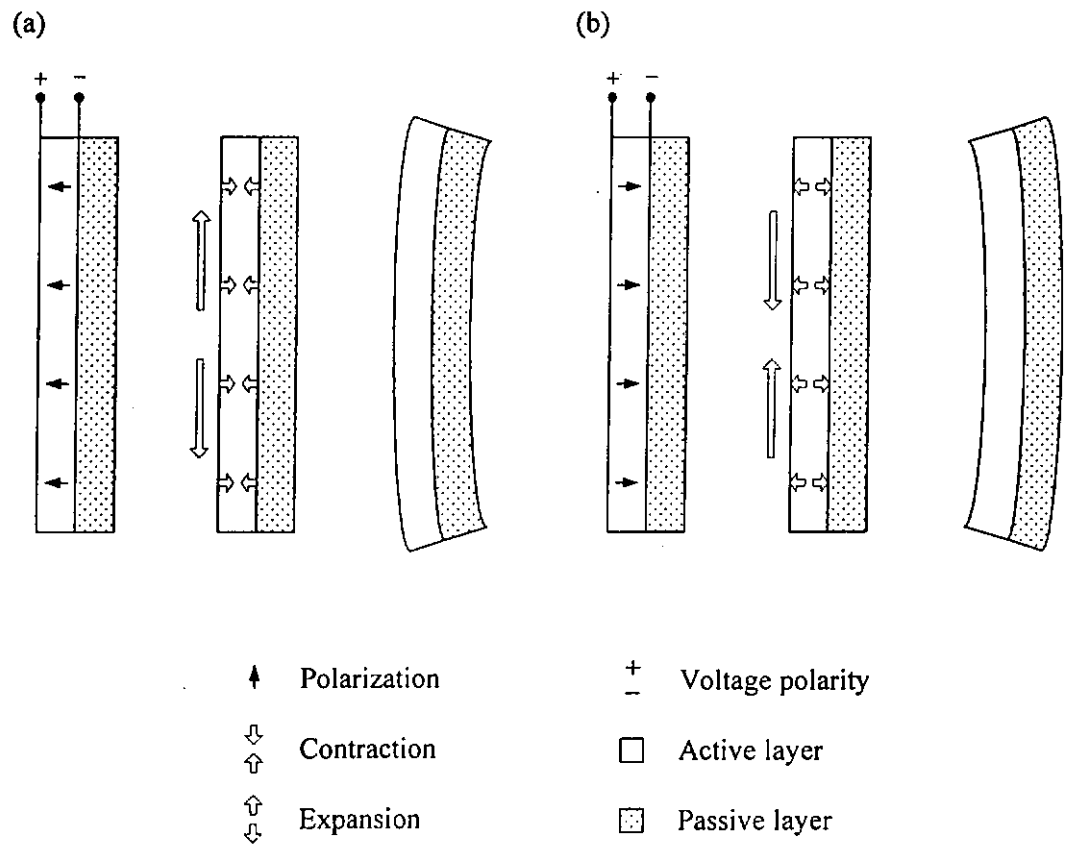

Figure 7.10 Bending mechanism of the active-passive bimorph bending actuator with PZT/PU composite as active layer under application of electric field **(a)** anti-parallel and **(b)** parallel to the polarization.

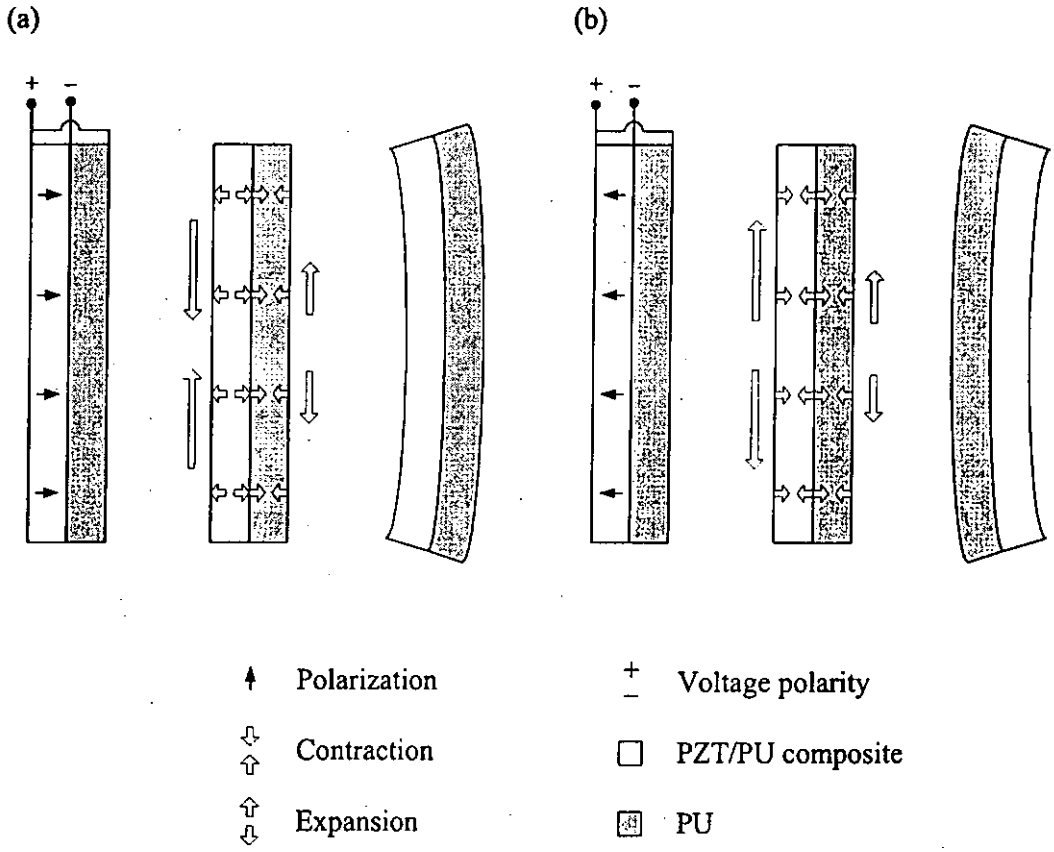

Figure 7.11 Bending mechanism of the active-active bimorph bending actuator with PU and PZT/PU composite as active layer under application of electric filed **(a)** parallel and **(b)** anti-parallel to the polarization.

Figure 7.11 shows the bending mechanism of an active-active bimorph bending actuator. One of the active layers is PU and the other is PZT/PU composites with 30% volume fraction of PZT. Since electrostriction of the PU layer is independent of the direction of the electric field, it will contract whenever there is a field. As a result, an enhancement of the bending displacement occurs when the applied electric field is in

the same direction of the polarization. The bending displacement will be reduced by the electrostriction of the PU layer when the applied electric field is anti-parallel to the direction of the polarization.

Table 7.1 Information of different configurations of the bimorph bending actuators.

Configuration	Active layer (thickness)	Active layer/ Passive layer (thickness)	Operating mode
I(a)	Composite (133 μm)	PU(120 μm)	A-A
I(b)	Composite (133 μm)	PU(120 μm)	A-P
I(c)	PU(120 μm)	Composite (133 μm)	A-P
II	Composite (184 μm)	Composite (184 μm)	A-P
III(a)	Composite (150 μm)	Composite (120 μm)	A-P
III(b)	Composite (120 μm)	Composite (150 μm)	A-P
IV	Composite (130 μm)	Composite (130 μm)	A-P

*Composite = PZT/PU composite with 30% volume fraction of PZT

*A-A = Active-active bimorph operation mode

*A-P = Active-passive bimorph operation mode

Following the bending mechanisms as described in the previous paragraphs, four configurations of bimorph bending actuators were constructed. Table 7.1 summarizes all the combinations. Some represent different operation modes. The bending performances of these actuators were tested using the setup shown as Figure 7.1. The

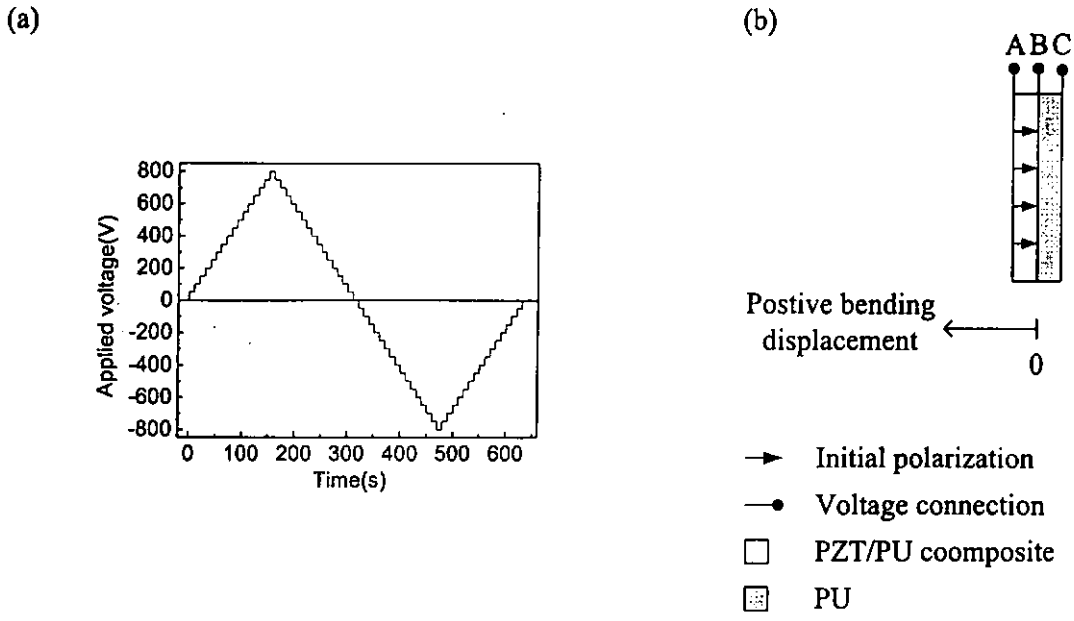

Figure 7.12 (a) Time profile of the application of "stepped" triangular wave-like electric field. **(b)** Initial status of the configuration I bimorph and the definition of the positive bending displacement.

time profile of the application of a "stepped" triangular wave-like electric field in the testing of configuration I bimorph is shown in Figure 7.12(a). The voltage step was 50V, the time duration of each step was 10s and the maximum voltage was 800V. In addition, Figure 7.12(b) shows the initial status of the polarization and the definition of the positive bending displacement of the testing. In testing the configuration I(a), the connection A and C were shorted and the voltage was applied to A and B such that the electric field was anti-parallel to the polarization of the PZT/PU composite at the start of the measurement. The connection of the testing of the configuration I(b) is similar to that of I(a) except C was shorted to B so that the electric field was only applied across

the composite. Similarly, in testing the configuration I(c), the electric field was only applied across the PU film (B and C) by shorting A and B. The testing results are shown as Figure 7.13.

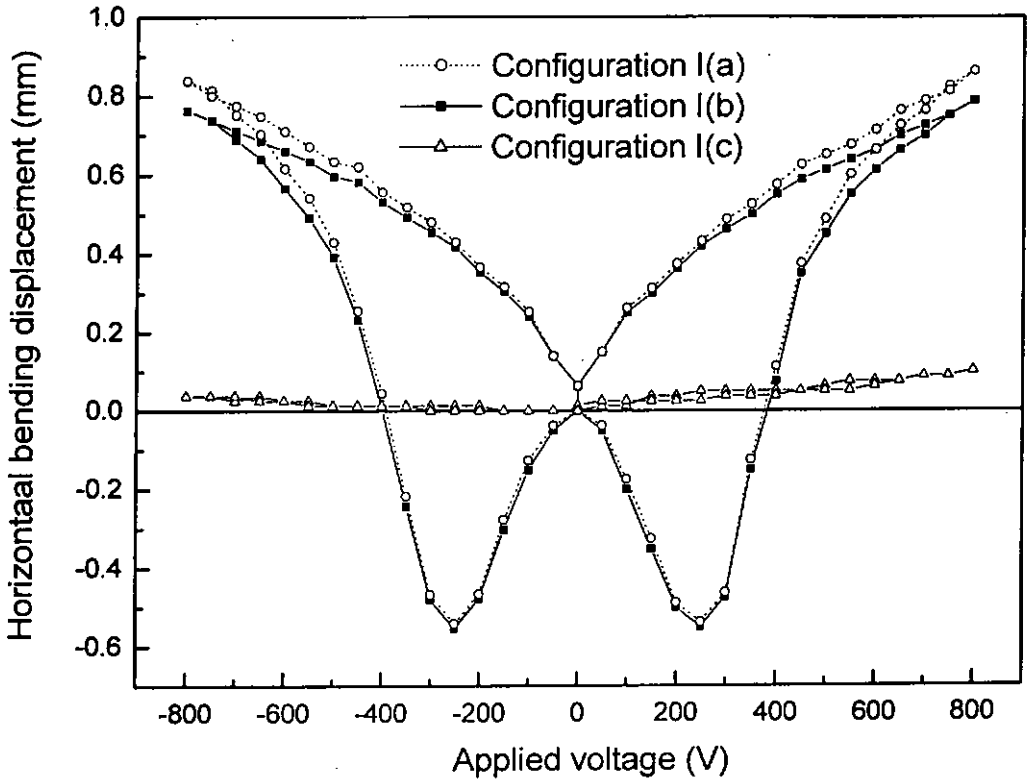

Figure 7.13 Horizontal bending displacement against applied voltage in three different operation modes of the configuration I bimorph bending actuator.

In figure 7.13, we see that the bending displacement of the configuration I(a) and I(b) formed a hysteresis loop in butterfly shape. The hysteresis loop was mainly due to the electrostriction behavior of PZT under the application of electric field which can be

explained from the schematic diagram as shown in Figures 7.10 and 7.11. In addition, a switching of bending displacement occurs at about +/–250V when the applied electric field is anti-parallel to the polarization. This switching is due to the flipping of PZT dipoles and has been verified from the *I-V* graph shown in Figure 7.14.

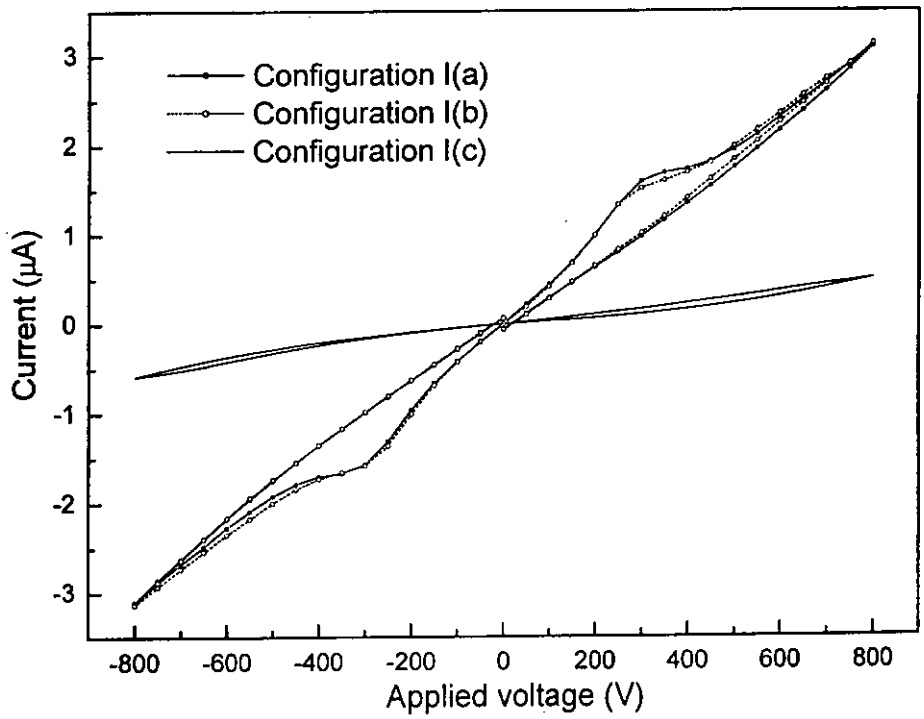

Figure 7.14 Graph of current against applied voltage in the bending displacement experiment of the configuration I bimorph bending actuators.

The hums in Figure 7.14 are the displacement current induced by the flipping of PZT dipoles in the PZT/PU composite. The relation between the flipping of PZT dipoles and the displacement current is already discussed in Chapter 6. On the other hand,

comparing the bending results of the configurations I(b) and I(c), we can see that the deflection of the PU was much smaller than that of the PZT/PU composite especially at low fields. Since the PZT/PU composite was stiffer compared with pure PU, PU when clamped by the PZT/PU composite had difficulty to drive a large deflection. However, there was an enhancement of bending displacement from PU in the configuration I(a) when the electric filed was high enough.

From the practical point of view, the PZT/PU composite in the bimorph system can provide a hysteresis bending behavior. In other words, the bimorph bending actuator can provide a bi-directional movement starting from neutral position when a bipolar voltage is applied. Because of the risk of depolarization, limits of the driving voltages have to be observed strictly.

The configurations II to IV were also tested using the same setup. All of them were tested in the active-passive mode with only the positive voltage ramp (Figure 7.2(a)) applied and the electric field was in the same direction as the polarization of the PZT inclusions. As expected, all actuators bent to the cathode side. The bending displacements are shown in Figure 7.15.

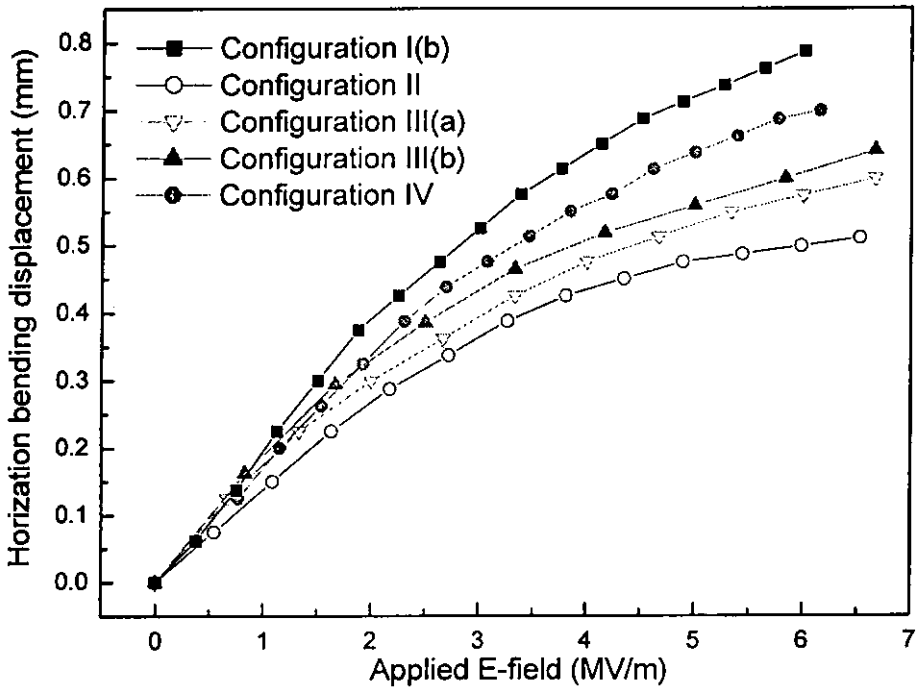

Figure 7.15 Bending displacement of bimorph bending actuators in different configurations.

Figure 7.15 shows that the bending performance of the configuration I(b) is the best because the stiffness of the PU passive layer is smaller than that in the other configurations. Comparing the configurations II to IV, a better performance can be obtained when the thicknesses of the active and passive layers are smaller.

A "symmetric" operation mode of a bi-directional bimorph bending actuator is illustrated in Figure 7.16. There is no risk of depolarizing the PZT inclusions in this operation mode because the applied electric field is always in the same direction of the

polarization of the PZT. Therefore, a symmetric and stable bi-directional bimorph bending actuator can be constructed when the thicknesses of the two active PZT/PU composite layers are equal. The testing results of a bi-directional bimorph bending actuator with thickness 130 μm for each layer are shown in Figure 7.17.

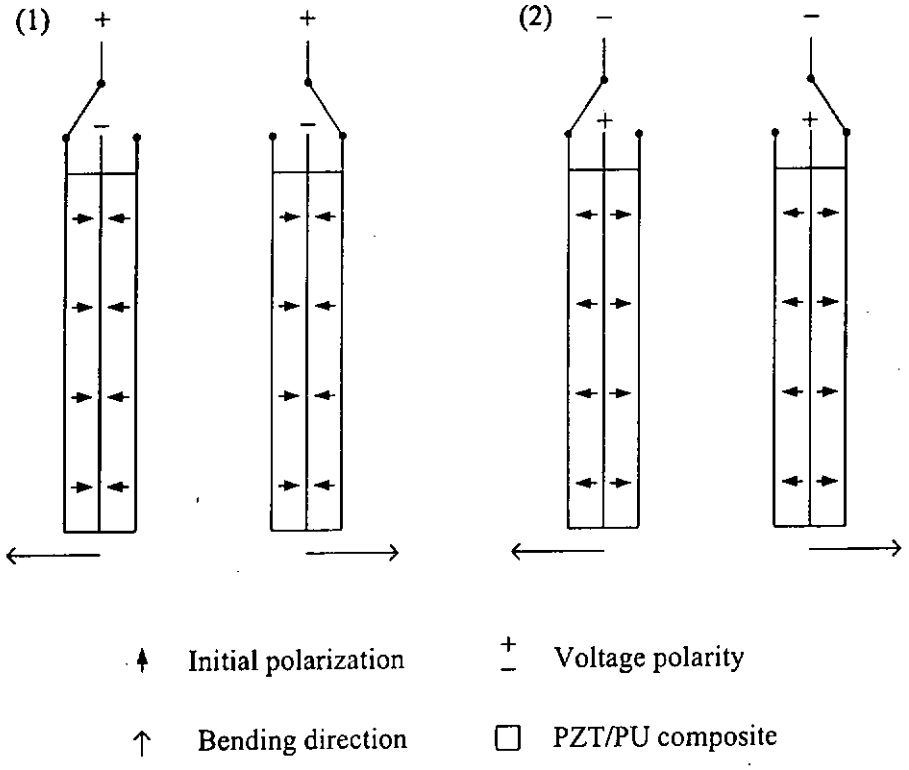

Figure 7.16 Operation status of the "symmetric" mode of the bi-directional bimorph bending actuator.

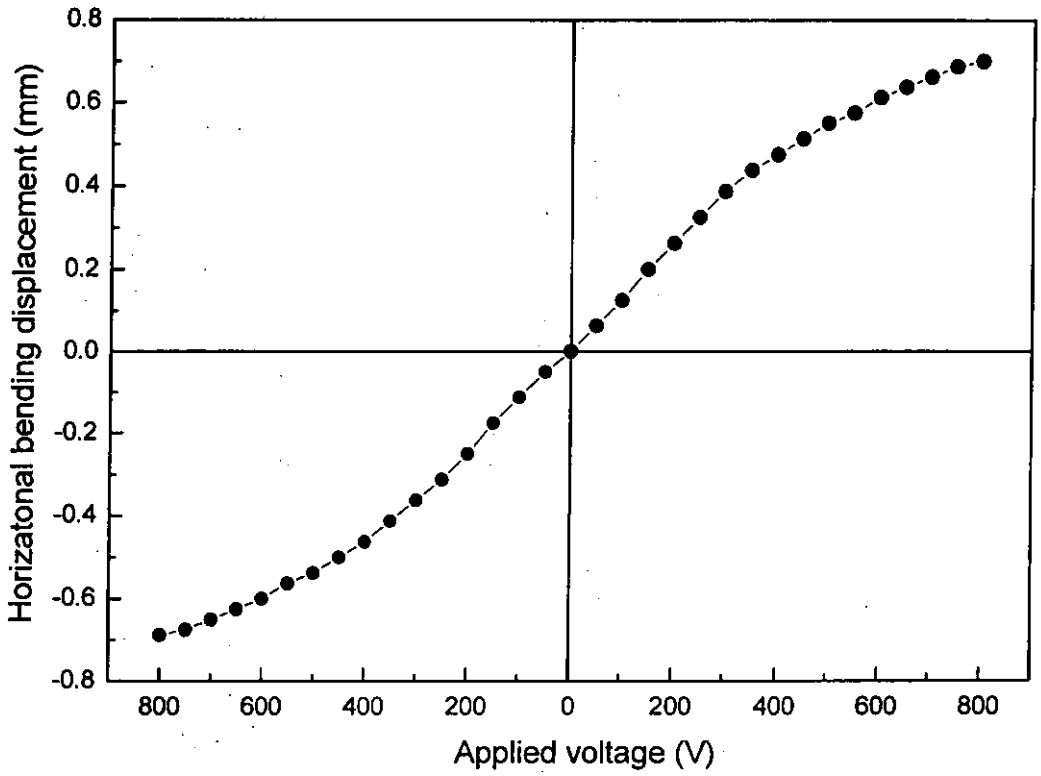

Figure 7.17 Bending displacement of the bi-directional bimorph bending actuator (each layer ~130 μm) under the application of electric field.

7.3 Summary of the Bending Performance of the Bending Actuators

Table 7.2 summarizes the bending performance of the bending actuators so far studied. For unidirectional bending actuation, a single PU film has the advantage of a faster response. The PU-PZT/PU composite bimorph on the other hand has higher stability although the response time is longer.

For bi-directional actuation, the bending displacement of the PU-PZT/PU composite bimorph, operated with electric field in the same direction as polarization, is large compared with the "symmetric" bimorph of PZT/PU composite layers. However, the bending displacement of the PU-PZT/PU composite bimorph, operated with electric field anti-parallel to polarization is limited because smaller fields must be used for fear of depolarizing the PZT in the composite. Thus the "symmetric" bimorph of PZT/PU composites should be chosen for bi-directional bending actuation.

Table 7.2 Summary of the bending performance of the bending actuators.

Bending actuator type	Single film	Bimorph	Bimorph	Bimorph
Element(s) of actuator	PU	PU& comp	PU& comp	comp& comp
Voltage driving type	DC	AC	DC	DC
Operation mode		A-A	A-A	A-P
Bending direction	Cathode	Both	Cathode	Both
Response time	Almost instant (<0.5s)	1 to 2s	1 to 2s	1 to 2s
Limitation(s)	One direction bending	Risk of depolarization Slower response	Slower response	Slower response

*comp = PZT/PU composite with 30% volume fraction of PZT

*A-A = Active-active bimorph operation mode

*A-P = Active-passive bimorph operation mode

Chapter 8

Conclusions and Suggestions for Future Work

8.1 Conclusions

0-3 composites of PZT/PU with 2, 5, 13, 18, 26 and 30% volume fractions of PZT were prepared by extrusion. Samples of pure PU and PZT/PU composites were subsequently hot pressed in thin film form. Microstructure study by SEM showed that PZT were uniformly dispersed in the PU matrix, and the ceramic particles exhibited clear ferroelectric crystal structures under XRD.

The dielectric permittivities and losses of the dried PZT/PU composites were measured at 1 kHz. Both the permittivities and losses were found to increase as the PZT content increased. They were also well fitted by the Bruggeman model. The pyroelectric coefficients of the samples were measured by the ac method. It almost increased linearly with the volume fraction of PZT. The pyroelectric coefficient of the composite with 30% volume fraction of PZT was about 90 $\mu C/m^2K$, which was much larger than the value calculated from standard formulas. A new simple model based on the permittivities and the conductivities of PZT and PU was constructed, giving good agreement with the experimental values of the pyroelectric coefficients of the composites.

As expected, the specific heat capacities of the PZT/PU composites decreased with increasing PZT content. Both the thermal diffusivities and thermal conductivities increased with increasing PZT content. Different figures of merit (FOM) of the composites were calculated. The highest voltage FOM (200×10^{-3} m^2/C) was obtained for the composite of 26% PZT. It was much higher than that of PZT (7.1×10^{-3} m^2/C). On the other hand, the detectivity FOM of the composite of 30% ceramic was 153×10^{-7} $Pa^{-1/2}$, which was twice that of PZT. Besides, the current FOM of the composites increased with increasing PZT content. Both the measured responsivities and detectivities of the pyroelectric sensors decreased with increasing irradiation frequency and became stable at above 100 Hz.

The electromechanical response of PU follows a simple quadratic relation with the applied electric field and the electrostriction coefficient is about 1.7×10^{-17} m^2/V^2. The electromechanical response of pure PZT forms a conventional hysteresis loop in butterfly shape and it is closely related to the *D-E* loop. Switching in the electrostrictive strain of the PZT/PU composites is observed. The critical field decreases with PZT volume fraction. For composites with high PZT volume fraction, the electromechanical responses are similar to the PZT except that the polarization switching fields are higher. A "hum" at the switching field in current-electric filed loop indicates the switching in the strain is due to dipole flipping in PZT. A mixture of carbon black and silicone as compliant electrode material manifests less clamping effect than the metallic electrodes. More than three times increment in the electrostriction coefficient of PU was found with the compliant electrodes.

Bending of a PU single film under an applied electric field is observed and its magnitude is found proportional to the square of the applied field. The bending effect is likely caused by the asymmetrical electrostriction on both side of the film. It may be attributed to the inhomogenous distribution due to injected charge which produces an asymmetrical electric field along the thickness direction. The film does not exhibit observable bending without the application of electric field even when a charge gradient exists in the film. The bending magnitude depends on the history of field application. In addition, the film will initially bend in the previous direction when the field polarity is reversed, but as the charge redistribute to form a new gradient, the film will bend to the opposite direction again. On the other hand, the bending response of bimorphs follows a hysteresis loop of butterfly shape. This can be explained by the electrostriction of the PZT/PU composite in the thickness direction. By using this special bending response, a symmetric, bi-directional bending actuator may be realized.

8.2 Suggestions for Future Work

One of the models in this thesis shows that the pyroelectric coefficient of 0-3 composites is strongly affected by the electrical conductivities of the matrix material. The higher conductivity of the matrix will give a larger pyroelectric coefficient. A more detailed investigation may lead to a new sensor material that has both higher pyroelectric coefficient and FOM. In addition, it has been demonstrated that the electrical conductivity of the PZT/PU composite affects its electromechanical performance as well. A further investigation into the effect of conductivity is worthwhile.

A new type of compliant electrode made by a mixture of carbon black and silicone has been demonstrated. It can provide less constraint in the electrostriction of flexible materials. This compliant electrode material can also be applied to the bending actuators to provide larger bending displacement.

References

Chan, H.L.W., Chen, Y. and Choy, C.L., "A Poling Study of PZT/P(VDF-TrFE) Copolymer 0-3 Composites", *Integrated Ferroelectrics*, Vol. 9(1-3), pp.207-214 (1995).

Chen, F.C., Poon, Y.M. and Choy, C.L., "Thermal Diffusivity of Polymers by the Flash Method", *Polymer*, Vol. 18, pp. 129-136 (1977).

Choy, C.L., Luk, W.H. and Chen, F.C., "Thermal Conductivity of Highly Oriented Polyethylene" *Polymer*, Vol. 19, pp. 155-162 (1978).

Choy, C.L., Leung, W.P. and Ng, Y.K., "Thermal Diffusivity of Polymer Films by the Flash Radiometry Method", *Journal of Polymer Science: Part B*, Vol. 25, pp.1779-1799 (1987).

Clegg, W.W., Jenkins, D.F.L. and Cunningham, M.J., "The Preparation of Piezoceramic-Polymer Thick Films and their Application as Micromechanical Actuators", *Sensors and Actuators A*, Vol. 58(3), pp.173-177 (1997).

Damjanovic, D., "Ferroelectric Dielectric and Piezoelectric Properties of Ferroelectric Thin Films and Ceramics", *Reports on Progress in Physics*, Vol. 61, pp. 1267-1324 (1998).

Das-Gupta, D.K., "Pyroelectricity in Polymers", *Ferroelectrics*, Vol. 118, pp. 165-189 (1991).

Dereniak, E.L. and Boreman, G.D., *Infrared Detectors and Systems*, A Wiley-Interscience Publication, New York, (1996).

Dias, C.J. and Das-Gupta, D.K., "Inorganic Ceramic/Polymer Ferroelectric Composite Electrets", *IEEE Transactions on Dielectrics and Electrical Insulation*, Vol. 3(5), pp.706-734 (1996).

Donaldson, A.B., "Radial Conduction Effects in the Pulse Method of Measuring Thermal Diffusivity", *Journal of Applied Physics*, Vol. 43, pp. 4226-4228 (1972).

Furukawa, T., Fujino, K. and Fukada, E., "Electromechanical Properties in the Composites of Epoxy Resin and PZT Ceramics", *Journal of Applied Physics*, Vol. 15, pp. 2119-2129 (1976).

Furukawa, T., Suzuki, K. and Date, M., "Switching Process in Composite Systems of PZT Ceramics and Polymers", *Ferroelectrics*, Vol. 68, pp. 33-44 (1986).

Furukawa, T. and Seo, N., "Electrostriction as the Origin of Piezoelectricity in Ferroelectric Polymers", *Japanese Journal of Applied Physics*, Vol. 29, pp.675-680, 1990.

Garn, L.E. and Sharp, E.J. "Use of Low-Frequency Sinusoidal Temperature Waves to Separate Pyroelectric Current from Nonpyroelectric Currents. Part II: Experiment", *Journal of Applied Physics*, Vol. 53, pp.8980-8987 (1982).

Haertling, G.H. "Ferroelectric Ceramics: History and Technology", *Journal. of the American Ceramic Society*, Vol.82, pp.797-818 (1999).

IEEE Standard on Piezoelectricity, ANSI/IEEE Standard 176-1987, IEEE New York (1988).

Jaffe, B., Cook, W. R. and Jaffe, H., *Piezoelectric Ceramics*, Academic Press, London and New York (1971).

Johnson, B., "Thermal Agitation of Electricity in Conductors", Physical Review, Vol. 32, pp. 79-109 (1928).

Kanno, T., Saga, M., Matsumoto, S., Uchida, M., Tsukamoto, N., Tanaka, A., Itoh, S., Nakazato, A., Endoh, T., Tohyama, S., Yamamoto, Y., Murashima, S., Fujimoto, N. and Teramishi, N., "Uncooled Infrared Focal Plane Array having 128×128 Thermopile Detector Elements", *Proceedings of SPIE*, Vol. 2269, pp. 450-459 (1994).

Kholkin, A.L., Wutchrich, C.H., Taylor, D.V. and Setter, N., "Interferometric Measurements of Electric Field Induced Displacements in Piezoelectric Thin Film", *Review of Scientific Instruments*, Vol. 67, pp.1935-1941 (1996).

Kim, J.S., Kim, Y.H., Lee, N.H. and Lee, D.C., "Ceramic-Polymers Composite Materials for Underwater Distance Sensor", *Molecular Crystals and Liquid Crystals Science and Technology Section A*, Vol. 247, pp.341-350 (1994).

Kinase, W. and Takahashi, H., *Journal of the Physical Society of Japan*. Vol. 10, pp. 942 (1995).

Krakovský, I., Romijn, T. and De Boer, A.P., "A Few Remarks on the Electrostriction of Elastomers", *Journal of Applied Physics*, Vol. 85, pp.628-629 (1999).

Kruse, W., McGlauchlin, L.D. and McQuistan, R.B., *Elements of Infrared Technology*, Wiley, New York, (1962).

Kruse, P.W. and Slattrud, D.D., Semiconductors and Semimetals: Vol. 47, Academic Press, New York, (1997).

Kyokane, J., Ishimoto, H., Yugen, H., Hirai, T., Ueda, T. and Yoshino, K., "Electrostriction Effect of Polyurethane Elastomer (PUE) and its Application to Actuators", *Synthetic Metals*, Vol. 103, pp. 2366-2367 (1999).

Leung, W.P. and Tam, A.C., "Techniques of Flash Radiometry", *Journal of Applied Physics*, Vol. 56, pp.153-160 (1984).

Marsh, K.N., *Recommended Reference Materials for the Realization of Physicochemical Properties*, Blackwell Scientific Publications, Oxford, (1987).

Mason W.P., *Physical Acoustics: Principles and Methods*, Academic Press, New York, (1964).

Morgan, S. H., Silberman, E. and Springer,J. M., "Laboratory Experiment on the Measurement of Pyroelectric Coefficients", *American Journal of Physics,* Vol. 52, Iss. 6, pp. 542-545 (1984).

Nigar, M., Blackwell, J., Chvalun, S.N., Seneker, S.D. and Schmelzer, H.G. "The Structure of the Domains in Trans, trans-HMDI-Base Polyurethane Elastomers" *Acta Polymeric*, Vol. 47, pp.48-54 (1996).

Noshay, A. and McGrath, J.E., *Block copolymers. Academic Press*, New York, pp. 516, (1977).

Nye, J.F., *Physical Properties of Crystals*, Clarendon Press, Oxford (1987).

Newnham, R.E., Skinner, D.P., Klicker, K.A., Bhalla, A.S., Hardiman, B. and Gururaja, T.R., "Ferroelectric Ceramic-Plastic Composites for Piezoelectric and Pyroelectric Applications", *Ferroelectrics*, Vol. 27 (1-4), pp.49-55 (1980).

Parker, W.J., Jenkins, R.J., Butler, C.P. and Abbott, G.L., "Flash Method of Determining Thermal Diffusivity, Heat Capacity and Thermal Conductivity", *Journal of Applied Physics*, Vol. 32, pp.1679-1684 (1961).

Pelrine, R.E., Kornbluh, R.D. and Joseph, J.P., "Electrostriction of Polymer Dielectrics with Compliant Electrodes as a Means of Actuation", *Sensors and Actuators A*, Vol. 64, pp. 77-85 (1998).

Riseic, L., *Sensor Technology and Devices*, Artech House, Boston, (1994).

Rogalski, A., *Infrared Detectors*, Gordon and Breach Science Publishers, Netherlands, pp. 124-147 (2000).

Sakamoto, W.K., Kagsawa, S. and Kanda, D.H., "Electric Properties of a Composite of Polyurethane and Ferroelectric Ceramics", *Journal of Materials Science*, Vol.33,

pp.3325-3329 (1998).

Sakamoto, W.K., Shibatta-Kagesawa, S., Kanda, D.H.F., Fernandes, S.H., Longo, E. and Chierice, G.O., "Piezoelectric Effect in Composite Polyurethane - Ferroelectric Ceramics", *Physical Status Solid A*, Vol. 172 (1), pp. 265-271 (1999 a).

Sakamoto, W.K., Shibatta-Kagesawa, S.T. and Melo, W.L.B., "Voltage Responsivity of Pyroelectric Sensor", *Sensor and Actuators A*, Vol. 77, pp.28-33 (1999 b).

Sakamoto, W.K. and Das-Gupta, D.K., "Electromechanical Properties of 0-3 Vegetable Based Polyurethane and Lead Zirconate Titanate Composite", *Dielectric Materials, Measurements and Applications Conference Publication*, No. 437, (2000).

Sakamoto, W.K., Darcy, H.F. and Das-Gupta, D.K., "Dielectric and Pyroelectric Properties of a Composite of Ferroelectric Ceramic and Polyurethane", *Materials Research Innovation*, Vol. 5, pp. 257-260 (2002).

Shaulov, A., Rosenthal, A. and Simhony, M., "Pyroelectric Voltage Response to Rectangular Infrared Signals in Triglycine Sulfate and Strontium-Barium Niobate." *Journal of Applied Physics*, Vol. 43, pp. 1440 (1972).

Shkel, Y.M. and Klingenberg, D.J., "Electrostriction of Polarizable Materials: Comparison of Models with Experimental Data "*Journal of Applied Physics*, Vol. 83, pp. 415-424 (1998).

Simhony, M. and Shaulov, A. "Pyroelectric Voltage Response to Step Signals of Infrared Radiation in Triglycine Sulfate and Strontium-Barium Niobate," *Journal of Applied Physics*, Vol. 42, pp. 3741 (1971).

Skinner, D.P., Newnham, R.E. and Cross, L.E., "Flexible Composite Transducers", *Materials Research Bulletin*, Vol. 13 (6), pp.599-607 (1978).

Steel, W.H., *Interferometry*, Cambridge University Press, New York, (1983).

Su, J. and Zhang, Q.M., "Space-Charge-Enhanced Electromechanical Response in Thin-Film Polyurethane Elastomers", *Applied Physics Letters*, Vol. 71(3), pp. 396-388 (1997 a).

Su J, Zhang Q.M., Kim C.H. Ting R.Y. and Capps R., "Effects of Transitional Phenomena on the Electric Field Induced Strain-Electrostrictive Response of a Segmented Polyurethane Elastomer", *Journal of Applied Polymer Science*, Vol. 65, pp.1363-1370 (1997 b).

Su, J., Zhang, Q.M., Wang, P.C., MacDiarmid, A.G. and Wynne, K.J., "Preparation and

Characterization of Electrostrictive Polyurethane Films with Conductive Polymer Electrodes", *Polymers for Advanced Technologies*, Vol. 9, pp.317-321 (1998).

Turnhout, J.V., *Thermally Stimulated Discharge of Polymer Electrets*, Elsevier Science, Amsterdam, (1975).

Ueda, T, Kasazaki, T., Kunitake, N., Hirai, T., Kyokane, J. and Yashino, K., "Polyurethane Elastomer Actuator", *Synthetic Metals*, Vol. 85, pp. 1415-1416 (1997).

Wada, Y. and Hayakawa, R., "A Model Theory of Piezo- and Pyroelectricity of Poly(Vinylidene Fluoride) Electret", *Ferroelectrics*, Vol. 32, pp. 115-118 (1981).

Wang, H., Zhang, Q.M. and Cross, L.E. "Clamping Effect on the Piezoelectric Properties of Poly(Vinylidene Fluoride-Trifluoroethylene) Copolymer", *Ferroelectrics*, Vol. 150, pp. 255-266 (1993).

Watanabe, M., Yokoyama, M., Ueda, T., Kasazaki, T., Hirai, M. and Hirai, T., "Bending Deformation of Monolayer Polyurethane Film Induced by an Electric Field, *Chemistry Letters*, Vol. 8, pp. 773-774 (1997).

Watanabe, M., Hirai, T., Ueda, T., Suzuki, M. and Amaike, Y., "Polyurethane Actuators Using Bending Piezoelectricity and Bending Electrostriction, *Journal of Intelligent Material Systems and Structures*, Vol. 10, pp.100-104 (1999 a).

Watanabe, M., Hirai, T., Suzuki, M. and Amaike, Y., "Electric Conduction in Bending Electrostriction of Polyurethane", *Applied Physics Letters*, Vol. 74 (18), pp. 2717-2719 (1999 b).

Watanabe, M., Kato, T., Suzuki, M., Amaike, Y. and Hirai, T., "Bending Electrostriction in Polyurethanes Containing Ions as Contaminants or Additives, *Japanese Journal of Applied physics*: Part 2, Vol. 38(8A), pp. L872-L874 (1999 c).

Watanabe, M., Shirai, H., Hirai, T., Suzuki, M. and Hirako, Y., "Bending Electrostriction in Polyurethane Using In-Situ Ultraviolet and Visible Spectroscopies, *Journal of Applied Physics*, Vol. 88(9), pp.5328-5333 (2000).

Watanabe, M., Suzuki, M., Hirako, Y., Shirai, H. and Hirai, T., "Hysteresis in Bending Electrostriction of Polyurethane Films", *Journal of Applied Polymer Science*, Vol. 79, pp. 1121-1126 (2001 a).

Watanabe, M., Kato T., Suzuki, M., Hirako, Y., Shirai, H. and Hirai, T., "Control of Bending Electrostriction in Polyurethane Films by Doping with Salt", *Journal of Polymer Science*: Part B: Polymer Physics, Vol. 39, pp. 1061-1069 (2001 b).

Watanabe, M., Shirai, H. and Hirai, T., "Ionic Polarization in Bending Electrostrictive

Response of Polyurethane Films", *Journal of Applied Physics*, Vol. 90(12), pp. 6316-6320 (2001 c).

Watanabe, M., Shirai, H. and Hirai, T., "Wrikled Polypyrrole Electrode for Electroactive Polymer Actuators", *Journal of Applied Physics*, Vol. 92(8), pp. 4631-467 (2002).

Whatmore, W., "Pyroelectric Ceramics and Devices for Thermal Infra-Red Detection and Imaging", *Ferroelectrics*, Vol. 118, pp. 241-259 (1991).

Willardson R. K. and Beer A. C., *Semiconductors and Semimetals: Vol. 5*, Academic Press, New York, (1970).

Wong, Y.W., Liu C.X., Tai, L.S. and Shin, F.G., "Electrostriction of Composite of Polyurethane (PU) with Ferroelectric Lead Zirconate Titanate (PZT) Ceramic Particles", *Proceedings of SPIE*, Vol. 4329, pp. 516-521 (2001 a).

Wong, Y.W., Tai, L.S., Liu, C.X. and Shin, F.G., "An Investigation of the Electrostrictive Property of PZT/Polyurethane Particulate Composites, *Ferroelectrics*, Vol. 264 (1-4), pp. 1715-1720 (2001 b).

Wong, C.K., Poon, Y.M. and Shin, F.G., "Explicit Formulas for Effective Piezoelectric Coefficients of Ferroelectric 0-3 Composites", *Journal of Applied Physics*, Vol.90, pp. 4690-4700 (2001 c).

Wong, C.K., Wong, Y.W. and Shin, F.G., "Effect of Interfacial Charge on Polarization Switching of Lead Zirconate Titanate Particles in Lead Zirconate Titanate/Polyurethane Composites", *Journal of Applied Physics*, Vol. 92, pp.3974-3978 (2002).

Xu, Y., *Ferroelectric Materials and Their Applications*, Elsevier Science, North-Holland (1991).

Yamada, T., Ueda, T. and Kitayama, T., "Piezoelectricity of High-Content Lead Zirconate Titanate/Polymer Composite", *Journal of Applied Physics*, Vol. 53(6), pp.4328-4332 (1982).

Yamazaki, H. and Kitayama, T., "Pyroelectric Properties of Polymer-Ferroelectric Composites", *Ferroelectrics*, Vol. 33(1-4), pp. 147-153 (1981).

Yoseph, B.C., *Electroactive Polymer (EAP) Actuators as Artificial Muscles: Reality, Potential, and Challenges*, SPIE, USA (2001).

Zhang, Q.M., Pan, Y.W. and Cross, L.E., "Laser Interferometer for the Study of Piezoelectric and Electrostrictive Strains", *Journal of Applied Physics*, Vol. 63, pp.2492-2496 (1988)

Zhang, Q.M., Jang, S.J. and Cross, L.E., "High-Frequency Strain Response in Ferroelectrics and Its Measurement Using a Modified Mach-Zehnder Interferometer", *Journal of Applied Physics*, Vol. 65, pp.2807-2813 (1989).

Zhang, Q.M., Su, J., Kim, C.H., Tinf, R. and Capps, R., "An Experimental Investigation of Electromechanical Response in a Polyurethane Elastomer", *Journal of Applied Physics*, Vol. 81, pp.2770-2776 (1997)

Zhenyi, M., Scheinbeim, J.I., Lee, J.E. and Newman, B.A., "High Field Electrostrictive Response of Polymers", *Journal of Polymer Science Part B: Polymer Physics*, Vol. 32, pp.2721-2731 (1994).

Zimmerman, R. L., Suchicital, C. and Fukada, E., "Electric Field Induced Piezoelectricity in Polymer Film", *Journal of Applied Polymer Science*, Vol. 19, Iss. 5, pp. 1373-1379 (1975).

List of Publication

Conference Paper

Lam, K.S., Wong, Y.W., Tai, L.S., Poon, Y.M. and SHIN, F.G., "The Bending Mechanism of Thermoplastic Polyurethane under an Applied Electric Field", *Proceedings of SPIE*, Vol. 5051, pp. 526-533 (2002).